Master's thesis

NTNU
Norwegian University of Science and Technology
Faculty of Natural Sciences
Department of Physics

Jacob Wilder Ng

Glow Discharge Optical Emission Spectroscopy for Elemental Characterization of Doped TiO_2 Thin Films made by Pulsed Laser Deposition

Master's thesis in Innovative Sustainable Energy Engineering
Supervisor: Turid Reenaas
Co-supervisor: Marisa Di Sabatino and Stela Canulescu
June 2023

NTNU
Norwegian University of
Science and Technology

DTU
Technical University
of Denmark

Jacob Wilder Ng

Glow Discharge Optical Emission Spectroscopy for Elemental Characterization of Doped TiO_2 Thin Films made by Pulsed Laser Deposition

Master's thesis in Innovative Sustainable Energy Engineering
Supervisor: Turid Reenaas
Co-supervisor: Marisa Di Sabatino and Stela Canulescu
June 2023

Norwegian University of Science and Technology
Faculty of Natural Sciences
Department of Physics

Abstract

Glow discharge optical emission spectroscopy has been used to characterize thin film samples fabricated by pulsed laser deposition. The principal samples are (Cr+N) co-doped TiO_2 films deposited by natural spread combinatorial PLD. (Cr+N) co-doped TiO_2 is relevant as a possible intermediate band material which could be used to create more efficient photovoltaic cells. The light absorption properties of the material depend on the doping concentrations of Cr and N, and GDOES is one available technique to analyze these concentrations.

Numerous preliminary PLD films (based on either TiO_2 or CrN) were first examined qualitatively to become familiar with GDOES and its application to this family of samples. Comparison between samples deposited under different PLD conditions confirms previous findings that a low substrate temperature and deposition in N_2 background are keys to adequately incorporating N into the final film, during both CrN and TiO_2 depositions. Issues stemming from atmospheric contamination during GDOES measurement were mitigated by employing a low-power measurement method to assess vacuum conditions before proceeding to a normal measurement.

A variety of samples of known composition (containing Ti, O, Cr, N, and/or Si) were used to developed GDOES calibration curves for these elements. The curves are formed by a relation between known elemental concentrations, sputtering rates determined by crater depth measurement, and measured elemental emission signal intensities. An attempt to artificially reduce sputtering rates for additional data points was inconclusive. For each element, the data points were fit with a regression line, optionally including some correction factors.

The combinatorial PLD samples were measured with GDOES at four positions, following the direction of increasing doping concentration. The qualitative results are consistent with the trends observed in the preliminary PLD films and display the efficacy of a N_2-O_2 gas cycling routine and a TiO_xN_y capping scheme adopted in the PLD method. After applying the calibration curves for quantitative results, the Cr concentration is found to range from 5.9 - 17.3 at%, surpassing the values expected according to a PLD simulation. The N concentration is strongly dependent on the decision to apply a correction factor for possible Cr interference. The concentration range is 1.6 - 8.8 at% (without correction factor) or 7.0 - 19.0 at% (with correction factor). Work is needed to improve the calibration curves for more reliable quantification.

Sammendrag

Glimutladnings optisk emisjonsspektroskopi (GD-OES) har blitt brukt for å karakterisere tynnfilmprøver fremstilt ved hjelp av pulset laser deponering (PLD). De viktigste prøvene som er analysert er (Cr+N) ko-dopet TiO_2-filmer deponert ved hjelp av kombinatorisk PLD. (Cr+N) ko-dopet TiO_2 er et mulig mellombåndsmateriale som kan brukes til å lage mer effektive solceller. Materialets lysabsorpsjonsegenskaper avhenger av dopekonsentrasjonene av Cr og N, og GDOES er en mulig teknikk for å analysere disse konsentrasjonene.

Flere PLD-filmer (basert på enten TiO_2 eller CrN) ble først undersøkt kvalitativt for å bli kjent med GDOES-teknikken og dens anvendelse på denne typen prøver. Ved å sammenlige prøver deponert under ulike PLD-forhold ble tidligere funn bekreftet: en lav substrattemperatur og deponering i N_2-bakgrunnsgass er nøkkelen til tilstrekkelig inkorporering av N i den endelige filmen, under både CrN- og TiO_2-deponering. Problemer som stammet fra atmosfærisk forurensning under GDOES-målingene ble dempet ved å bruke en laveffekt-målemetode for å evaluere vakuumkvaliteten før man gikk videre med en normal måling.

En rekke prøver med kjent sammensetning (inneholdende Ti, O, Cr, N og/eller Si) ble brukt til å lage GDOES-kalibreringskurver for disse grunnstoffene. Kurvene ble laget på bakgrunn av relasjonen mellom kjente konsentrasjoner av ulike grunnstoff, sputterhastigheter bestemt ved kraterdybdemåling og målte emisjonssignalintensiteter for ulike grunnstoff. Et forsøk på kunstig reduksjon av sputtringshastighet for å få ytterligere datapunkter gav ikke entydige resultater. For hvert grunnstoff ble datapunktene tilpasset med en regresjonslinje, eventuelt inkludert noen korreksjonsfaktorer.

De kombinatoriske PLD-prøvene ble målt med GDOES for 4 ulike punkter på prøven, langs en akse med økende dopingkonsentrasjon. De kvalitative resultatene stemmer overens med trendene som er observert i de foreløpige PLD-filmene og viser at en N_2-O_2-gasssyklusrutine og et TiO_xN_y-beskyttelseslag tatt i bruk i PLD-metoden, fungerer. Etter å ha brukt kalibreringskurvene for å få kvantitative resultater, er Cr-konsentrasjonen funnet å variere fra 5,9 - 17,3 at%, og dette overgår verdiene sammenlignet med en simulering av forventet mengde doping. N-konsentrasjonen er sterkt avhengig av et valg om å bruke en korreksjonsfaktor for en mulig Cr-interferens. Målt mengde N er 1,6 - 8,8 at% (uten korreksjonsfaktor) eller 7,0 - 19,0 at% (med korreksjonsfaktor). Mer arbeid er nødvendig for å forbedre kalibreringskurvene for å få en mer pålitelig kvantifisering av sammensetning av prøvene.

Preface

I would like to thank a number of individuals for their support throughout this project:

First is my supervisor Professor Turid Reenaas, for welcoming me into her group, for her patience in training and explaining previous work, and for continuous feedback on research, analysis and documentation.

Marisa Di Sabatino for additional supervision, GDOES advice and administering the N5T study program in Innovative Sustainable Energy Engineering.

Stela Canulescu for additional supervision. Thank you also to all my professors at DTU, where I completed the first year of my Master degree program.

Thomas Brakstad, a PhD student in the group, was involved in depositing the samples studied here. Data from his prior ellipsometry measurements were extremely valuable.

Patrick Chapon, a GDOES researcher with HORIBA, offered many suggestions regarding the process and results in this project, shared additional training resources, and provided additional reference samples for calibration.

Sergey Khromov provided training for the GDOES instrument and stylus profilometer used in this work and was very responsive to questions about the interpretation of results.

Jakob Vinje (and the NTNU NanoLab) provided training for the 3D optical profiler used in this work. Øystein Gjervan Hagemo and the NTNU Finmekanisk verksted provided a titanium sample for calibration. Astrid Salvesen and the NTNU Glassblåserverksted provided a quartz sample for calibration. Hogne Lysne was also involved in the fabrication and prior analysis of the PLD samples.

And thank you to my fellow students Joseba Ormaetxea Orobengoa, Sarah Nyeki, Vilma Kristiansson, Harry Malhi, Andrés Greciano, and Ahmad Chehaimi for cinnamon rolls and cabin trips.

Jacob Ng
NTNU Trondheim
June 2023

Contents

Abstract **i**

Preface **v**

Contents **vii**

1 Introduction **1**

2 Theory **5**

2.1 Intermediate band solar cells 5
2.2 Glow discharge optical emission spectroscopy 9
2.2.1 Sputtering 10
2.2.2 Optical emission 12
2.2.3 Spectroscopy 14
2.2.4 Further considerations 15
2.3 Calibration for quantitative GDOES 19
2.3.1 Calibration curves 20
2.3.2 Emission yield 22
2.3.3 Sputtering rate 22
2.3.4 Errors and uncertainty 23
2.3.5 Curve fitting and application 24
2.4 Pulsed laser deposition 26

3 Methods and Experimental Details **29**

3.1 Samples 29
3.1.1 Fabricated samples 29
3.1.2 Reference samples for calibration 37
3.2 GDOES measurements 41
3.2.1 Equipment 41
3.2.2 Measurement procedure 43
3.2.3 Low-power plasma surface cleaning 45
3.2.4 Calibration curve formation 46
3.3 Stylus profilometer measurements 47
3.4 Optical profiler measurements 48

4 Results and Discussion **51**
4.1 Nitrogen signal consistency 51
4.2 Calibration measurements 56
4.2.1 GDOES profiles and craters 57
4.2.2 Calibration measurement summary tables 74
4.2.3 Reduced sputtering measurements 76
4.3 Calibration curves 80
4.4 PLD plume films - qualitative 91
4.5 PLD CCS films - qualitative 99
4.6 PLD CCS films - quantitative 106
4.7 Future work 114

5 Conclusions **117**

References **119**

Appendix A - Spectrometer detection wavelengths **125**

Chapter 1

Introduction

The following chapter is adapted from the author's previous specialization project [1]

The alarming impacts of climate change are increasingly apparent just from a scan of global headlines from year to year. Threatening forecasts of sea level rise, displaced populations, failing crops, and jeopardized health are shifting from dystopian science fiction to an uncomfortable reality [2]. Nations of the world have every reason to act, not only to avoid the impending harms, but also because a green transition promises new jobs, wealth creation, and sustainable development around the globe [3]. The burning of fossil fuels in the energy sector contributes to 60% of total greenhouse gas emissions, marking this as a crucial opportunity for transformation [4]. Thankfully, decarbonization of the energy sector is relatively straightforward, due to the abundance of alternative sources and ever-improving technologies to harness them.

The theoretical potential of renewable energy sources is undeniably staggering, with solar power alone easily capable of meeting the energy needs for all human civilization, as illustrated in Figure 1.1 [5, 6]. Efforts now focus on transitioning the power sector to renewable sources in a feasible manner. An upward trend in electrification will only enhance the relevance of this endeavour and further highlight challenges [8]. Technology for generating electricity from renewable sources has reached a cost parity with fossil fuels, but limitations remain when targeting sustainable terawatt-scale deployment [9]. These considerations include materials and production, capital costs, temporal and geographic variability, competing uses, and end-of-life treatment.

Solar photovoltaics (PV) are a clean energy technology whose installed capacity has exploded within the past decade, with a 2021 cumulative capacity of 940 GW [10]. The foundation of this technology is silicon, a semiconductor element which is able to convert incident light into electrical power. Silicon has enjoyed an extensive

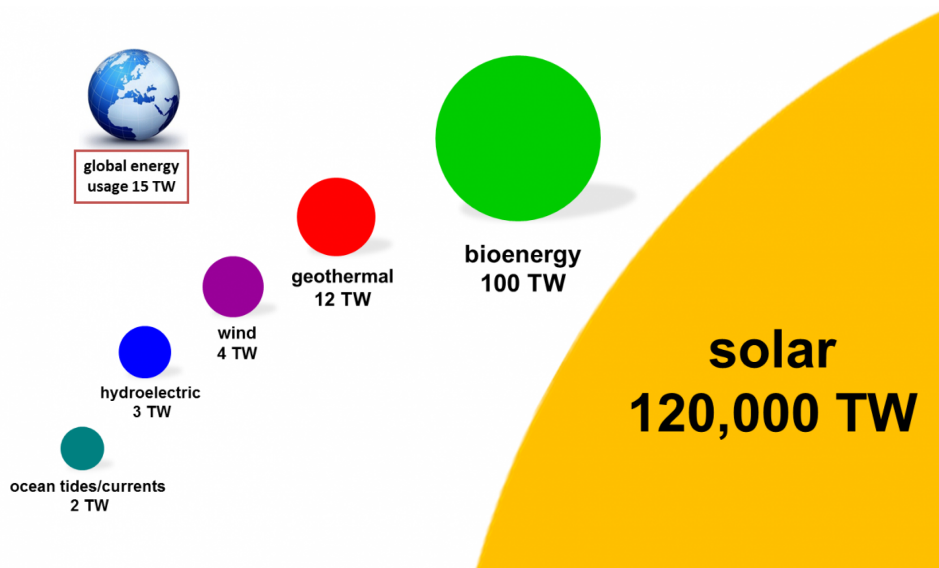

Figure 1.1: A visual comparison of global power demand with the absolute maximum production available from various renewable sources [7].

record of development, thanks in part to its ubiquity in the transistors which enable the modern age of digital computing. Silicon-based solar cells are driving the current wave of installations, as manufacturing expertise and economies of scale have steadily reduced costs, and the power conversion efficiency (PCE) has gradually inched higher.

After decades of research, however, the performance of silicon solar cells may be reaching a plateau. Production costs have dropped to $0.25/W [11] and the record PCE is around 27% [12] (although commercially available modules rarely exceed 23%). These metrics are admirable, but may be insufficient when contemplating a society predominantly powered by renewable energy. It is worth considering alternative materials and technologies to harness energy from sunlight. Silicon solar cells fall into a class termed "first-generation PV", because they first demonstrated the potential of photovoltaics to contribute meaning-fully in the power sector and other applications [13]. One of the limitations of silicon is its requirement for extreme purity. demanding energy-intensive processing steps. It is also a relatively poor absorber of light, so thicker layers of material are necessary, with associated costs [14].

"Second-generation PV" arose with the aim of developing materials to overcome these shortcomings of silicon. Examples include CdTe, CIGS, and amorphous-Si. These materials are superior light absorbers, with a "thin-film" being sufficient for a PV device. Here, "thin" means a few microns, compared to the hundreds of microns for a typical silicon cell. These thin-film PV technologies have the potential for high-throughput production methods with cheap costs [13]. Nevertheless, they are not without their own challenges. For the most part, they have not quite reached a stage of commercialization. Some rely on scarce or toxic elements, such as cad-

mium or indium. Their PCEs also remain lower than silicon, with records around 23%. Relatively young compared to silicon, these second-generation materials clearly have room to develop, and the "low-cost and low-efficiency" option will certainly be appropriate for some applications.

Finally, the more recent "third-generation PV" attempts to tackle the aforementioned issues by focusing on improving efficiency. The "Shockley–Queisser" limit is commonly-cited detailed balance model which calculates a maximum PV efficiency around 33% for un-concentrated sunlight on Earth. [15]. The most advanced silicon cells are already approaching this ceiling [5]. The Shockley–Queisser limit, however, is dependent on a several of physical and device assumptions. For example, a valid assumption for 1st- and 2nd-generation PV devices is that the semiconductor's single badgap doesn't allow light to be captured with full efficiency over the entire solar spectrum. A device with multiple bandgaps, however, could absorb light more efficiently and surpass the Shockley–Queisser limit. In one approach, multi-junction solar cells stack different semiconductors optimized to capture different regions of the solar spectrum. Alternatively, a semiconductor could be modified to have split the bandgap into multiple steps within a single material. Such a device is termed an intermediate band solar cell (IBSC) [13]. Though still in its infancy, the IBSC concept is worth exploring, as the introduction of just a single intermediate band could raise the theoretical efficiency to nearly 50%.

Such intermediate band materials have been the subject of research within Professor Reenaas' solar cell group at the NTNU Department of Physics. Current efforts are focused on titanium dioxide (TiO_2) as the semiconductor material, with the intermediate band formed by doping with chromium and nitrogen. Samples are fabricated by pulsed laser deposition (PLD) and feature a continuous compositional spread (CCS) of dopant concentrations. The optimal concentration of chromium and nitrogen are not yet known, so this approach is an efficient way to investigate the relation between various material properties and the doping level. An essential aspect of this characterization, therefore, is determining the concentration of chromium and nitrogen at various points along the sample. Various tools are available for this sort of elemental quantification, but not all are well-suited for these particular samples. For instance, secondary ion mass spectroscopy (SIMS) can be used to characterize ppm level concentrations of trace elements. But the chromium and nitrogen levels expected in these films is in the range 1-10 at%. Spectroscopic techniques based on electrons, such as energy dispersive x-ray spectroscopy (EDX), have limited detection capabilities for light elements such as nitrogen.

Glow discharge optical emission spectroscopy (GDOES) is a tool readily-available at NTNU which boasts high sensitivity for all elements, detection levels ranging from trace to major, fast measurements, and simple operation [16].

The thesis work this semester builds on previous specialization project work [1]. The aim is to perform quantitative analysis of PLD (Cr+N) co-doped TiO_2 films. The report first summarizes the working principle of intermediate band solar cells, including the specific material combination pursued in this group. The rest of the chapter is devoted to the basic theory of glow discharge optical emission spectroscopy, followed by an assortment of additional details regarding the technique, and an overview of the equations and calibration process required for quantitative compositional analysis. A introduction to pulsed laser deposition is provided, relevant to the fabricated samples investigated.

Next, a synopsis of the all the PLD and calibration samples is given. The specific instrumental setup is described, along with the basics of operation. Sample mounting, polychromator calibration, and acquisition settings are mentioned. The specifics of calibration curve formation in software are mentioned. Sections follow concerning stylus profilometery and 3D optical profilometry, two complementary technique which can be used to inform the GDOES parameters.

The results chapter first presents a method to predict and avoid atmospheric nitrogen contamination in GDOES measurements. All calibration measurements are presented (both GDOES profiles and crater profiles). An idea related to reducing sputtering rates in calibration samples is considered. The calibration measurements are used to develop calibration curves, with corrections applied to some.

Quantitative results are presented for some preliminary PLD films and then for the PLD CCS films. Finally, the calibration curves are applied to the PLD CCS films for quantitative analysis. The chapter finishes with various recommendations for future work.

A conclusion reiterates the work and findings, and numerous suggestions for further work are suggested.

Chapter 2

Theory

The following chapter includes sections adapted from the author's previous specialization project [1]

This Theory chapter begins with a description of the intermediate band concept for solar cells. This is included to provide context for the project work; the information is not directly required to understand the report.

Next, the glow discharge optical emission spectroscopy technique is explained. The basic theory is divided into three main stages: sputtering, optical emission, and spectroscopic detection. This foundation is followed by some details related to crater shape and its impact on depth resolution, as well as warnings about a number of interference effects important for interpreting the results.

The qualitative processes of GDOES are then developed into a quantitative method - composition depth profiling. The section covers considerations in the selection of calibration samples, conditions for valid calibration curves, required methods to determine sputtering rate, measurement uncertainty, and finally curve-fitting by regression.

The chapter concludes with an overview of pulsed laser deposition, including details relevant to the fabricated samples analyzed in this work.

2.1 Intermediate band solar cells

Solar cell materials are classified as semiconductors, which means that their electron energy band structure features a gap, below which the bands are filled with electrons and above which the bands are filled with holes (or absent of electrons). The size of this bandgap E_g determines the photon energy threshold required in order to excite an electron from the lower valence band (VB) to the upper conduction band (CB). A smaller bandgap (less than 1 eV, for example) allows the material to absorb lower energy light from the solar spectrum, such as infrared, in addition to visible and

ultraviolet. More photo-absorption equates to a larger photo-current. However, when power is extracted from the PV device, the voltage is determined by the potential difference between charges in the CB and VB, that is, the size of the bandgap. Clearly a trade-off exists between current and voltage, both of which depend on the bandgap, and the product of which determines the power output. The optimization calculation was first reported in 1961 by Shockley and Queisser, concluding that the maximum theoretical efficiency for a solar cell is around 30%, achieved at a bandgap of 1.1 eV, which conveniently matches silicon [15]. This precise value has since been updated (33.16% for $E_g = 1.34$ eV) [17], but the fact remains that the best-performing silicon cells are already approaching this limit, with a record power conversion efficiency (PCE) of 26.7% [12].

One of the assumptions inherent in the Shockley-Queisser limit is a single bandgap. Stacking multiple bandgaps could allow more efficient photo-absorption over the solar spectrum while maintaining a larger device voltage. This gives rise to the concepts of multi-junction solar cells and intermediate band solar cells (IBSCs). In the case of IBSCs, the most common arrangement seeks to produce an intermediate band (IB) within a large bandgap, effectively splitting the gap into two, and offering three pathways for the optical excitation of charges: from VB to IB, from IB to CB, and from VB to CB. These routes are illustrated in Figure 2.1, where transitions between band combinations can be either generation (G) or recombination (R). Such a material would be sandwiched between the n-type and p-type semiconductors which typically comprise a solar cell. In this configuration, the intermediate band material acts as a more efficient absorbing layer, and the n- and p-type layers allow excited charge carriers to be extracted for electrical power.

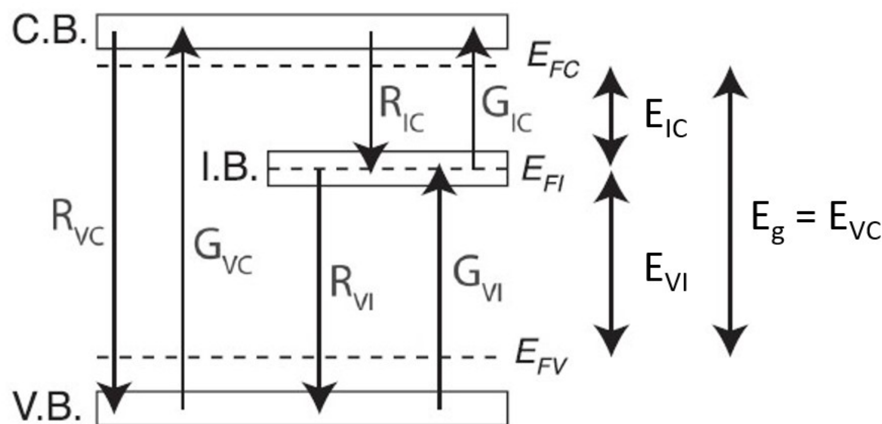

Figure 2.1: A band diagram schematic of a semiconductor with an intermediate band (IB) located within the bandgap. Various electronic transitions (generation (G), recombination (R)) are possible between the VB, IB, and CB. The IB splits the total E_g into two smaller gaps. Also shown are the quasi-Fermi energy levels for each band. Adapted from [18].

With the same Shockley-Queisser trade-offs in mind, the total bandgap E_g and the placement of the intermediate band are important for maximizing potential efficiency. A large E_g is suited to absorption of shorter wavelengths. The subgap sizes E_{VI} and E_{IC} should allow absorption of longer wavelength photons, but it is also important to match the current into and out of the IB, which depends on the solar spectrum (assuming AM1.5, for instance). One paper reports a theoretical max PCE of 46.8% for $E_g \approx 2.4$ eV and $E_{IC} \approx 0.9$ eV [18], approximately 1.5x larger than the Shockley-Queisser case for a single bandgap.

The IBSC concept clearly has advantages, but implementation still remains a challenge. In particular, finding appropriate materials and methods to form the IB remain a topic of investigation. Proposed approaches include using quantum dots and highly mismatched alloys [18, 19]. Another suggestion is uncompensated n-p co-doping of wide-bandgap oxide semiconductors. In this regard, titanium dioxide (TiO_2) is a possible choice of host material. TiO_2 is already an attractive material for photo-energy applications thanks to its low cost, chemically inertness, photo-stability, and good charge transport properties [20, 21]. However, its bandgap of >3 eV puts its absorption edge in the UV range, whereas the visible range would often be preferable.

Experiments and simulations have tested doping to decrease the bandgap, and n-p co-doping has emerged as a promising tactic, since it improves the solubility of dopants at substitutional sites. Further, non-compensated doping, where n-type and p-type dopant charges don't completely cancel each other, prompts the formation of an intermediate band, enabling absorption over a wider range of photon energies. DFT calculations, and subsequent experiments, have suggested chromium and nitrogen as a possible n-p co-dopant pair in anatase TiO_2 [20, 22]. Figure 2.2 presents DFT results of the density of states around the bandgap of TiO_2 when co-doped with Cr and N.

The dotted line marks the density of states for undoped TiO_2, where the VB maximum lies at 0 eV and states at the CB minimum don't appear until 3.2 eV. In the doped case, the VB maximum increases slightly, and, notably, some states are introduced within the bandgap.

Normally, when doping is discussed in the context of solar materials, it might be on the scale of parts-per-million (ppm), such as a concentration of 10^{18} cm^{-3} phosphorous atoms in the case of n-doped silicon (where the intrinsic density is around $5x10^{22}$ cm^{-3}). However, the doping levels proposed in (Cr+N) co-doping would be at the percentage level [22]. This shifts the detection regime required for quantification, motivating an investigation into the suitability of glow discharge optical emission spectroscopy for this task.

The (Cr+N) co-doped TiO_2 is the approach currently being explored by Professor Reenaas' group in the Physics department at NTNU, with thin film samples being

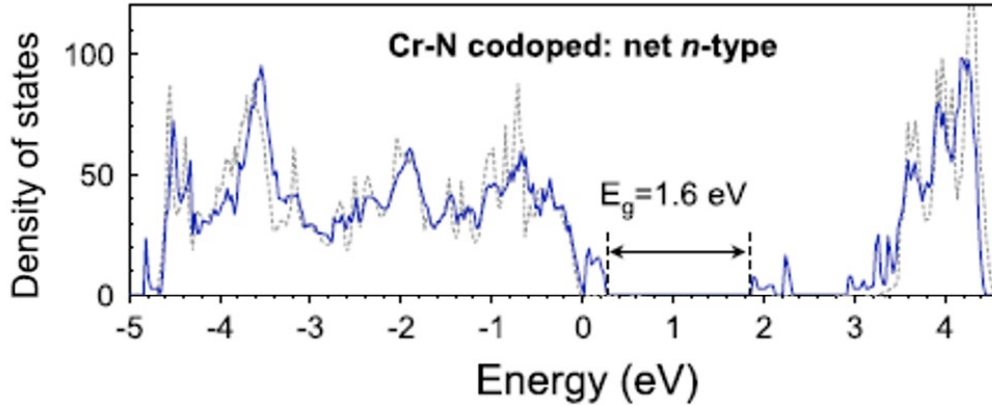

Figure 2.2: Density of states (DOS) for anatase TiO_2 co-doped with Cr and N (uncompensated such that net doping is n-type) according to DFT calculations. The dotted line shows the DOS for undoped TiO_2, where the VB maximum ends at 0 eV and the CB minimum doesn't appear until 3.2 eV. The solid line shows a decreased bandgap in the doped case. Adapted from [22].

fabricated by pulsed laser deposition (PLD). The optimal Cr and N doping concentration is not known, so combinatorial PLD is used to fabricate TiO_2-based films with a gradient in composition across a 2" silicon wafer substrate, allowing a comparative study of material properties at different doping levels. This PLD process will be elaborated in Section 2.4.

2.2 Glow discharge optical emission spectroscopy

One of the most fundamental properties to determine after deposition of a sample or discovery of a material is its elemental composition. This information might be somewhat known beforehand or may be completely unknown. The desired output could be a breakdown of bulk composition by atomic mass, or a spatial map of elemental distribution, or the concentration of some dopant or trace material. Some common tools for this purpose include energy-dispersive spectroscopy (EDS), X-ray photoelectron spectroscopy (XPS), or secondary-ion mass spectrometry (SIMS). Another, more recently developed, technique is called glow discharge optical emission spectroscopy (GDOES).

GDOES is a relatively quick method for elemental depth profiling of a sample; the technique is especially well-developed for the analysis of bulk metals, but is continually expanding to the application of diverse thin films as well. The instrument combines plasma sputtering with a spectrometer to identify elemental signals based on characteristic optical emissions from the sputtered sample atoms. The following overview of the technique is largely based on the practical textbook by Nelis and Payling [23] as well as the user manual for HORIBA's GD Profiler 2 [24]. The instrument is pictured in Figure 2.3.

Figure 2.3: A photograph of the GD Profiler 2 by HORIBA Scientific. It is an RF-GDOES instrument, shown here with the sample compartment cover open [24].

The diagram in Figure 2.4 sketches out the major components of the sample compartment and plasma system. The sample to be analyzed, which must have a solid, flat surface, is placed up against the chamber wall. A simple vacuum and O-ring seal the surface, and an electrode/cooling block is held in place against the backside of the sample. With the ambient atmosphere evacuated, the chamber is then filled with argon gas (typically to a pressure between 500-900 Pa). The glow discharge is formed by biasing the anode (a copper tube which extends nearly to

the sample surface) and the sample (which becomes the cathode via its contact with the rear electrode). The rear electrode block also contains a water cooling circuit to prevent the sample from heating too much during exposure to the plasma [25].

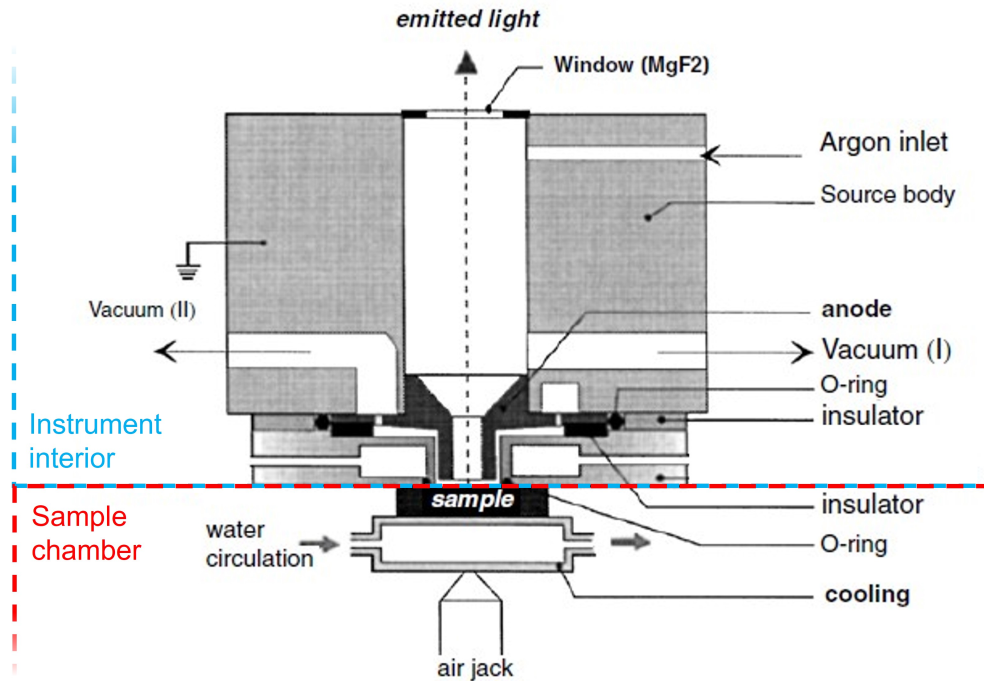

Figure 2.4: A schematic (top-down) view of the sample compartment and components of the plasma system (not typically accessible to the user). Adapted from [23].

2.2.1 Sputtering

The diameter of the anode determines the size of the area on the sample surface to be analyzed. 4 mm is common, so the technique is not well-suited for profiling precise points on the sample. Most instruments now employ radio frequency (RF) biasing (at 13.56 MHz), as this allows non-conductive samples to be analyzed while avoiding any issues of charge build-up. With a sufficient voltage (>150 V), the argon gas ionizes into Ar^+ and e^-, and these particles are alternately accelerated toward and away from the sample. In an effort to control experimental variables, the plasma is usually held at a constant pressure and supplied with a constant power ($P = IV$). In this mode, the product of voltage and current is fixed, but the ratio between them can change. This value (representing an impedance, $Z = \frac{V}{I}$) is automatically adjusted to facilitate impedance matching with the plasma, as this minimizes power reflected back to the source [24].

The argon ions bombard the sample surface with an energy of around 50 eV, sufficient to break chemical bonds at the surface and sputter off material [26]. The process is fast, with erosion rates up to 100 nm/s [25]. This makes GDOES attractive for thicker layers on the order of µm [27]. Ideally, the surface sputtering will be uniform across the area and erode a flat-bottomed crater with time (as illustrated

in Figure 2.5). The actual sputtering rate varies with the elemental composition (according to sputtering yield and preferential sputtering), crystallinity, and surface morphology like roughness [24].

Obviously, this is a destructive process, which limits some applications, or requires that this be the final stage in the case of multiple characterization methods.

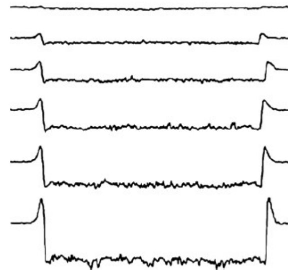

Figure 2.5: From top to bottom: Progressing stages of crater formation with longer sputtering times. Adapted from [23].

Compared to the density of argon atoms in the plasma, the sputtered atoms are very sparse, so it is mostly assumed that the plasma conditions are not significantly altered by the introduction of sputtered material. Further, the chamber experiences a constant combination of vacuum pumping and argon flow to maintain the set pressure. This continually flushes out sputtered material, minimizing potential residual signal from layers previously sputtered. With that said, however, some amount of sample material does re-deposit around the edge of the crater, and on the inner walls of the anode, as illustrated in Figure 2.6 [23]. This contamination can alter measurement of subsequent samples. Thus, a cleaning step is performed in between measurements, as will be described in the next chapter.

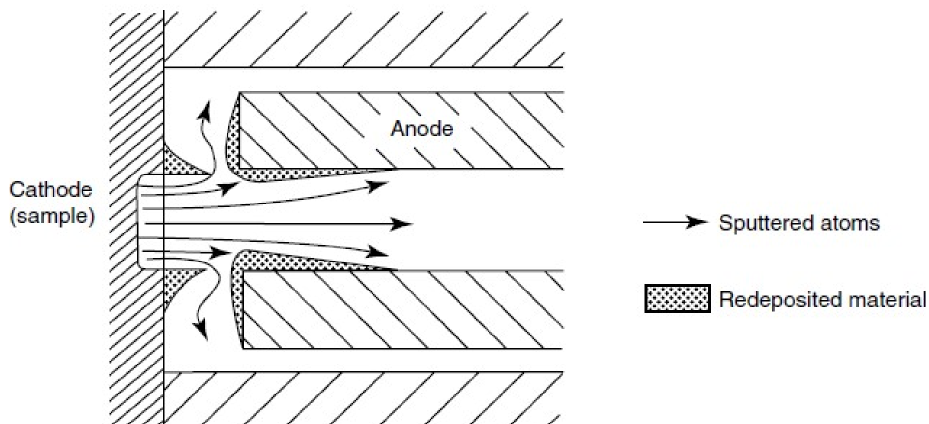

Figure 2.6: Various pathways of sputtered sample atoms during the sputtering process. Most exit into the argon plasma, where they contribute to the total optical signal. Some, however, re-deposit around the edge of the crater, at the sample-anode gap, or along the inner walls of the anode [23].

2.2.2 Optical emission

Once the sputtered sample atoms eject into the plasma, they are subject to energizing collisions with the free electrons and argon ions forming the plasma. These sample atoms' electrons are excited to available shells at a higher-energy. They then de-excite (electrons drop back down to fill the vacancy in the lower shell) by radiative emission [23]. Due to the the conservation of energy and the quantized nature of electronic energy levels, the photons produced are limited to a set of particular wavelengths according to the electronic transition which created them. This process is illustrated in Figure 2.7.

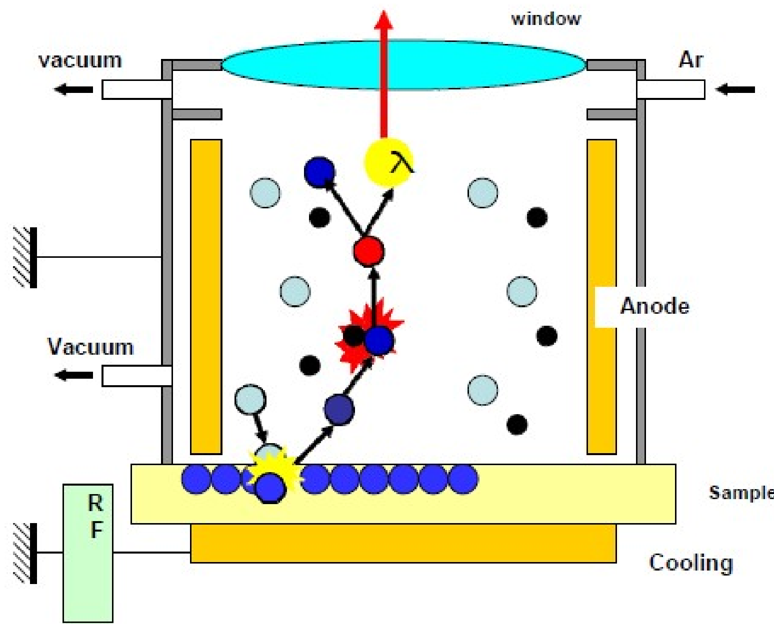

Figure 2.7: A plasma chamber schematic with Ar^+ ions (light blue), attracted to the biased sample, knocking off atoms from the sample surface (dark blue). These sputtered atoms enter the plasma, are excited (red) by collisions with electrons (black), and de-excite by emitting photons of characteristic wavelengths [24].

Each element has a unique set of transition energies between its electronic shells, meaning that every element has a characteristic spectrum of emission lines, some of which fall in the visible range (along with some in UV and IR). The precise photon wavelength produced for a given de-excitation can be calculated from the following equation, where h is Planck's constant, c is the speed of light, and ΔE is the difference between the higher E_2 and lower E_1 energy electron shells [24]:

$$\lambda_{photon} = \frac{hc}{\Delta E} = \frac{hc}{E_2 - E_1} \tag{2.1}$$

These characteristic transitions and resulting spectrum are illustrated in Figure 2.8 for the case of a hydrogen atom. As an example, the electronic transition from

the $n = 2$ state at -3.4 eV to the ground state ($n = 1$) at -13.6 eV corresponds to an emitted photon with an energy of 10.2 eV and a wavelength of 121 nm.

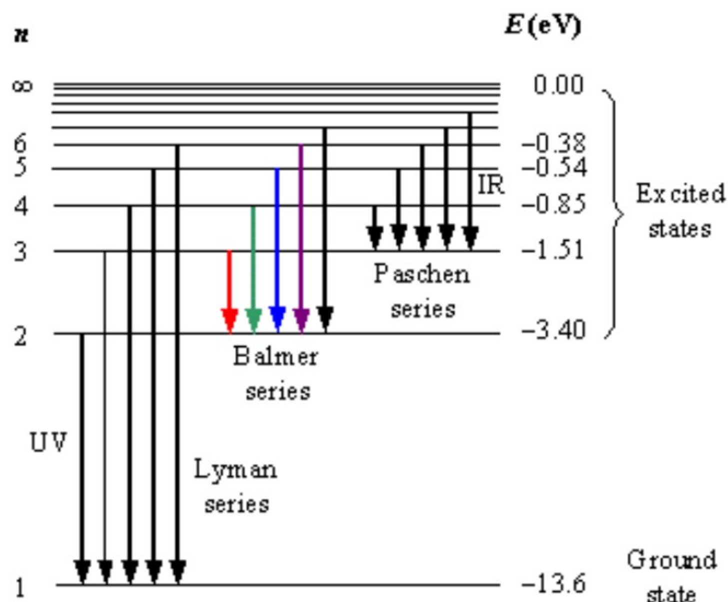

Figure 2.8: Diagram of possible electronic de-excitation transitions for a hydrogen atom [28].

Not all of the sputtered atoms will exist as neutral species in the plasma. Some may have an electron completely stripped away, and these ionized particles will have a different structure of energy levels, producing a different spectrum. In practice, emission from ions ionized two or more times rarely appear in the captured spectrum. Spectral line names have a 'I' appended after the elemental symbol for the case of a neutral atom, and a 'II' appended for a singly-ionized atom [24]. Elements will also vary in intensity amongst their spectral lines depending on how likely different electronic transitions are. A key point is that the intensity (the number of photons) at a given wavelength is proportional to the concentration of a given element in the plasma, which is proportional to the concentration of that element in the sample. This is the link that makes compositional quantification possible in GDOES.

Capturing a full emission spectrum can provide a fingerprint to identify the atom that produced it. Often, it can be sufficient to record the signal at one particular wavelength to determine the presence of an element, especially if no other elements emit strongly near that line.

Both the sputtering process and the optical emission depend on plasma parameters such as pressure and power. The plasma in the chamber is not uniform, and although models exist, it is complex and the various interactions are not all well understood [23, 16]. Nevertheless, plasma-based techniques remain a powerful tool for materials science and characterization.

2.2.3 Spectroscopy

A common polychromator spectrometer arrangement, the Paschen-Runge configuration, is depicted in Figure 2.9. The optical emissions from all the species in the plasma pass through a window at the end of the chamber (a), then through an entrance slit (b) into the spectrometer. The light from the glow discharge chamber is diffracted from a concave grating (c), which splits the light into its component wavelengths. The curvature of the grating defines a Rowland circle, with the focal point of each diffracted wavelength tracing out the circumference of this circle.

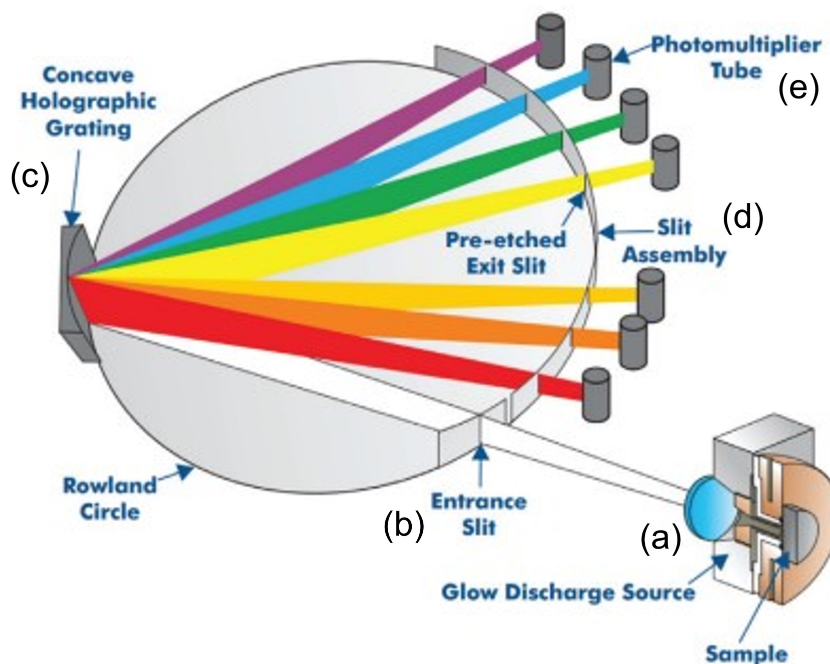

Figure 2.9: A Paschen-Runge spectrometer setup with a Rowland circle geometry. Light from the plasma chamber passes through a window and entrance slit and is incident on a curved diffraction grating. This splits different wavelengths to different angles, where an optical mask allows selected signals to pass to PMT detectors. Only the 1st-order diffraction range is shown here. Adapted from [29].

The grating is usually designed to disperse light in the UV-Vis range. The grating actually diffracts to multiple orders, so a 1st-order spectrum is created over a range of angles, along with a 2nd-order spectrum which partially overlaps the 1st-order (with higher orders possible as well). An optical mask (d) lies around the edge of the circle, with slits positioned to accept wavelengths of interest. The slit positions (i.e. the wavelengths available for analysis) are chosen by the instrument manufacturer. Behind each slit is a photomultiplier tube (PMT) (e) to record the intensity of light at the given wavelength. Where multiple diffraction orders are concurrent on a detector, it must be designed to accept one wavelength and filter out the others. These PMTs must perform over a wide range of signal intensities, as relevant compositions may vary from ppm doping levels up to percentage levels for alloys. Additionally,

consecutive sample layers might feature an elemental signal which alternates between these extremes. Due to the rapid sputtering rate of GDOES, the response from the data acquisition system must be appropriately fast and stable [24].

The raw data collected by instrument allows plotting of intensity (in volts) for selected wavelengths vs. sputtering time (in seconds). Using a one-to-one mapping between a wavelength and an element, software can show (qualitatively), which elements are present, along with trends in their composition, as a function of time.

2.2.4 Further considerations

The preceding discussion has presented the basics of glow discharge optical emission spectroscopy. In practice, there are some other details to be aware of regarding the processes of sputtering, emission, detection, and analyzing GDOES results.

Depth resolution and crater optimization

Returning to the sputtering step, the applied plasma power has a roughly linear effect on sputtering rate and signal intensity. The plasma pressure, on the other hand, influences the shape of the crater, which in turn limits the possible depth resolution [27, 30]. As illustrated in Figure 2.10, the formation of a convex crater (a) indicates that the plasma pressure is too high, whereas a concave crater (c) results from too low pressure. The flat-bottomed crater (b) is optimal and provides the best depth resolution. This is not particularly crucial for a bulk sample, but consider a layered material, such as a film of TiO_2 on a silicon substrate. Near the interface, when the sputtering has nearly eroded the TiO_2 layer, a convex crater shape as in Figure 2.10 (a) would produce a period of time where the silicon substrate signal is generated from the center of the crater, while the edges are still sputtering in TiO_2. The measurement will show an extended region where TiO_2 and Si appear to overlap, even if this interface is supposed to be sharp in reality. The same issue results from a concave crater as in Figure 2.10 (c). This can be particularly problematic if researchers are trying to quantify diffusion across the interface, or use the GDOES profile as a means of measuring layer thickness.

The plasma parameters which produce a flat crater will depend on the material being sputtered. If enough sample material is available, an optimization procedure can be performed, whereby various craters are produced by adjusting the plasma pressure. These craters can then be profiled with a stylus profilometer or optical profiler to see which has the flattest bottom [30, 32]. Alternatively, the depth resolution of an interface can be checked in the GDOES profile itself, noting that a steeper slope at a signal onset indicates better resolution between layers [23]. If multiple layers exist, each with their own ideal plasma parameters, a compromise is required. Non-uniformity of crater shape can also be augmented or reduced at interfaces, according

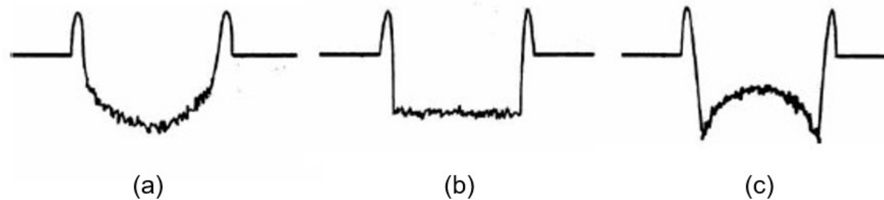

Figure 2.10: Three GDOES crater profiles, where (a) is convex and indicates too high plasma pressure, (b) is the desired flat-bottomed crater, and (c) is concave and indicates too low plasma pressure. Each crater also shows a rim of redeposited material. Adapted from [31].

to differences in the erosion rate between the two layers. For example, if a convex crater reaches a substrate with a lower erosion rate, the edges will start to catch up with the center of the crater.

Shimizu et al. have also reported that depth resolution degrades deeper in the sample. This is due to an edge effect where the periphery of the crater sputters slightly faster, even if the rest is uniformly level. This effect builds over time, such that the best resolutions are achieved at the surface of the sample [27].

Surface (and interface) roughness also influences the achievable depth resolution. Sputter-induced roughening does not seem to be a major issue [25, 27]. Similarly, because of the relatively low energy of sputtering particles, their penetration depth is small (< 1 nm), so sputtering is not expected to cause layer mixing [24, 33, 27].

Optical interference effects

Shifting now to details in the emission and detection processes, the detected intensity can be influenced by the reflectivity of the sample. Assuming isotropic emission from atoms in the plasma, only some fraction of photons pass through the window to the spectrometer. A reflective sample surface, however, can potentially double the intensity of recorded light [25, 34]. According to the dielectric function of the sample, the extent of reflection may vary for different spectral lines.

This effect can lead to a more interesting phenomenon when a thin film is deposited on top of a reflective substrate. If the film is optically transparent in some range of wavelengths, it is possible to observe phase-based optical interference caused by reflection at both the film surface and at the substrate interface. This process is illustrated in Figure 2.11. The signal intensity received at the detector will be the summation of both components, where constructive or destructive interference will modify the amplitude according to the film thickness (h_{layer}) and index of refraction $n(\lambda)$ at the particular wavelength of interest.

Since the sample is continually being sputtered in GDOES, the layer thickness is changing with time, changing the phase shift in a sinusoidal manner and resulting in alternating constructive and destructive interference. The detector records

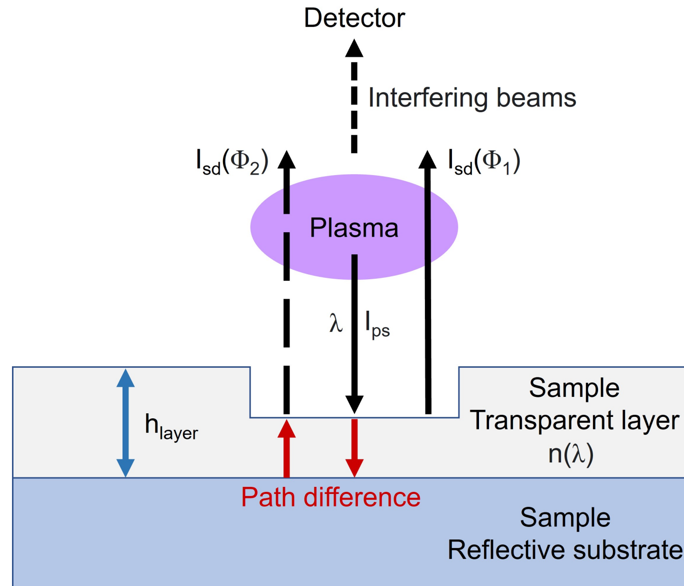

Figure 2.11: The interference effect of optical signals caused by double reflection - at the surface of a transparent layer, and at the interface with a reflective substrate. Light from the plasma incident on the sample surface (I_{ps}) is split into two components which experience different path lengths before reaching the detector (I_{sd}). The corresponding phase difference $\Delta\phi$ enables either constructive or destructive interference.

this as oscillations in the emission intensity. This effect ceases, of course, when the transparent layer is completely sputtered through to the substrate [34, 35].

This effect will be relevant for the PLD samples studied in this work. They have been deposited on a substrate of single-side polished silicon, which is quite reflective. And the deposited film, TiO_2, is transparent in much of the visible range used for GDOES signal detection.

Another factor which can alter detected signal intensity is self-absorption. As emission and absorption are inverse processes, the emission wavelengths of an element will match its absorption edges, so it's possible that particle i_1 in the plasma radiatively emits a photon only to have it be absorbed by another particle i_2 before it reaches the detector. The concentration of sample atoms in the plasma is already small, so trace elements in the sample will not suffer much from this effect. Elements which comprise a major part of the sample composition will be more subject to this signal distortion. Different spectral lines for a given element will also experience self-absorption to different degrees. The issue is more pronounced in resonant emission lines, which have their low-energy transition state at or near the ground state. When possible, it is desirable to use lines with minimal self-absorption to avoid adding complexity to the calibration process described in the following section [24, 33].

Spectral interference is one more aspect to be aware of in optical-emission-based

techniques. Each element selected for analysis is associated with a detector checking at a characteristic wavelength. Interference care arise from overlapping emission lines from other elements or from changes to the background signal due to scattered light inside the spectrometer. Metals, for example, have a rich emission spectrum, of varying intensity [23]. For example, the a common line used for titanium detection is Ti 365.355 nm. Niobium happens to have a low-intensity emission line at 365.1 nm [36]. Depending on the spectrometer and experimental setup, the presence of niobium in a sample could alter the detected titanium intensity, or even suggest the presence of titanium when in fact there is none. A suspected interference can often be investigated by checking a different emission line for the given element (using a monochromator, for instance).

Another common complication regarding emission is the hydrogen effect. Hydrogen is frequently present on the sample surface in the form of adsorbed humidity, and the presence of hydrogen in the plasma can have a strong interfering impact, strengthening the emission of some lines and weakening others [23, 37]. Additionally, hydrogen can alter sputtering rate and crater shape [38, 39]. The mechanisms for this are varied, but include increased plasma collisions as a light element and alterations to the electrical properties of the plasma [40, 41]. This is one reason to address sample surface contamination before measurement. Attempts to correct the hydrogen effect can also be implemented in software.

2.3 Calibration for quantitative GDOES

It is quite clear how to use GDOES to qualitatively detect the presence of different elements in a sample. Even more powerful, though, the application of the technique extends to quantitative analysis, called compositional depth profiling (CDP).

In it's simplest form, the recorded GDOES signal intensity I_i for a given emission line from element i is given by:

$$I_i = k_i \; c_i \; q_M \tag{2.2}$$

where k_i is an emission yield term, c_i is the elemental concentration (typically in mass percent), and q_M is the sputtering rate (in mass per area per time) of the material. The product of c_i and q_M gives the concentration of the element in the plasma, and the emission yield relates the number of atoms in the plasma to the number of photons which reach the detector.

Since quantitative GDOES seeks to determine elemental concentration, Equation 2.2 is inverted to make $c_i q_M$ the subject of the equation. In reality, some other terms are also included. There is an instrument detection efficiency, typically assumed to be constant. A background term b_i is also added to account for the PMT dark current, instrument noise, scattered light, argon emission, and interfering signals from nearby emission lines.

The more complete equation is

$$c_i \; q_M = I_i K_i \; R_i \; S_i \; + b_i \tag{2.3}$$

The emission yield k_i has been inverted and split into a few components: K_i for the constant part of the emission yield (based on the instrument and measurement conditions), R_i for the variable part of the emission yield (subject to change for different samples), and S_i is a correction term for self-absorption [42].

This relation exists for each element i in the sample. For a given element, if K_i, R_i, S_i, and b_i are constant (or nearly constant at the operating point), then $c_i q_M$ forms a linear dependence on I_i.

Knowing that the sum of all elemental concentrations must equal 1,

$$\sum_i c_i = 1 \tag{2.4}$$

a set of equations arises which can relate intensity to concentration and sputtering rate.

2.3.1 Calibration curves

Developing a usable I_i vs. $c_i q_M$ relation relies on determining the slope of Equation 2.3, comprised from K_i, R_i, and S_i. GDOES is a comparative technique, so as opposed to using theoretical or empirical models to compute these terms, they are derived through a calibration procedure. This is typically done with certified reference materials (CRMs) of a known composition. For each element of interest in the sample, a calibration curve must be developed by plotting intensity I_i vs. elemental concentration $c_i q_M$. Thus, several CRMs will be required for each element present, with a concentration range near the expected sample concentration, as well as above and below. After following a consistent experimental method, the measured values of I_i will ideally form a linear trend with $c_i q_M$.

An example iron calibration curve is shown in Figure 2.12. Each data point is a measurement on different aluminum-based CRMs with a small, known concentration of iron. The samples are all of the same aluminum matrix, so the sputtering rate is the same and can be omitted from the x-axis. The y-axis is the intensity detected for the Fe 371.999 nm emission line. The nine points form a clear linear trend. In GDOES measurements of unknown samples, now, the calibration curve can be used to determine iron concentration based on the measured iron emission intensities. Some horizontal error bars are also visible in the plot. This will be explained later in the section.

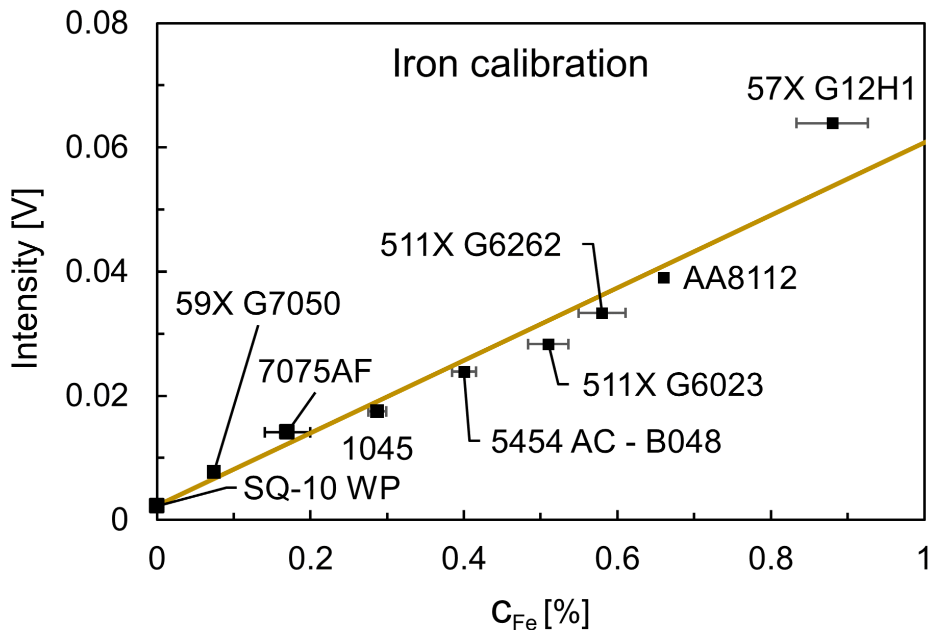

Figure 2.12: An example calibration curve for low concentrations of iron in aluminum samples. Each labeled data point is a GDOES measurement on a CRM, plotting detected signal intensity against known iron concentration C_{Fe}.

The more reference samples available, the greater the quality and reliability of the analysis. A greater number of samples are especially required if the calibration curve appears non-linear. As more elements are introduced in the sample, more references are needed (although one reference might be usable in calibration curves for multiple elements if its composition is similar to the sample of interest). As is apparent from Equation 2.4, calibration is required for all the major elements of a sample in order to achieve accurate results. Omitting calibration for a major element will skew all the remaining concentration calculations. This process can be expensive and time-consuming, depending on the complexity of the sample and the accuracy required [23].

Bulk materials represent the simplest case for the application of the calibration procedure. Besides some deviation at the surface, it is assumed that the sample is more-or-less homogeneous with depth. Thus the sputtering rate, q_M, is constant throughout analysis, so calibration curves can be a function of the form $\mathrm{I_i(c_i)}$ (as in Figure 2.12).

The situation is more complex with surface analysis, thin films, and layered materials. Here, the sputtering rate is subject to vary between different layers. To take this into account, intensity is taken as a function of concentration multiplied with sputtering rate. This raises another point about the selection of reference materials - not only should c_i cover an appropriate range, but the sputtering rate q_M should also be reasonably similar.

For example, consider a sample of bulk Zn with around 10% Ni. It would not necessarily be appropriate to form a Ni calibration curve using a reference sample of stainless steel with 10% Ni, because the overall sputtering rate in steel is much lower than in Zn. Put another way, the intensity of reference sample signals should also be matched appropriately to that of the sample of interest [24].

The sputtering rate is the same for all elements in a given sample. Although preferential sputtering is a factor in the topmost layers of a sample, the composition in the GDOES crater quickly (within milliseconds) reaches an equilibrium such that the sample material sputtered into the plasma is representative of the composition of the sample bulk [33, 42].

The sputtering rate must be disentangled from the elemental concentration at the end of the process. As an extension of Equation 2.4, and an approximated combination with Equation 2.3

$$\sum_i c_i q_M = q_M = \sum_i I_i * constants \tag{2.5}$$

Thus, summing all the elemental intensities gives the sputtering rate (which may vary in different material layers), allowing concentrations to be isolated at any given measurement timestep.

2.3.2 Emission yield

One of the key assumptions in forming a calibration curve is that the various samples are being measured with comparable experimental conditions. This is to fulfill the requirement that the emission yield terms K_i and R_i are constant. The likelihood of optical emission (at a given wavelength) by an atom (of a given element) in the plasma depends on the concentration of ions and electrons in the plasma as well as the collision energy of these particles. A change to the argon pressure influences the shape and distribution of regions in the plasma, and also induces a change in electrical parameters [33]. The emission yield is expected to increase with increasing excitation current, as this creates more electrons for collision in the plasma and generates more metastable argon atoms. The emission yield is expected to decrease with increasing voltage, since the electron collision cross-section decreases at higher energies [23]. The user-set plasma parameters (pressure and power) should be the same for all measurements: on calibration samples and on the analyte samples of interest for quantification.

Even when plasma power is held constant, however, the plasma impedance (the ratio of voltage and current) is subject to change. This can vary according to the secondary electron yield of atoms at the sample surface, meaning that sputtering through layers of different sample material can potentially alter emission yields [23]. Or, the emission yield for a given element may be different in calibration samples of different matrices. This variation can be monitored to a degree by tracking the excitation voltage which the matching box converges to. Subsequent corrections in software are available based on this parameter. This tactic is more difficult to apply for non-conductive samples and RF biasing [43, 42].

As mentioned previously, the presence of hydrogen can also serve to modify emission yields in an inconsistent way for different emission lines. When self-absorption is present, the S_i term must be accounted for. This can be accomplished by using a 2nd-order curve to fit the calibration points.

2.3.3 Sputtering rate

Besides converting signal intensity to elemental concentration on the y-axis, the calibration procedure also enables conversion between sputtering time and depth on the x-axis. Equation 2.5 showed how to calculate the sputtering rate q_M for a sample based on all elemental signal intensities. Integrating q_M over the measurement time results in the total sputtered mass per anode area. Dividing by density allows conversion to depth [24].

The density for a material being characterized by GDOES is likely not known beforehand. It can be determined by measurements of mass and volume (using, for instance, a balance and the Archimedes method) [23]. It is also possible, and typically

easier, to estimate the density according to the elemental concentrations calculated in the calibration process.

For the calibration samples, the sputtering rate should be input along with elemental concentrations as a known quantity. A few methods exist to experimentally determine sputtering rate. A very sensitive balance can be used to measure the sample mass difference before and after sputtering. This is difficult in practice due to the extremely small amount of material sputtered. Assuming a cylindrical crater geometry with a known anode diameter, the change in mass can be converted to sputtering rate. Another method, likely the most common, directly measures the crater depth h by stylus or optical profilometry, and then computes erosion rate (dividing depth by measurement time t) and sputtering rate using the material density (ρ_M, either measured or estimated), as in Equation 2.6 below with any necessary unit conversions.

$$q_M = \rho_M * h/t \tag{2.6}$$

A recent innovation by HORIBA is their "differential interferometry profiler" (DiP), a laser built into the GDOES instrument which allows in-situ depth measurement. The beam is split and directed to spots inside and outside the crater. As the crater deepens, the phase difference between the two beams changes, and this can be converted to crater depth for use in Equation 2.6 [24].

As a way to minimize sensitivity to plasma and instrument parameters, relative sputtering rates (RSR) are often employed instead of absolute sputtering rates. This modifies $c_i q_M$ to become $c_i q_M / q_{Ref}$ or $c_i q_{RSR}$, where q_M is the sputtering rate of the sample matrix compared to q_{Ref}, the sputtering rate of a reference such as pure iron. This is potentially useful during calibration, as it allows reference samples sputtered under different conditions to be incorporated into a single calibration curve [44, 34].

2.3.4 Errors and uncertainty

The accuracy of a quantified GDOES analysis is dependent on a number of factors. When forming the calibration curves, there are three primary sources of uncertainty associated with each data point: uncertainty in the CRM composition and sputtering rate, uncertainty in the measured intensity value, and uncertainty related to the detection limit for the particular emission line being used [23].

The first uncertainty pertains to the placement of the data point on the x-axis, $c_i q_M$. The CRMs may come with a manufacturer certificate specifying an uncertainty range in the composition. If this is not provided, the uncertainty for each element in a sample is simply estimated based on the concentration of that element (i.e. a major element will have a larger absolute uncertainty than a trace element). The uncertainty in sputtering rate is also factored here. This is typically estimated from

the standard deviation in crater depth calculated from multiple different profilometer line scans. Any uncertainty in density would be included here as well.

The second uncertainty relates to fluctuation in the measured intensity, I_i, on the y-axis. To determine the intensity of a particular elemental signal, the GDOES profile is typically averaged over a time range where the measurement appears stable. In addition to obtaining this average value of the signal, one can also compute the standard deviation of the signal intensity. This uncertainty is mapped onto the x-axis to easily aggregate with the other uncertainty sources.

The third uncertainty is not linked to the particular CRM or measurement, but rather acknowledges that very weak signals may become indistinguishable from background noise, depending on the detector response.

These uncertainty sources are independent, so the total standard deviation for a calibration data point is taken as the square-root of the sum of each term squared. The largest single source of uncertainty will dominate the total term. It is reported that the sputtering rate calculation by crater depth measurement is often the primary source of error, with a typical relative standard deviation (RSD) in the range 5-10% [34].

2.3.5 Curve fitting and application

When all calibration samples have been measured and their composition and sputtering rates have been documented, the final step is to fit a function to the data. Most commonly, this means performing a method-of-least-squares regression to achieve a linear fit. With an uncertainty estimate for each calibration data point, a weighted regression is possible. The smaller absolute uncertainty associated with lower concentration, lower intensity data points often results in a curve that appears to favor this lower range, possibly at the expense of missing higher concentration points. Depending on the anticipated analyte sample concentration, a weighted regression can be chosen to emphasize lower concentrations or an unweighted regression can be chosen to emphasize higher concentrations [45].

Additional fitting parameters can be included, intended to correct various interferences or differences in measurement conditions. Higher order curves can also be used to fit non-linear data. Care must be taken when deciding to apply these curve alterations; they can often improve the data fit, but there should be a specific reason to justify their use [33, 24]. Ideally, the set of calibration curves will be validated against additional CRMs which were not used in the calibration. This provides an opportunity to evaluate the accuracy of the calibration and tune it for improvement.

To summarize the process of compositional depth profiling:

- Select and acquire reference materials appropriate to the elements and concentrations in the analyte sample(s) of interest
- With known elemental concentrations and (relative) sputtering rates, record GDOES measurements (using the same experimental conditions) on each calibration sample to generate data points I_i vs. $c_i q_{RSR}$
- Develop a calibration curve for all relevant elements by regression
- Record a GDOES measurement on the sample of interest, using the same experimental conditions as the calibration measurements
- Convert measured intensities I_i into $c_i q_{RSR}$ according to the calibration curves
- Sum $c_i q_{RSR}$ for all i to get overall relative sputtering rate q_{RSR}
- For each element i, divide $c_i q_{RSR}$ by q_{RSR} to acquire elemental composition c_i
- Multiply by the absolute reference sputtering rate q_{Ref} to get absolute sputtered rate q_M
- Integrate q_M over time to get sputtered mass
- Divide by density and anode area to convert to depth
- Result: profile of elemental concentrations (at% or wt%) vs. depth

2.4 Pulsed laser deposition

Before moving on to the Methods and a description of various fabricated samples, it will be useful to take a brief look at the pulsed laser deposition (PLD) process. PLD is a thin film deposition technique in which short, energetic laser pulses are fired at a material, called a target. Material from the target surface is ablated and ejected in a highly-directional plasma plume. A substrate is mounted opposite the target such that the plume material will be incident and deposit in a thin layer on the surface. Consecutive pulses of the target builds up the cumulative deposited layer thickness on the substrate [46]. This simplified description is illustrated in Figure 2.13.

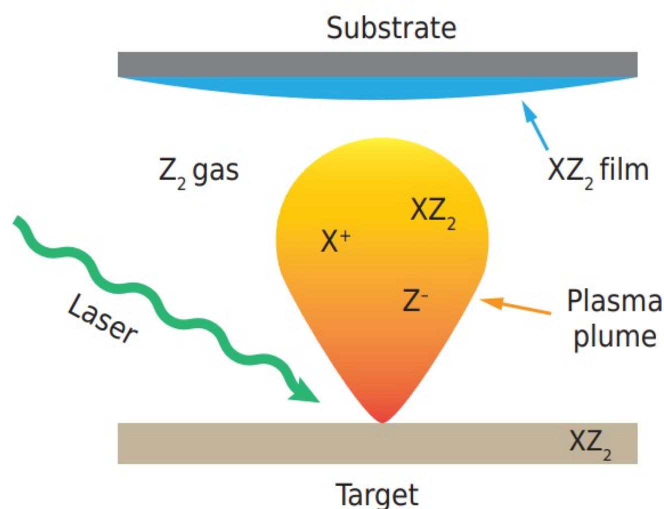

Figure 2.13: Diagram of PLD process. A bulk target (of material XZ_2) is ablated by a pulsed laser beam. A plasma plume results, ejecting a variety of energetic species. The vacuum chamber may have some background gas pressure influencing the plume spread and reactions (here Z_2). Some particles of the plume reach the substrate and adsorb on its surface. These steps are repeated to create a thin film of desired thickness. Figure taken from [47].

Of course, a variety of factors influence this process. The shape and spread of plume material reaching the substrate surface area is not completely uniform; the highest-energy particles are found at the plume center, and this region will also be thickest in the layer transferred to the substrate. If a flat film of homogenous thickness is desired, the substrate can be shifted to some optimal position relative to the plume and rotated during deposition. The entire process takes place in a vacuum chamber in order to minimize external contamination and facilitate transfer of material from the target to the substrate. Some controlled flow of background gas (either inert or reactive) is also a possibility, though, which can affect the film growth process and resulting structure and composition. Additional parameters to tune the deposition include substrate temperature, laser fluence and frequency, and target-substrate distance. The benefits of this technique include the ability for stoichiometric transfer of material from target to substrate, and precise growth control [47, 48].

An extension of PLD is the use of multiple targets during deposition, termed combinatorial PLD. Besides allowing for new material combinations, one version called natural spread combinatorial PLD (nc-PLD) also takes advantage of the non-uniform plume shapes to deposit a film with a spatial gradient in composition. This process is depicted in Figure 2.14: A target (of material α) is positioned toward the left side of the substrate. After laser excitation, the resulting plume ablation is skewed toward the left side of the substrate, depositing more material in a distribution around the plume center (marked $\times_1$). A second target (of material β) is positioned at the right side of the substrate, with its material deposition distribution similarly shifted (around plume center $\times_2$). A layer formed by pulsing both targets at their respective locations will have a concentration gradient from majority α near $\times_1$, to majority β near $\times_2$, with some ratio of $\alpha_a\beta_b$ in between. Many cycles of this process creates a thin film, layer by layer, with an equivalent gradient. Various parameters can be adjusted to control the final film composition and thickness profile. Regarding the investigation of (Cr+N) co-doped TiO_2, the main benefit of using nc-PLD is the ability to fabricate samples with a continuous compositional spread (CCS). A single CCS sample allows study of the effects of a range of doping concentration on the film's optical and crystallographic properties [48].

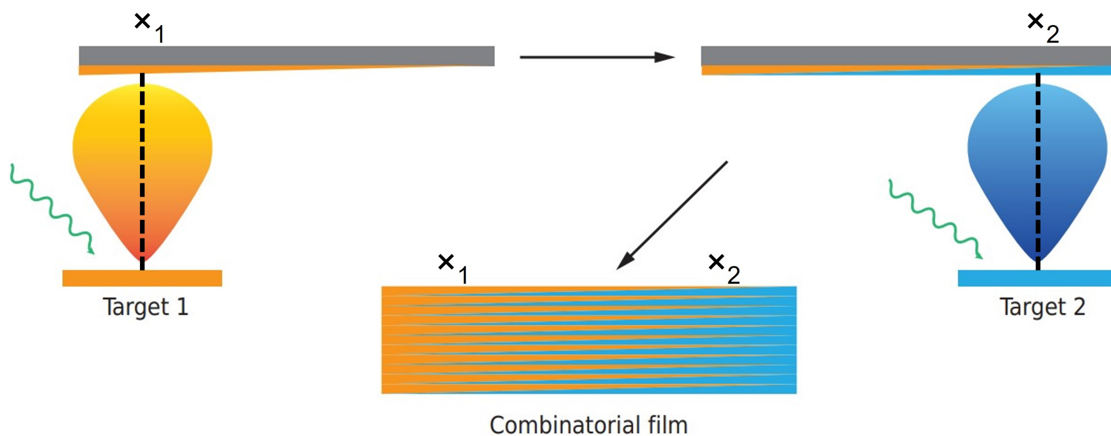

Figure 2.14: Schematic of natural spread combinatorial PLD. Materials from multiple different targets are deposited at different locations on the substrate. $\times_1$ and $\times_2$ mark the plume center positions of two different targets. The distribution of material from each plume results in a continuous compositional spread between the locations of the two plumes. This overall gradient is preserved as new layers are deposited with each successive cycle to build up to the desired film thickness (as in the side-view shown bottom-center) [48]. Figure adapted from [47].

Chapter 3

Methods and Experimental Details

The following chapter includes sections adapted from the author's previous specialization project [1]

This chapter begins with information about the fabricated PLD samples which are the materials of interest for GDOES analysis. In order to perform the calibration procedure for quantitative results, samples of known composition are required. The reference samples used in this work are described and key elemental concentrations are provided. Next, the project-specific context of the GDOES instrument and measurement procedures are provided. Besides outlining the process for a typical GDOES measurement, some additional details are given regarding a useful pre-measurement surface cleaning function. The important process of developing calibration curves in the Quantum GDOES software is elaborated. Finally, two sections discuss the method of GDOES crater profiling by means of stylus profilometer and 3D optical profiler. Associated data processing steps are also described.

3.1 Samples

3.1.1 Fabricated samples

The PLD samples described in this section were synthesized by Hogne Lysne and Thomas Brakstad as part of their PhD work.

A complete description of the PLD method will not be given here, but an overview of the deposition parameters for each film may be useful. More details can be found, for example, in the 2022 publication by Lysne and Brakstad et al. [48].

As mentioned in Section 2.1, the group seeks to realize an IB material by co-doping TiO_2 with Cr and N. As a recap of Section 2.4, PLD is an accessible method for material prototyping, and a doping effect can be achieved by using multiple targets for a deposition (combinatorial PLD). Natural spread combinatorial PLD (nc-PLD) involves sequentially ablating two target materials, depositing different material distributions centered at two different locations on the wafer. The fabricated film features a continuous compositional spread (CCS), with a greater concentration

of one material at one position, a greater concentration of the second material at the other position, and a gradient in concentration in between. This is well-suited to study different doping concentration levels [49]. The two targets in this case are TiO_2 and CrN, ablated separately to control the amount of doping.

For the CCS films, it would be most convenient to deposit in the same chamber environment for the whole process. However, previous studies by the group (such as ellipsometry and Raman spectroscopy [49, 50]) found significant formation of Cr_xO_y phases when ablating CrN in an O_2 background gas, with minimal nitrogen transfer to the film. Deposition purely in N_2 was also problematic when ablating from the TiO_2 target, as the film's crystalline quality degraded and there was evidence of TiO_xN_y [47, 51]. An O_2 background gas is best suited for TiO_2 formation and a N_2 background gas is best suited for Cr and N doping. In response, a gas cycling scheme was developed, adding time and complexity to the deposition method, but intended to result in more stoichiometric material transfer to the sample and higher-quality films. All PLD samples in this work were deposited on 2" (50.8 mm) diameter p-type silicon <001> wafers [52].

3.1.1.1 PLD plume films

One prior achievement of the group was the development of a simulation tool to accurately predict the transfer of target material to the substrate, dependent on various PLD parameters [48]. This involved several depositions using either a TiO_2 or CrN target onto a non-rotating substrate, followed by mapping the resulting film thickness by variable angle spectroscopic ellipsometry (VASE, or simply *ellipsometry*). These films were also useful to study the influence of deposition parameters such as background gas (O_2 or N_2), gas pressure, substrate temperature, and substrate position. A non-rastering laser system was used, so the plume position relative to the substrate was fixed throughout deposition.

The samples created in these depositions reflect the non-uniform transfer of material from the PLD ablation plume onto the substrate. The deposited film captures variations in the plume such as material distribution and kinetic energy of adatoms (both greater at the plume's center). As such, these samples are termed PLD "plume" films. This title distinguishes them from combinatorial PLD films or films made with substrate rotation, both of which achieve a more uniform thickness across the wafer. Two PLD plume film examples are pictured in Figure 3.1, with visible GDOES craters.

Many of these samples had already been characterized in an assortment of other ways (Raman spectroscopy, X-ray diffraction (XRD), atomic force microscopy, in addition to ellipsometry) so they were available for GDOES measurement, despite its inherently destructive outcome. Most of the 2" wafers had been cut into smaller pieces subject to a size limit for XRD measurements.

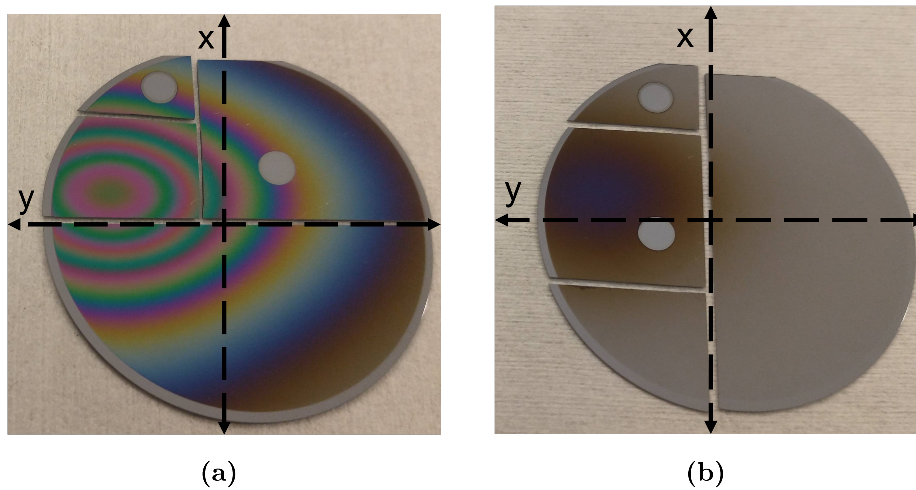

(a) (b)

Figure 3.1: (a) Sample P-TiO_2-O-700, one of several PLD samples created to study the TiO_2 plume distribution. (b) Sample P-CrN-N-cy-O-700, a CrN-based plume film. The circular marks are sites where GDOES measurement has sputtered through to the underlying silicon substrate. The wafers were previously cleaved into chips small enough for XRD measurement. x- and y-axes are overlaid to show the coordinate orientation used during deposition.

For the PLD plume films, which utilized only one material target at a time, gas cycling was still included for some samples, to get a sense of how O_2 exposure might affect the films deposited in N_2. The details of the cycling procedure are as follows: the single target would be ablated by some number of laser pulses in a N_2 environment (equating to a few angstoms of film thickness), followed by 20 seconds of waiting for stabilization. Then, the chamber atmosphere would be flushed out, and O_2 introduced for a period of 30 seconds without any deposition. After flushing out the O_2, N_2 would be reintroduced for the next round of pulsed deposition, with a 20 second waiting time for stabilization. This sequence would then be repeated for the total number of desired pulses. The substrate temperature was also varied (either 700°C or 550°C) for different sample depositions, as this can influence the TiO_2 phase and crystalline quality, as well as the incorporation of nitrogen into the film [49].

A summary of the PLD plume film samples and their deposition parameters follows in Table 3.1. The naming convention uses: P for plume, TiO_2 or CrN to denote the target material, O or N to denote background gas, N-cy-O to indicate deposition in N_2 followed by a pause in O_2, and finally 700 or 550 for the substrate temperature in °C. No sample rotation took place during deposition, and the substrate shift in each case was at its default position relative to the target location: x=0.33 cm, y=1.63 cm.

Table 3.1: A summary of the PLD parameters used for deposition of various plume and flat film samples. T is the substrate temperature. When O_2 is indicated, the gas pressure is 1.3 x 10^{-2} Torr. When N_2 is indicated, the gas pressure is 1.6 x 10^{-2} Torr. N_2 / O_2 means that deposition took place in N_2, but periodic waiting stages in O_2 also took place. Pulses is the total number of laser pulses on the PLD target, corresponding to the film thickness.

Sample	T [°C]	Gas	Pulses
P-CrN-O-700	700	O_2	40,000
P-CrN-N-cy-O-700	700	N_2 / O_2	30,800
P-CrN-N-550	550	N_2	40,000
P-TiO_2-O-700	700	O_2	15,000
P-TiO_2-O-550	550	O_2	5,000
P-TiO_2-N-cy-O-700	700	N_2 / O_2	5,000
P-TiO_2-N-cy-O-550	550	N_2 / O_2	5,000

3.1.1.2 PLD flat films

While the PLD plume samples were fabricated to improve the PLD simulation and study deposition parameters, future samples would ideally have a flat, uniform film thickness. This was investigated by rotating the sample during deposition and adjusting the substrate position relative to the deposition plume. Two such films were used in this GDOES work, one with the substrate at a default position, and another with an optimized shift. Visual inspection of the thickness fringes in Figure 3.2 already allows a qualitative comparison of film thickness uniformity, and ellipsometry was used to quantify the results. The rainbow-colored sample in (a) was used in some earlier

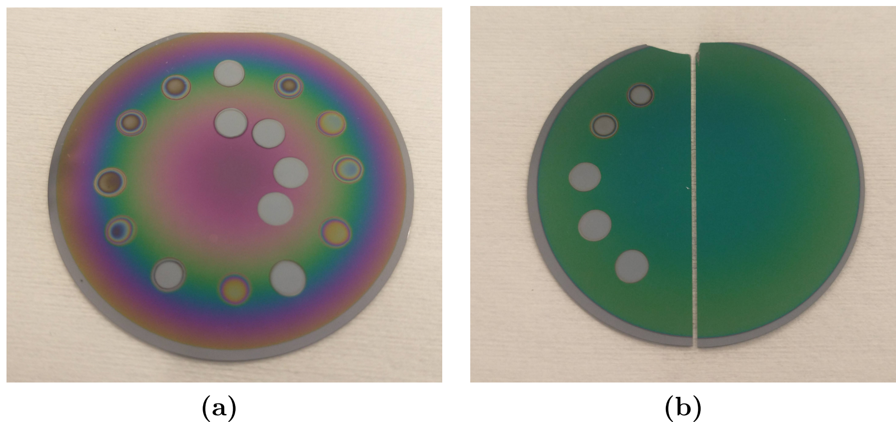

(a) (b)

Figure 3.2: Two samples with a thin film of TiO_2 deposited by PLD on a 2" silicon wafer with sample rotation. The film in (b) has a more uniform thickness thanks to optimized substrate positioning. It will be discussed again later as a calibration sample. The (b) wafer was cleaved in half before any measurements.

GDOES experiments and will not feature further in this work. The green sample in (b) (named F-TiO_2-O-700-opt, for optimized flat film) was included as a calibration sample assuming a nominal stoichiometry of TiO_2 and anatase phase. To fabricate this sample, the substrate was rotated at 29 °/s while pulsing the TiO_2 PLD target 36,000 times in an O_2 background. The substrate temperature was 700°C, and the substrate shift was (0.00, 2.80) cm.

3.1.1.3 PLD CCS films

The samples described so far have been fabricated using a single target material. These final samples employ the CCS approach explained in Section 2.4, with ablation from both TiO_2 and CrN targets, taking place at two positions on the substrate. Position 1 is used to describe the arrangement where PLD target ablation takes place with a substrate shift of -1.3 cm (the left side of the wafer). Only TiO_2 ablation in O_2 takes place at position 1. The position 1 plume center is denoted $\times_1$. Position 2 refers to ablation with a substrate shift of +1.3 cm (the right side of the wafer). Various nc-PLD steps take place in this arrangement, such as CrN ablation in N_2, TiO_2 ablation in O_2, and also TiO_2 ablation in N_2. The position 2 plume center is denoted $\times_2$. The positions were chosen according to the simulation results for a level thickness across the center line. Note that although deposition is centered at $\times_1$ for position 1, material is deposited across the entire wafer to some degree, consistent with the distribution observed in the PLD plume films. Likewise for deposition in position 2.

The desired Cr and N concentrations were only up to 10 at%, so TiO_2 ablation was also required at position 2 in order to deposit sufficient host material and obtain an even film thickness between $\times_1$ and $\times_2$. This was done by alternately rotating the substrate at 0°and 180°, allowing ablation from the TiO_2 target for the substrate oriented in both positions 1 and 2.
An example CCS film is pictured below in Figure 3.3 (although this particular sample did not receive GDOES measurement).

The first of these CCS films was deposited purely in O_2. Figure 3.4 displays the simulated thickness (along a central rectangle of the wafer) resulting from a single loop of nc-PLD steps. (a) is a top-down color thickness map, with the plume centers marked ($\times_1$ and $\times_2$). The overlaid red contour lines are simulated Cr (or N) doping levels, at 3, 5, 7 and 9 at% from left to right. (b) is a side-view of how the layer thickness is built up from different nc-PLD steps at positions 1 and 2. For this CCS film, 400 loops result in the total pulse numbers listed in Table 3.2.

As mentioned previously, though, CrN ablation in O_2 was found to introduce undesirable Cr_xO_y phases. The gas cycling scheme allows ablation of CrN in a purely N_2 environment. However, it was discovered that the just-deposited layer of Cr and N was altered merely by exposure to the O_2 gas used in the subsequent TiO_2 ablation

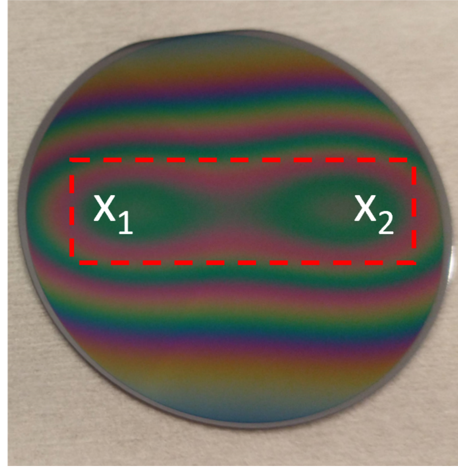

Figure 3.3: A PLD sample fabricated with a continuous compositional spread (CCS). The thickness fringes indicate that the horizontal center line has a mostly uniform thickness. The vaguely ∞-shaped fringe roughly outlines the positions of plume centers $\times_1$ on the left and $\times_2$ on the right. The dashed red rectangle marks the region where PLD simulation was used to optimize film thickness uniformity and tailor the doping concentration range.

stage. A "capping" step was therefore included to address this, where the TiO_2 target was additionally ablated in N_2 at position 2 to protect the underlying layer of Cr and N with a thin layer of TiO_xN_y before cycling back to O_2 for the majority of the TiO_2 ablation (at both positions 1 and 2).

A reference CCS film was fabricated where the CrN ablation was omitted, allowing independent study of the effect of the TiO_2 capping layer. The design of the nc-PLD steps is given in Figure 3.5, showing (a) the simulated thickness map and (b) the sequence of deposition layers within a single loop. No red doping contours are included, because there is no CrN ablation.

And finally, a CCS film was fabricated including pulses from both the TiO_2 and CrN targets, plus the gas cycling and capping layer. The corresponding simulated thickness map and constituent nc-PLD steps are presented in Figure 3.6, with the doping contours included again in (a) for 3, 5, 7 and 9 at% Cr and N levels.

A comparison of these three CCS samples is given in Table 3.2, with the total number of pulses from each target in each background gas at each position.

The goal of this thesis work is to quantify the Cr and N doping concentrations at different locations on the CCS films. GDOES quantification requires comparison to calibration samples, which will be presented in the following section.

Table 3.2: A summary of the PLD parameters used for deposition of various CCS samples. T is the substrate temperature. Pulses in O_2 took place at 1.3 x 10^{-2} Torr. Pulses in N_2 took place at 1.6 x 10^{-2} Torr. Pos. 1 denotes a deposition plume centered at -1.3 cm on the substrate, and Pos. 2 denotes a deposition plume center at +1.3 cm.

Sample	T [°C]	Pulses in O_2			Pulses in N_2	
		TiO_2	TiO_2	CrN	TiO_2	CrN
		Pos. 1	Pos. 2	Pos. 2	Pos. 2	Pos. 2
CCS-O-700	700	10,400	8,800	18,000	0	0
CCS-Cap-NoCr	550	10,400	4,800	0	4,000	0†
CCS-Cap1	550	10,400	4,800	0	4,000	36,000

† As a placeholder for the CrN ablation step, this sample featured a 9-second wait in each loop.

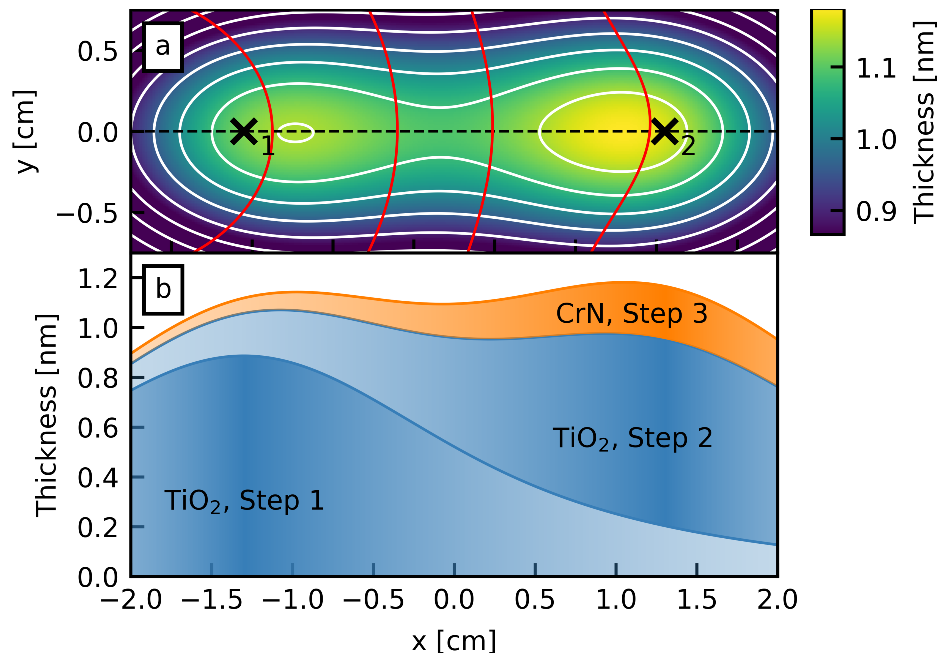

Figure 3.4: (a) Simulated thickness map for CCS-O-700, for $\frac{1}{400}$ of the pulses listed in Table 3.2, where $\times_1$ and $\times_2$ indicated the positions of the plume centers at -1.3 cm and +1.3 cm, respectively. The simulated Cr and N concentration is plotted as red contour lines, that from left-to-right represent 3 (near $\times_1$), 5, 7, and 9 at% (near $\times_2$), respectively. GDOES measurements will take place outside the bounded region shown here. (b) Simulated (cumulative) material spread along the dashed center line in a). Material from the TiO_2 target in blue, and material from the CrN target in orange. Figure taken from [49].

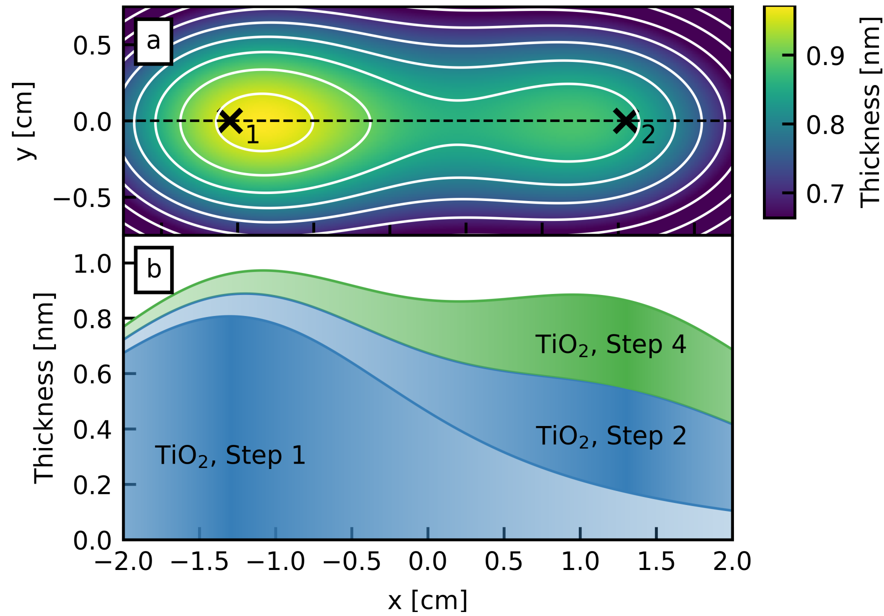

Figure 3.5: (a) Simulated thickness map for CCS-Cap-NoCr, for $\frac{1}{400}$ of the pulses listed in Table 3.2, where $\times_1$ and $\times_2$ indicated the position of the plume centers at -1.3 cm and +1.3 cm, respectively. GDOES measurements will take place outside the bounded region shown here. (b) Simulated (cumulative) material spread along the dashed center line in a). Material from the TiO_2 target deposited in an O_2 atmosphere in blue, and in N_2 atmosphere in green (the capping). Figure taken from [51].

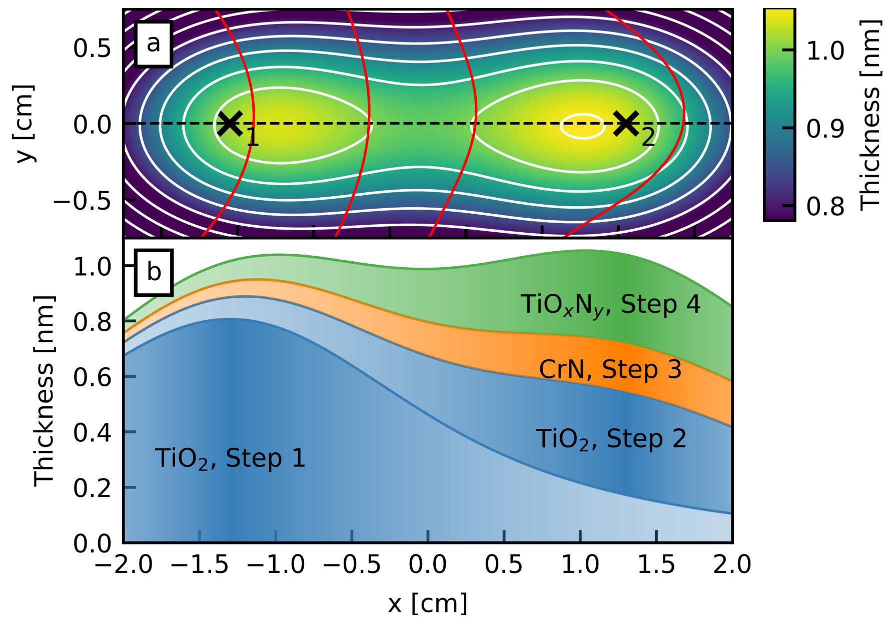

Figure 3.6: (a) Simulated thickness map for CCS-Cap1, for $\frac{1}{400}$ of the pulses listed in Table 3.2, where $\times_1$ and $\times_2$ indicated the position of the plume centers at -1.3 cm and +1.3 cm, respectively. The simulated Cr and N concentration is plotted as red contour lines, that from left-to-right represent 3 (near $\times_1$), 5, 7, and 9 at% (near $\times_2$), respectively. GDOES measurements will take place outside the bounded region shown here. (b) Simulated (cumulative) material spread along the dashed center line in a). Blue layers: material from the TiO_2 target deposited in an O_2 atmosphere. Green layer: material from the TiO_2 target deposited in an N_2 atmosphere (capping). Orange: material from the CrN target deposited in an N_2 atmosphere. Figure taken from [51].

3.1.2 Reference samples for calibration

As noted in Section 2.3, any attempt at quantitative GDOES analysis requires comparison against samples of known composition (preferably CRMs). Purchasing these CRMs can become expensive [23], and they are not always available with the desired elemental concentrations, especially for non-metallic materials [53]. A limited selection of CRMs with relevant elements were already available in the lab. Some others were borrowed from Horiba's GDOES lab in France. Other samples included were nominally pure, or have an expected composition, which were not confirmed by other characterization methods, but included nevertheless with admission of some possible uncertainty range. All calibration samples are listed below along with some relevant details. Table 3.3 follows with relevant elemental concentrations (in weight percentage). Most samples are pictured in Figure 3.7.

- **1045 aluminum** - CRM, sourced from Pechiney. Included for silicon content. Metallic disk.
- **1766 low-alloy steel** - CRM, sourced from NIST. Contains no elements of interest in relevant concentrations, but serves as the NTNU GDOES lab reference sputtering material as mentioned in Section 2.3.3. Metallic disk.
- **AlN** - Borrowed from Horiba. Ceramic sheet.
- **C276 Hastelloy** - Obtained from NTNU Finmekanisk verksted. Included for chromium content. Metallic disk. The elemental concentrations for this alloy are specified within a range of a few percent. When defining the sample in the Quantum software, elemental concentrations were set at the middle of their range, with the accuracy field set to encompass the max and min possible values.
- **CE650 aluminum-titanium-oxide** - CRM, sourced from Swerea Kimab. Included for titanium and oxygen content. Ceramic disk.
- **Chromium** - Borrowed from Horiba. Metallic disk.
- **CrN PLD target** - A packed-powder puck of CrN for PLD target ablation. Originally sourced from Stanford Advanced Materials [54], but no longer listed on their website. Contact with a sales representative instructed that the product density is in the range 85-90% of solid CrN. This density range introduces uncertainty in the calculated sputtering rate, which must be factored when inputting software values. There was some question, following receival of the target, if the composition might actually be Cr_2N, a material which *was* listed on the site. The representative assured that the composition was CrN as ordered. Despite this, some of the results will be interesting to consider in the context of Cr_2N. In this case, the relative concentrations of Cr and N are shifted and a different material density is used.

- **JK49 high-alloy nitrogen steel** - CRM, sourced from Swerea Kimab. Used for diagnostic checks prior to all GDOES measurement sessions at the NTNU lab. Included for chromium and nitrogen content. Metallic disk.
- **Quartz (SiO_2)** - Obtained as scrap from NTNU Glassblåserverkstede. Thin rectangular slide.
- **Silicon** - 2" silicon wafer used as deposition substrate in PLD lab. Additionally, some of these silicon wafers were also used for a number of tests where a deposited film was not required, so there was no need to waste a crater spot on the limited PLD samples. The wafers were sourced from University Wafers. They are ID#444, <001>-oriented, p-type (B-doped), 0-100 Ω-cm resistivity, 320-350 µm thick, single-side polished, and test grade quality [52].
- **Titanium** - Obtained as scrap from NTNU Finmekanisk verksted. Grade 2 purity. Metallic plate.
- **TiN** - Borrowed from Horiba. TiN coating on Co-Cr alloy. Metallic disk.
- **TiO_2 PLD flat film (F-TiO_2-O-700-opt)** - As described in the previous section, this sample is a PLD product of TiO_2 ablation in an O_2 environment while rotating the substrate. The decision to include it as a reference sample for calibration is motivated by the need for more oxygen-containing samples. Its titanium and oxygen content have not been directly confirmed by another method. However, Raman spectroscopy found clear evidence of anatase peaks [50]. Additionally, the model resulting from ellipsometry measurement places the absorption edge around 3.4 eV , which is in agreement with reported values for the bandgap of anatase TiO_2. Nevertheless, without being able to confirm the sample's elemental concentration by a more direct method, a generous uncertainty range of 10% of concentration was set in the software. The material density was input as 3.78 g/cm^3, in line with anatase.

Additionally, some other samples were considered for use as calibration samples, but were ultimately not used. These include a TiO_2 PLD target which failed to adequately form a vacuum seal, and a strontium titanate ($SrTiO_3$) substrate and aluminum oxide (Al_2O_3) substrate which both fractured during measurement, likely due to thermal stress [55].

Table 3.3: All calibration samples, along with their weight percentage of selected elements. Some other major elements are also listed, including the concentration of the primary constituent. The sample source is also listed, although only a few were CRMs.

Sample	Concentration [wt%]					Other	Source
	Ti	**O**	**Cr**	**N**	**Si**	**major**	
1045	0.255	-	-	-	8.02	Al (90.5%)	[56]
1766	-	-	-	0.02	0.01	Fe (99.8%)	[57]
AlN	-	-	-	34.2	-	Al (65.8%)	Horiba
C276	-	-	16.0	-	0.08	Ni (54.6%), Mo, Fe	Metal lab [58]
CE650	22.0	34.0	-	0.27	-	Al (38.0%), C	[59]
Cr	-	-	100.0	-	-	-	Horiba
CrN	-	-	78.8†	21.2 †	-	-	[54]
JK49	-	-	5.0	1.89	0.5	Fe (75.6%), V, Mo	[59]
Quartz	-	53.3	-	-	46.7	-	Glass lab
Si	-	-	-	-	100.0	-	[52]
Ti	100.0	-	-	-	-	-	Metal lab
TiN	77.4	-	-	22.6	-	-	Horiba
TiO_2	60.0 ‡	40.0‡	-	-	-	-	PLD lab

† For the Cr_2N version, Cr is 88.1% and N is 11.9%.

‡ Assuming a stoichiometric 1:2 atomic ratio of Ti:O in the fabricated film.

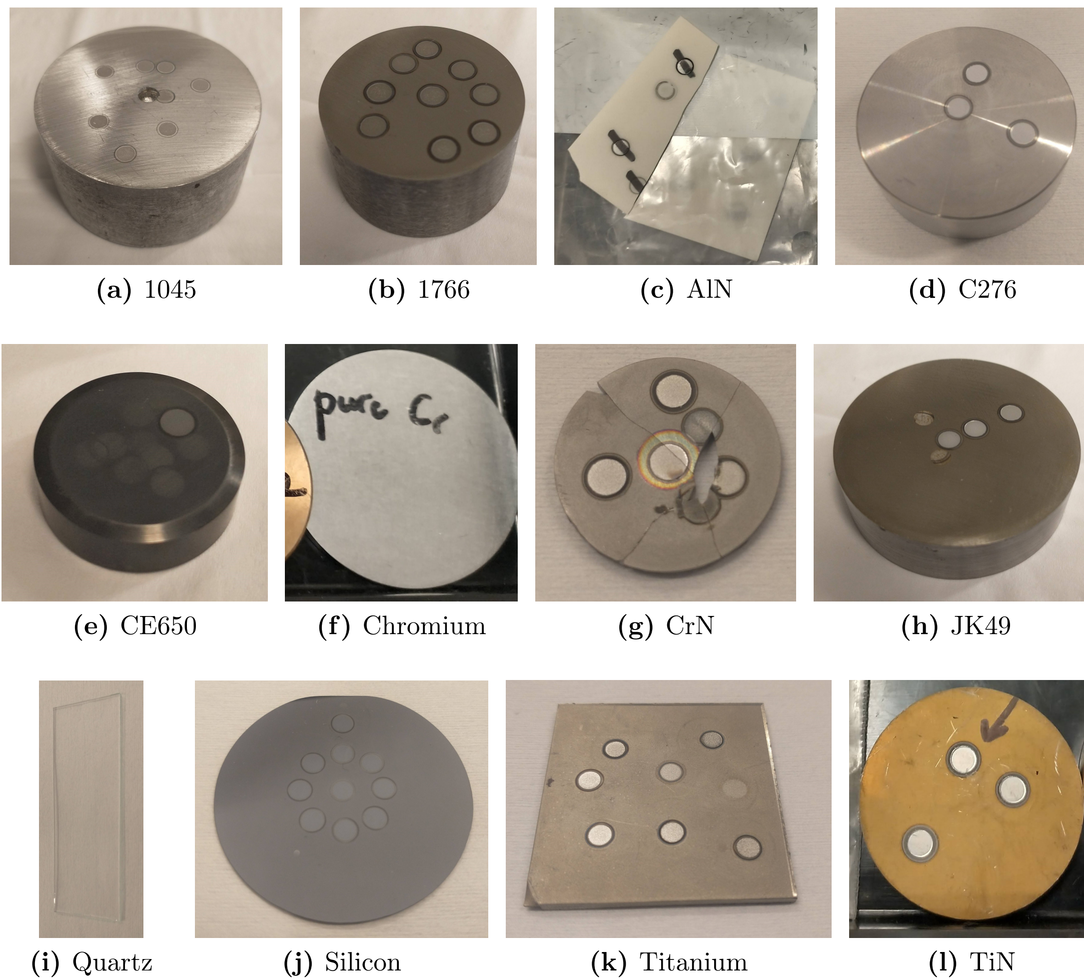

(a) 1045 **(b)** 1766 **(c)** AlN **(d)** C276

(e) CE650 **(f)** Chromium **(g)** CrN **(h)** JK49

(i) Quartz **(j)** Silicon **(k)** Titanium **(l)** TiN

Figure 3.7: Photographs of all samples used for calibration (except the TiO_2 PLD film, already pictured in Figure 3.2 (b)). Prior GDOES measurement craters are visible on most of the samples.

3.2 GDOES measurements

3.2.1 Equipment

The equipment used in this project is a GD-Profiler 2 by HORIBA Jobin Yvon (pictured in Figure 2.3). It is maintained by the Department of Materials Science and Engineering at NTNU. The plasma gas is argon, and the anode is copper with a 4mm diameter. The system is also equipped with HORIBA's differential interferometry profiling, DiP, which employs a laser (at $\lambda = 635$ nm) for in-situ crater depth measurement. The anode and DiP opening are visible in the sample mounting surface in Figure 3.8 (a).

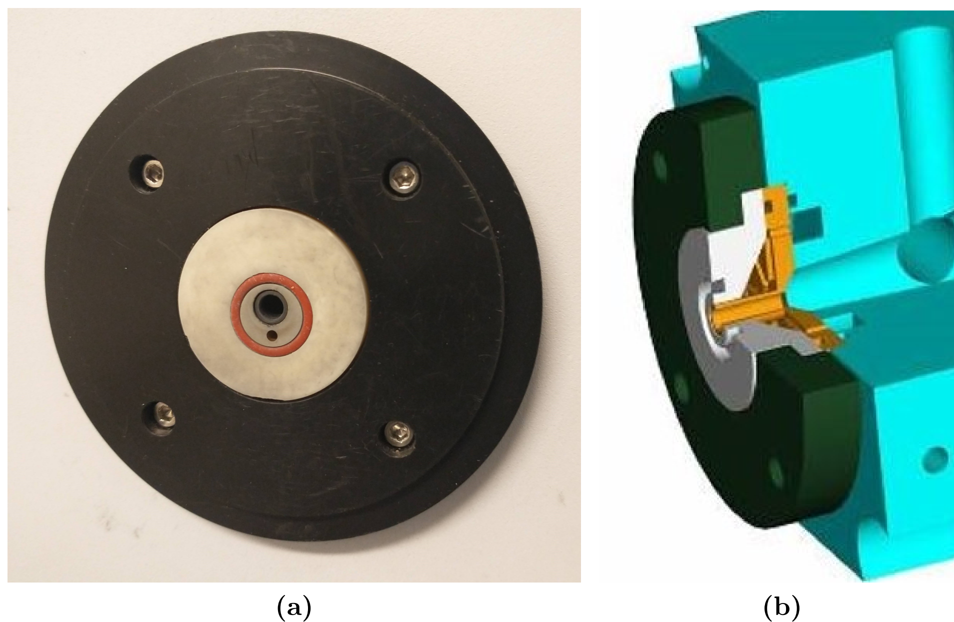

(a) (b)

Figure 3.8: (a) An image of the GDOES chamber sample mounting pad. At the center is the anode tube and a small hole for the interferometry laser. These are surrounded by an O-ring and white ceramic material. (b) A schematic cross section of the sample mounting pad, showing the copper anode tube extending back and comprising the plasma chamber. Adapted from [60].

The plasma source operates in RF mode, with a matching box that automatically adjusts two variable capacitors to minimize reflected power. A pulsed mode was introduced for this instrument somewhat recently, which decreases the average power but maintains high instantaneous power for sputtering. This has proven advantageous for fragile or heat-sensitive samples [61]. It has also been reported that this can improve depth resolution and enhance elemental sensitivity [26]. On our instrument, use of the pulsed mode is incompatible with the automatic matching box, requiring the capacitors to be manually set to their optimal value before starting. Additionally, the corresponding synchronized acquisition setting (recording data only during the pulses of plasma power) is not available with our hardware, resulting in profiles which

appear messy with high-frequency spikes.

Two oil rotary pumps are used to generate the vacuum seal and flush the plasma during operation. A water cooling circuit is built into the cathode block that contacts the back of the sample and holds it against the anode. The chiller is set to 15°C. The transfer optics systems is comprised of two MgF_2 lenses which allow light from the plasma chamber to the spectrometer. Over time, the window out of the plasma chamber can become dirtied with sputtered material, causing a gradual decline in recorded intensities [23]. Cleaning the window is possible as part of periodic technician maintenance, but this was not performed during this semester work.

The spectrometer utilizes the Paschen-Runge setup. The entrance slit is 20 µm and makes an incident angle of about 52° with the grating. The concave polychromator diffraction grating has 2400 lines/mm, diffracting into three orders around the Rowland circle. This covers a spectral range from about 120-600 nm. The exit slits on the optical mask are pre-determined by HORIBA, with widths between 35-50 µm. Slits intended to collect emissions in the range 250-500 nm are positioned to use the 1st-order diffraction. Shorter wavelengths are collected at their 2nd-order diffraction angles. The zero-order diffraction (a lower-intensity reflection of all incident light) is directed to a separate parabolic grating which is used to focus longer wavelengths. 47 channels are available for simultaneous measurement. The detectors are termed High Dynamic Detectors (HDD), and are essentially photomultiplier tubes (PMTs) with automatic adjustment capability of their supplied voltage to accommodate potentially large swings in intensity. Due to the spatial overlap of 1st- and 2nd-order diffraction angles for some wavelengths, some detectors employ a filter to block out unintended contributions to the signal from emission lines at $\frac{1}{2}$ or 2 times the wavelength. The spectrometer also includes a monochromator (making use of the zero-order spectrum) mounted with a Czerny-Turner configuration. This can be calibrated to any wavelength for simultaneous measurement with the polychromator. It can also record the full optical spectrum of a bulk sample over the course of a two-minute measurement. Nitrogen is used for continuous flushing of the optical system. Atmospheric O_2 and H_2O absorb in the UV range, which would weaken some spectral lines before they reach the detector.

The instrument is controlled and data is recorded via HORIBA's Quantum software (v2.12) [45]. For each measurement, a "method" is selected, specifying which elements to check for (which spectral lines), the plasma parameters (power, pressure), flushing time, background acquisition time, pre-integration time (used to reach steady-state in bulk materials), an option for pulsed source operation, an option for soft plasma cleaning, and if an associated calibration function exists.

The instrument was operated in constant pressure/constant power mode, leaving the plasma impedance (voltage and current) as a free parameter. The plasma and acquisition settings were adjusted over the course of the work. However, the applied

power was typically 25 or 40 W, the pressure was typically 700 Pa, the longest acquisition time was 600 seconds, averaging was usually 0.05 s/pt (20 points per second), background acquisition was 5 seconds, flushing consisted of one 40-second cycle, and no pre-integration was used. The spectral lines analyzed for the elements of interest are: 365.355 nm for Ti (I), 130.223 nm for O (I), 425.439 nm for Cr (I), 149.267 nm for N (I), and 288.162 nm for Si (I). The parenthetical (I) after each element indicates that the emission line comes from the neutral state (not ionized) atom. A complete table listing the polychromator spectral lines paired with each element is included in Appendix Table A.1.

3.2.2 Measurement procedure

After turning on all the equipment, the first steps before a measurement session always begin with calibration. A pure aluminum sample is used to center the polychromator (according to the Al 396.157 nm line). The anode inner wall is cleaned with a reaming tool (pictured in Figure 3.9 (a)), and the mounting surface is cleaned with dry, lint-free tissue paper. This attempts to remove contamination from previous measurements.

The sample mounting procedure involves placing the the point of interest up against the anode and starting the pumps to hold the sample in place. To achieve a sufficient seal, samples must be flat and rigid and large enough to cover the O-ring surrounding the anode (approximately 13 mm diameter). The sample forms the final wall of the plasma chamber. The rear electrode block is placed up against the back of the sample (which must also be flat and parallel with the front surface) and held in place by a Teflon-coated piston arm (as in Figure 3.9 (b)). After closing the chamber cover, the evacuated plasma tube is filled with argon gas to the specified pressure.

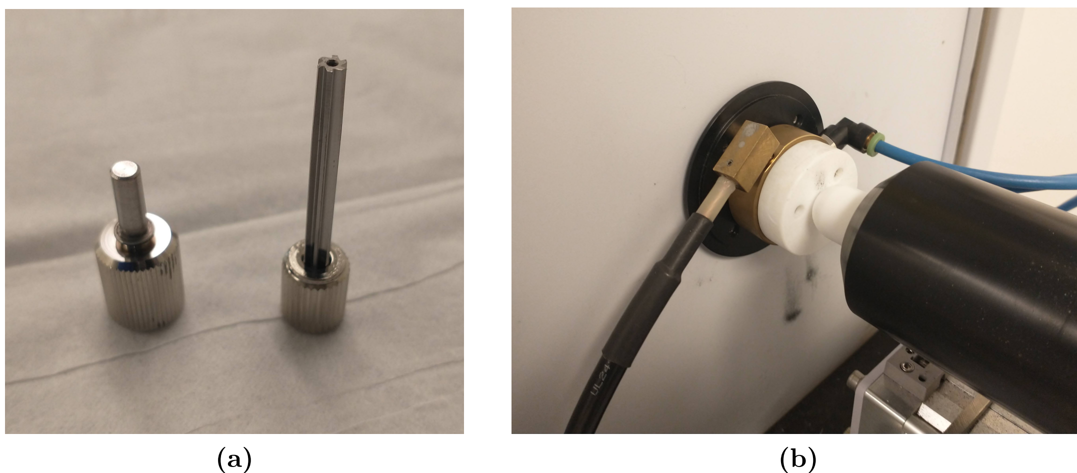

(a) (b)

Figure 3.9: (a) Two reaming tools used to clean out the inside of the anode. (b) A sample mounting arrangement in the GDOES chamber, where the RF power and cooling block contacts the sample backside and is held in place by a piston arm.

Measurements typically begin with a flushing cycle of alternating low and high pressure intended to clean the sample surface to a degree. This is followed by a period of background measurement, where detector (HDD) signals are recorded with no source excitation. The background signal for each channel is subtracted from the subsequent measurement. For bulk samples, a pre-integration time is included, where the sample is sputtered (according to the specified plasma power and pressure parameters) for a few seconds to stabilize the plasma, remove any surface contamination or oxides, and reach a representative steady state. The measurement then proceeds with the same plasma parameters for a specified period of time or until the operator stops the process. The number of data points collected depends on the setting of how long to average the signal (in milliseconds/point). This is a trade-off between recording a smooth signal and capturing sufficient details in the profile. The polychromator centering uses a particular method which runs automatically and notifies the user of the offset since the previous calibration. This value is recorded for diagnostic use if necessary.

Next, the polychromator is profiled using a standard steel sample (JK49) [59]. The aluminum sample is removed by releasing the piston arm and venting the vacuum. A circular mark is clearly visible on the sample surface where the sputtering took place. The anode and mounting surface are cleaned as before, and the steel sample is mounted. Again, the polychromator profiling uses a special method different from a typical measurement. For diagnostic purposes, the maximum and minimum signal intensities for a selected set of elements is recorded. Over the course of the semester, the primary iron signal ranged between 11.4 V to 9.4 V, generally trending downward with time. This may be due to gradual contamination of the spectrometer window. Finally, a simple check is performed by running a surface analysis on the steel sample just to see that the signals are stable and reasonably close to expected values.

In the previous specialization project work [1], 3D printed wafer alignment templates were used to position the 2" PLD samples over the anode in a systematic manor. The measurement naming convention carries over from this template, with pt. 01 corresponding to wafer center, pts. 02-09 forming a ring 8.45 mm radial from the center, and pts. 10-21 forming an outer ring 16.9 mm radial from the center. A schematic map of all labeled crater points possible using these templates is illustrated in Figure 3.10.

Many of the PLD samples were already cleaved into smaller pieces for other characterization work. This limited the use of the alignment templates and also constrained which positions were possible to measure. The identifying number for such measurements is typically based on the nearest position to the 21 points shown in Figure 3.10.

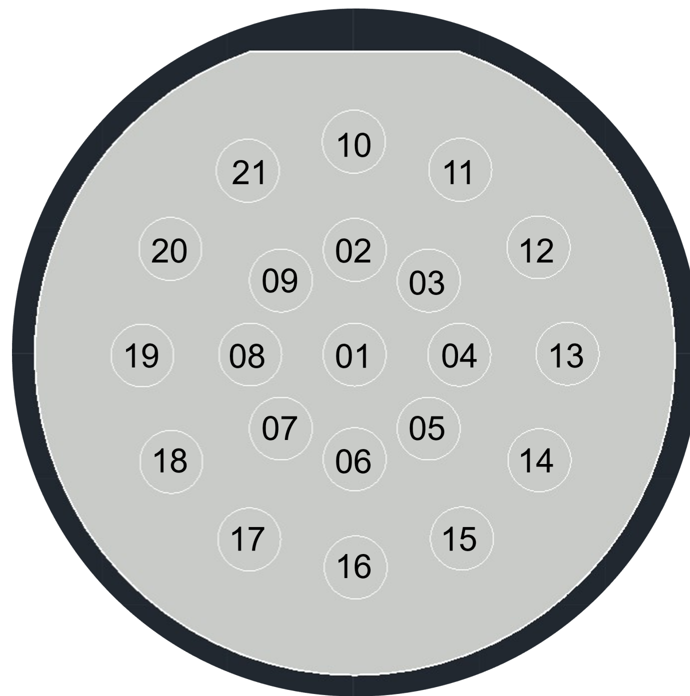

Figure 3.10: Labeled crater points, as positioned by template 1 for point 01, template 2 for points 02-09, and template 3 for points 10-21. Note the wafer flat oriented at the top.

The calibration samples have a variety of shapes and dimensions, so no templates were designed for systematic placement. Measurement locations were estimated by eye to avoid overlapping previous craters. The calibration measurements presented in the next chapter are simply numbered chronologically (i.e. pt. 01 was measured before pt. 02, etc.) without regard to position on the sample. As bulk materials, the composition is expected to be uniform around each sample after sputtering past the surface.

3.2.3 Low-power plasma surface cleaning

The Quantum software includes an option for surface cleaning prior to surface analysis. This generates a low-power "soft" plasma in which bombarding argon ions are too weak to sputter the sample atoms, but, in combination with the gas flow, can help dislodge surface contaminants for a cleaner subsequent analysis [62]. The plasma settings available for surface cleaning are the same as in a normal measurement: power (typically 5 W or less, either pulsed or continuous), pressure, and application time. The spectrometer is active during surface cleaning and the results are displayed (enabling a visual check that the sample surface is not being sputtered) but not saved. After surface cleaning, the normal measurement immediately proceeds according to the parameters set in the method.

For the sake of recording potentially useful information, an alternative to this

built-in function is the creation of a separate method which specifies a low bias power. This allows the surface cleaning measurement results to be saved. Some experiments in this work made use of this dedicated-method plasma cleaning measurement. The cleaning method parameters were typically identical to the associated normal method, with the exception that the power was reduced to 5 W. In contrast to the built-in plasma cleaning, the minimum input power for a user-created method is 5 W. Pulsed mode was also used to ensure the sample surface was not being unintentionally sputtered. Analysis time was typically 60 seconds.

3.2.4 Calibration curve formation

A database of calibration samples is maintained within the Quantum software, where data must be entered for each samples' elemental composition (in weight fraction (wt%), ppm, or atomic percentage (at%)), density, and relative sputtering rate. An accuracy field is optionally included if the concentration uncertainty for elements in a sample are known [45].

As detailed in Section 2.3.3, relative sputtering rates (RSR) are preferable to ease transfer of results between methods and experimental setups. When the RSR for a sample is already known, it can simply be entered in the software. If the RSR is determined experimentally (in the course of calibration measurements, for example), then the erosion rate (µm/min) is entered (as determined by profilometry or another method). This is converted to a sputtering rate ($g/m^2/s$) by multiplying by density as in Equation 2.6. Using the same plasma conditions, a measurement must be made on the chosen reference (1766 low-alloy steel in our lab). The calculation then proceeds from crater depth to erosion rate to sputtering rate for the reference. An accuracy field is also available alongside the RSR input for each sample, to address variations stemming from different crater measurements. This value input here is calculated from the standard deviation of depths from multiple line scans of the same crater. Both the compositional and sputtering rate accuracies factor into weighting of points for the regression construction of calibration curves, explained in Section 2.3.5.

When all reference samples are entered into the database, they must be assigned within the settings for the GDOES method, and then measured using the parameters of that method. As a note, the calibration sample details are not fixed at this point. For example, there is no issue if a sample is initially defined in the database without knowing the RSR. This can be added later, after a measurement has been made on the sample. Ideally, the samples are measured within a single session to minimize changes in the experimental conditions. In this work, various samples were considered for calibration, and experiments were done over the course of the semester, so the best measurements were chosen after seeing each profile.

A time range is selected for averaging elemental intensities within each measure-

ment profile where all signals are stable. This was typically the last 30-120 seconds of the measurement. The standard deviation of signal intensity is also automatically assigned as one of the uncertainty components described in Section 2.3.4 Along with the sample sputtering rate q_M, the resulting signal intensity for each emission line I_i is paired with the previously defined elemental concentrations for that sample c_i. That is to say, one data point is created for the Equation 2.3.

Once all samples specified within a method have been measured, computation of the calibration curves can proceed. For each element i which is included in the composition of at least one calibration sample, all $I_i = c_i q_M$ data points are plotted together. A linear regression fits a curve amongst all measurement points, with stronger weighting for points with smaller uncertainty in elemental concentration and sputtering rate.

When calibration curves for all relevant elements have been generated, modified, and accepted, the method becomes calibrated. All measurements taken using this method (including previously stored measurements) can now apply a "CDP" button to the qualitative results to follow the conversion process explained in Section 2.3 to transform signal voltage to elemental concentration, and sputtering time to sputtering depth.

3.3 Stylus profilometer measurements

As noted in Section 2.3.3, a direct measurement of crater depth is a common method to determine a sample's sputtering rate, q_M, a necessary component in the quantification equations.

For many of the GDOES measurements taken, and for all measurements on calibration samples, a contact stylus profilometer was used to acquire line scans across the resulting crater. A MarSurf M 400 unit is available in the same lab as the GDOES instrument. It is connected to an SD 26 drive unit and BFW-250 probe system. The specified measurement speed is 0.2 mm/s, the measuring range is ±25 µm, and the profile resolution is 0.8 nm [63]. A scan length of 8 to 12 mm was chosen to cover the entire 4 mm diameter crater plus sufficient margins on either side for leveling. Since the instrument only reveals the profile of a linear slice across the crater, multiple measurements (at least 5) were typically made of a single crater from various angles, all passing through the center. Most samples presented a mostly flat surface with varying degrees of roughness.

Data processing

The MarSurf outputs data as a text file, with some metadata at the top and calculated parameters at the bottom, and the middle lines populated by raw measurement results. All results were copied to a spreadsheet for uniform data processing. This

involved leveling the profile (a linear leveling according to values averaged over a range at the start and end), vertically shifting the area surrounding the crater to a height of zero, and centering the crater for easy comparison between measurements.

For samples with rougher, less-polished surfaces, some averaging across points was used to smooth out the profile. Some measurements included anomalous features, such as spikes from dust particles, trenches from scratches, overlap with other craters, or curvature from non-uniformity of the original sample surface. After visual examination of each profile, such atypical measurements were excluded from further analysis.

All GDOES tests were performed with the 4 mm anode, so all craters have this same diameter. The depth of each crater was calculated by considering the range -1.9 to +1.9 mm around the centered crater scan. Not all scans cross exactly through the crater center, so some measurements show a crater spanning slightly less than 4 mm. The 2D line scan represents a 3D surface by sweeping around a circle. Thus, the edges of the scan sweep a larger area than the center; to evenly average the depth at all points in the 2D scan would not accurately represent the average depth over the 3D crater. Rather, the scan is averaged over smaller segments, which are weighted according to their radial distance before summing. The difference in these calculation methods is negligible for a perfectly flat crater, but the error grows for craters which are deeper at the center (convex) or edges (concave) [23].

The average crater depth was used to compute a sputtering rate for each sample, following Equation 2.6. The relative standard deviation in depth measurements was used as input for the RSR accuracy field.

3.4 Optical profiler measurements

In addition to the stylus profilometer, many craters were also examined using a 3D optical profiler, specifically a Bruker ContourGT-K maintained by NTNU's NanoLab.

Optical profilometry uses the wave properties of light, especially phase, to extract data of surface topology. A coherent light source is split into two paths - one to a reference, and one to the sample. The reflections from each of these paths recombine at a detector, where interference is possible due to differences in the path length. The reference path has a fixed length, so any interference is a result of features or variations in the sample surface height. A mode exists which uses monochromated light, but this work employs white-light interferometry (WLI, or vertical scanning interferometery, VSI). The 3D optical profiler also incorporates a microscopic objective lens such that very small sample areas can be imaged. When the sample surface is in focus (i.e. the stage height is adjusted to match the lens focal length), the detector shows interference fringes which follow the contours of the sample. Different elevations of the sample will be in focus at different stage heights, allowing the software

to map the surface profile according to the positions of maximal fringe contrast [64]. The instrument can provide nm resolution for height differences up to several µm.

With a 4 mm diameter, the GDOES craters are rather large features. With the weakest objective lens (2.5x), the instrument's field of view is approximately 2.0 x 1.5 mm. However, the software has a built-in stitching functionality, allowing multiple profiles to be combined into one larger image. Approximately 20% overlap is specified between frames, so a 9 x 1.5 mm image is an aggregation of 1 row x 6 columns. As with the stylus profiles, scans across the crater in at least two directions (horizontal and vertical) were usually performed with the optical profiler. Many of the craters failed to measure properly just at the sharp crater rim (i.e. no height was recorded). This doesn't affect the depth calculation within the however.

Data processing

The Bruker software has a built-in planar leveling function which was applied before exporting the data. For convenient comparison with the stylus profilometer results, line scans were taken from the optical profiles in the software Gwyddion [65]. The scan results were transferred into the same spreadsheet as mentioned before. The optical scan data received a similar treatment of edge-zeroing, crater centering, and radially-weighted depth calculation.

Chapter 4

Results and Discussion

The main results of this work were 1) the calibration procedure intended for compositional quantification of PLD-fabricated thin film samples, and 2) the GDOES measurements of various PLD-fabricated thin film samples. Some other findings related to these results are additionally presented, such as a low-power measurement for prediction of atmospheric nitrogen signals, and attempts to generate additional calibration data points from the limited number of calibration samples.

4.1 Nitrogen signal consistency

One of the primary motivations for using GDOES for elemental characterization of these samples was the purported sensitivity to nitrogen. However, a recurring challenge was the inconsistency of nitrogen signals between repeated measurements on same sample which are expected to have the same composition. For instance, using the same plasma parameters, measurements at two spots on the same silicon wafer (points 07 and 08, presented in Figure 4.1) detected average nitrogen signal intensities of 7.8 mV and 19.1 mV, respectively, more than a factor of 2 difference. Both signals are low compared to the primary 0.26 V silicon intensity, but nevertheless, such uncertainty is problematic given that small quantities of nitrogen (0-10 at%) are of interest for the doped CCS samples.

For samples like silicon, where no nitrogen content is expected in the bulk, possible sources of nitrogen include contamination in the argon gas source or supply line, leakage from the spectrometer chamber, or atmospheric leakage through the O-ring seal due to insufficient sample placement or surface roughness. Spectral interference is another hypothetical possibility; for the N 149.267 nm line collected at its 2nd-order diffraction angle, possible interferences include Cu 148.864 nm and Cr 144.843 nm, plus the 1st-order angle from Cu 296.116 nm, Cr 298.647 nm, and Fe 298.357 nm [36]. The nitrogen signal is effectively absent in some measurements (as expected), so the issue does not appear to be systematic, nor necessarily related to the sample

itself. This also rules out contamination from the argon supply and optical chamber, as these would presumably be constant from one measurement to the next (when all instrument settings are otherwise the same). The anode is made of copper, but it is not expected to be sputtered to any significant degree, and such a contribution would also seem to be somewhat stable across measurements. Further, the detector for the Cu 324.759 nm line is typically recording a negligibly small signal for copper. Metallic contamination (Cr or Fe) from prior samples is possible, but this effect would be confined to the surface and should be identifiable by the dedicated detectors for these elements.

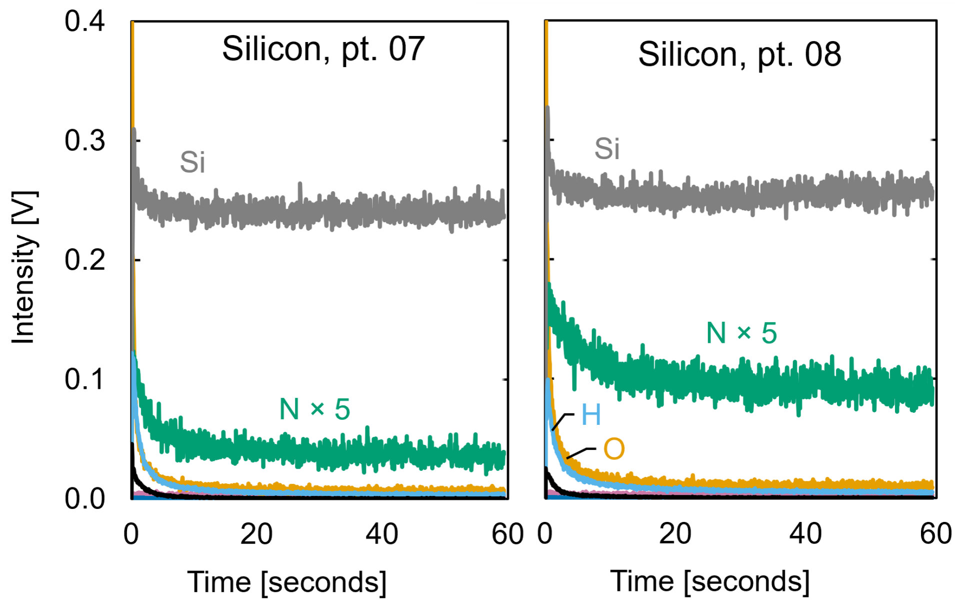

Figure 4.1: A comparison of two GDOES profiles of the same silicon wafer, where the nitrogen intensity differs.

The explanation which seems most likely for variable nitrogen levels between measurements is sample placement and the sealing of the plasma chamber. The pressure regime typical of GDOES is in the hundreds of Pascals, and the instrument's pressure sensor is appropriate for this scale. Thus, when mounting a sample and sealing it against the anode, no granularity is available to distinguish between a pressure of 0.1 Pa and 0.01 Pa. Either the chamber is at vacuum level (0 Pa) or it is not. This enables the possibility that two apparently identical measurements are actually experiencing slightly different levels of atmospheric leakage. Avoiding any leakage altogether would be preferable, but finding a way to assess leakage prior to sample sputtering could be a satisfactory alternative. While the current vacuum system is not suited for such a determination, the spectrometer could be applied for this purpose.

Low-power measurement for atmospheric leakage prediction

As mentioned in Section 3.2.3, a 5 W GDOES method was created to emulate the "soft" plasma surface cleaning recommended in the literature. As the plasma and spectrometer are active in this low-power method, it seemed possible that the detector signals recorded might, in addition to showing contaminating surface elements, give an indication of atmospheric leakage. The gas pressure in this method was set identical to that used in the full-power method (700 Pa), so a similar degree of atmospheric influx might be expected compared with the full-power measurements. Crucially, the low-power measurement is performed with the intention of *not* sputtering the sample surface. Thus, if the low-power measurement were to suggest unacceptable atmospheric nitrogen levels stemming from sample placement, there would still be a chance to reposition the sample before proceeding to a destructive full-power measurement. Any effect related to the surface cleaning outcome of this treatment is incidental.

This approach was tested initially with measurements on a silicon wafer to see if there was any correlation between the nitrogen intensity during the low-power measurement and the nitrogen intensity during the subsequent full-power measurement (without adjusting the sample mounting at all in between). As expected, the nitrogen signals in the low-power method were extremely small, ranging from 0.5 to 5.0 mV. They did, however, seem to form a rough linear correlation with the nitrogen intensity recorded in the following full-power measurement, giving reason to pursue the method further.

A low-power measurement taken on one of the PLD flat films (F-TiO_2-O-700-opt) revealed a non-zero titanium signal when using the 5 W power (shown in the left plot of Figure 4.2). To avoid any risk of sputtering the sample surface, the low-power method was adjusted to use the pulsed mode (with software default values: frequency = 33 Hz, and duty cycle = 0.0625 for an effective applied power of 0.3125 W). The resulting plot (shown in the right plot Figure 4.2) has signal intensities at the magnitude of detector background levels, affirming that the sample surface is effectively free of sputtering.

After this point, all GDOES measurements (both for calibration samples and for PLD samples) were preceded by a pulsed low-power measurement to infer adequate sample placement. As a way to compare between different samples, the nitrogen signal for a given measurement was normalized by the total light entering the spectrometer - a recorded parameter F_i, the total intensity of luminous flux [45].

In Figure 4.3, the full-power $\frac{N}{F_i}$ is plotted against the low-power $\frac{N}{F_i}$ recorded in each GDOES measurement. On a log scale, an upward trend is visible. Across all sample types, the data points form a loose distribution. Within a particular sample type, comparisons to previous measurements provide a simple predictive power. For example, in one measurement on F-TiO_2-O-700-opt, the low-power relative nitrogen

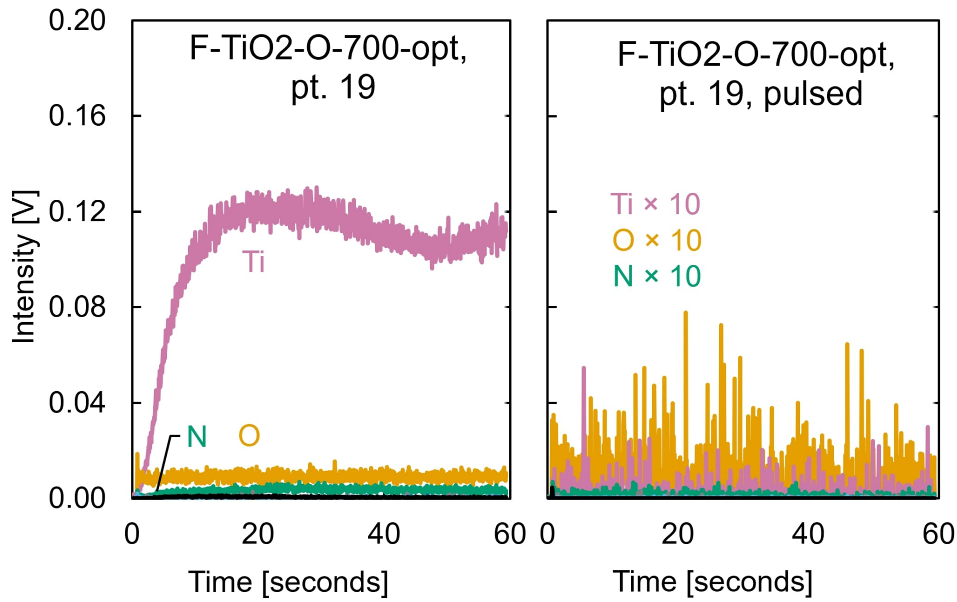

Figure 4.2: A comparison of two low-power GDOES profiles at the same spot on a TiO_2 PLD film. In the left, using an applied power of 5 W, the titanium signal is large enough to indicate sample sputtering. In the right, using a pulsed power (5 W peak), no sputtering is evident.

was 6×10^{-4} and the resulting full-power value was 15×10^{-4}. In another measurement, the low-power relative nitrogen was 4×10^{-4}, suggesting that the sample seal was at least as good as before. In this instance, the corresponding full-power level was indeed smaller, at 9×10^{-4}. Of course, some of the samples actually contain nitrogen (green triangles in Figure 4.3), so a larger full-power nitrogen level is found relative to their low-power prediction, which only takes into account the contribution from atmospheric nitrogen.

Once a sample has been measured once in this way, future low-power measurements become a useful diagnostic. If the relative nitrogen value is smaller than previous, the full-power measurement can proceed with some confidence of minimal atmospheric contamination. If the relative nitrogen is larger, however, the sample can be repositioned until the low-power measurement records a satisfactory nitrogen signal.

Figure 4.3: The relative nitrogen levels (nitrogen intensity divided by total flux intensity) from a low-power measurement (5 W pulsed, absent of sample sputtering) approximately forecasts nitrogen levels in a full-power measurement.

4.2 Calibration measurements

In this section, the GDOES profiles for all calibration samples are presented. Multiple measurements were typically taken, the first to get a sense of what to expect from the particular sample, and subsequent ones to acquire a stable profile suitable for the calibration curves. Only the final measurement used for calibration is presented here. Only minimal comments will be included, as the profiles generally reflect the expected composition. Although the instrument records signals for over 40 elements, only relevant elements will be shown. Some strong metal emission signals are scaled down to better see in relation to weaker signals. Ti (color-coded pink), O (orange), Cr (dark blue), N (green), Si (gray), H (light blue), and C (black) are included in all plots, although the signals are not always strong enough to be visible. Table 4.1 at the end summarizes the measurement time range selected for calibration curve input and the average signal intensities for Ti, O, Cr, N, and Si.

Additionally, each GDOES crater was measured by stylus profilometer and/or optical profiler for the purpose of calculating sputtering rates. As mentioned in Section 3.3, multiple measurements were made on each crater (a minimum of 5), but a single representative plot will be given here, paired with its corresponding GDOES profile. The crater shapes vary in quality because the plasma parameters are not optimized for each sample, but rather must be fixed according to the values chosen for the fabricated PLD samples. Since these calibration samples are mostly bulk materials, the crater shape is not so important. In any case, the repeated scans generally display a similar crater shape and depth. Table 4.2 lists - for all samples - the average crater depth, relative sputtering rate, and relative standard deviation from multiple measurements.

4.2.1 GDOES profiles and craters

1045 aluminum

The GDOES profile for the 1045 aluminum CRM is plotted in Figure 4.4; it is dominated by the aluminum signal, as expected. It appears to have a slight positive slope even at three minutes of measurement, suggesting that the crater shape has not quite reached an equilibrium yet. However, the silicon signal, which is why this sample was included for calibration, seems stable.

A representative crater profile for the 1045 CRM is plotted in Figure 4.5. Its shape is convex, with rounded edges, suggesting that the applied pressure (700 Pa) is higher than ideal for this material. Recall that the plasma conditions are chosen for the TiO_2 PLD samples, and the optimal parameters for different calibration samples might not be similar. The surface roughness reflects the course mechanical polishing of the sample, observable by visual inspection.

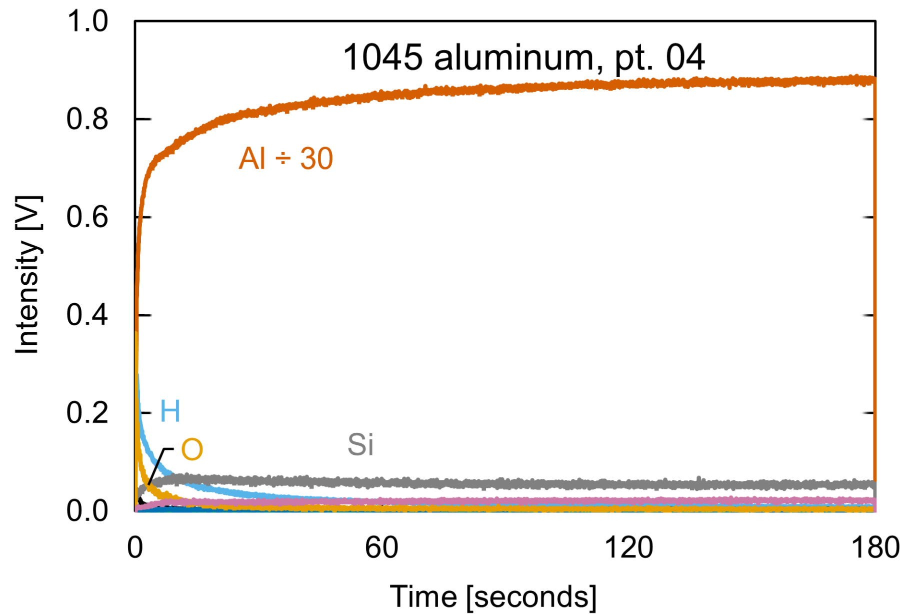

Figure 4.4: GDOES calibration profile of 1045. Relevant elemental signals are labeled in the plot. Power: 25 W. Pressure: 700 Pa.

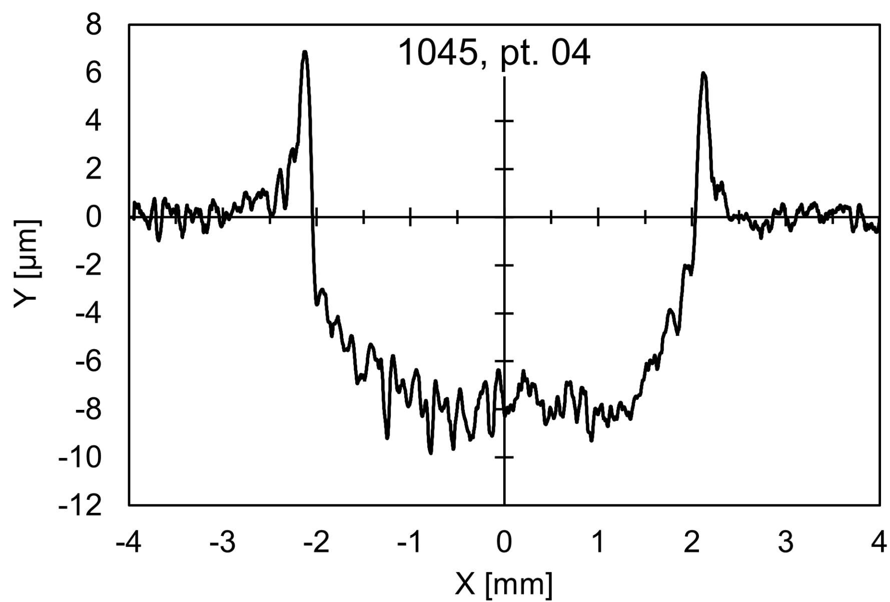

Figure 4.5: Representative stylus profilometer scan of 1045 crater. Power: 25 W. Pressure: 700 Pa. Time: 180 s. Average depth: 6.63 µm.

1766 steel

The GDOES profile for the 1766 steel CRM is plotted in Figure 4.6. This sample is nearly pure iron, with a signal that quickly stabilizes.

A representative crater profile for the 1766 CRM is plotted in Figure 4.7. The crater shape is relatively flat, although preferential sputtering of different grain orientations is apparent.

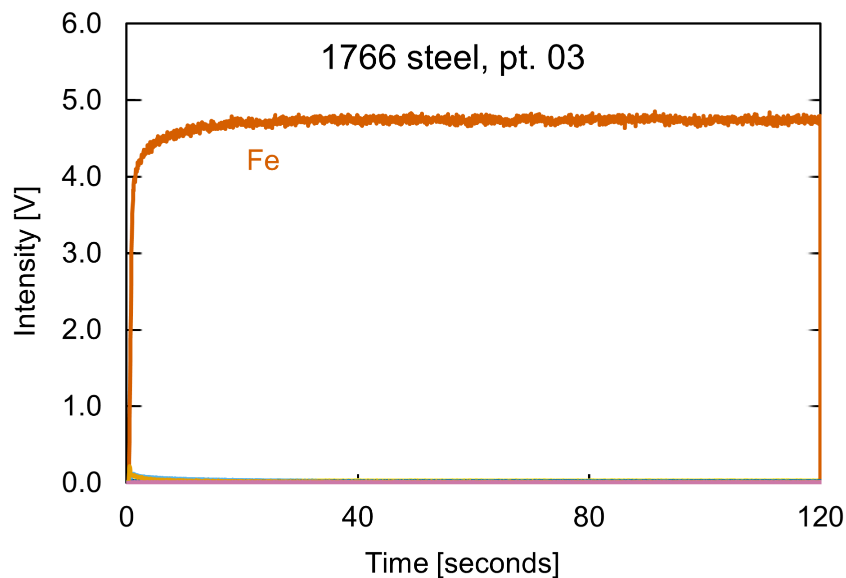

Figure 4.6: GDOES calibration profile of 1766. Relevant elemental signals are labeled in the plot. Power: 25 W. Pressure: 700 Pa.

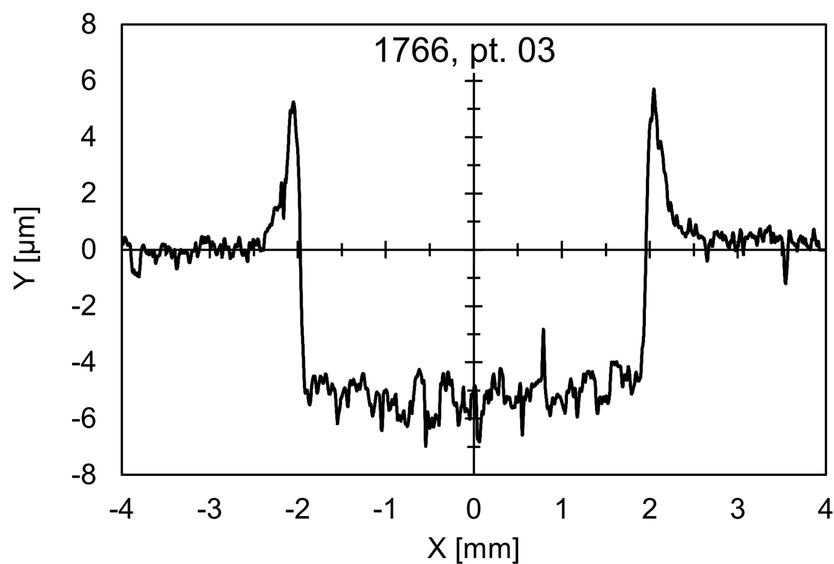

Figure 4.7: Representative stylus profilometer scan of 1766 crater. Power: 25 W. Pressure: 700 Pa. Time: 120 s. Average depth: 4.98 µm.

AlN

The GDOES profile for the AlN calibration sample is plotted in Figure 4.8. The expected elemental signals from aluminum and nitrogen appear acceptable. As a reminder, although the stoichiometric composition of the sample is equal parts aluminum and nitrogen, the associated signals will not necessarily be of equal intensity, for the variety of reasons described in Section 2.2.2.

A representative crater profile for the AlN calibration sample is plotted in Figure 4.9. It is severely concave, likely caused by the insulating nature of the sample. At the high frequency (13.56 MHz) of RF excitation, the capacitance in non-conductive samples increases the impedance, such that the bias at the sputtering surface of the sample can be much less than the voltage applied by the backside electrode [66, 67]. The poor voltage transfer coefficient results in lower incident ion energy, favoring material removal at the edges of the anode [30]

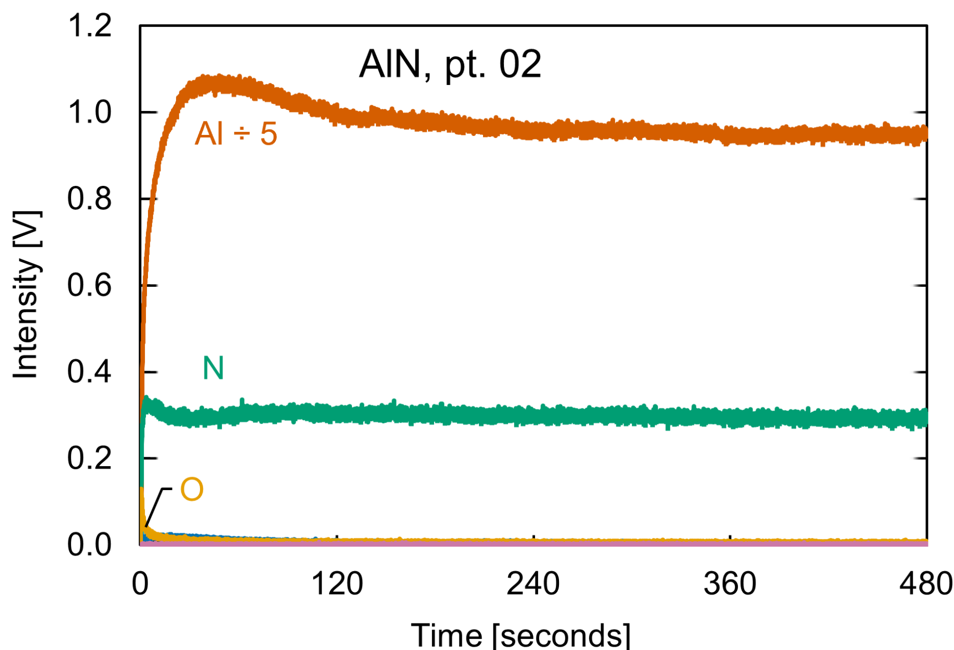

Figure 4.8: GDOES calibration profile of AlN. Relevant elemental signals are labeled in the plot. Power: 25 W. Pressure: 700 Pa.

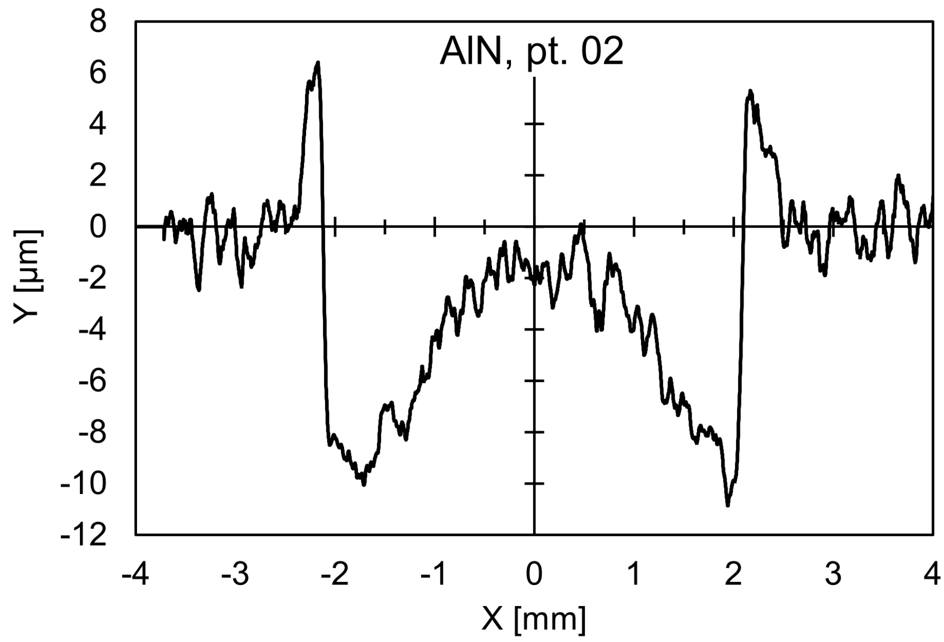

Figure 4.9: Representative stylus profilometer scan of AlN crater. Power: 25 W. Pressure: 700 Pa. Time: 480 s. Average depth: 5.83 µm.

Hastelloy C276

The GDOES profile for the C276 calibration sample is plotted in Figure 4.10; it displays strong signals from the expected metals of the alloy. The instrument also recorded a weak signal from the aluminum emission line (not plotted), which is not a part of the sample's composition. It is most likely spectral interference from one of the other metals.

A representative crater profile for the C276 calibration sample is plotted in Figure 4.11. The crater shape is mostly level, with just slight convexity. The sharp, tooth-like roughness stems from the surface polishing pattern.

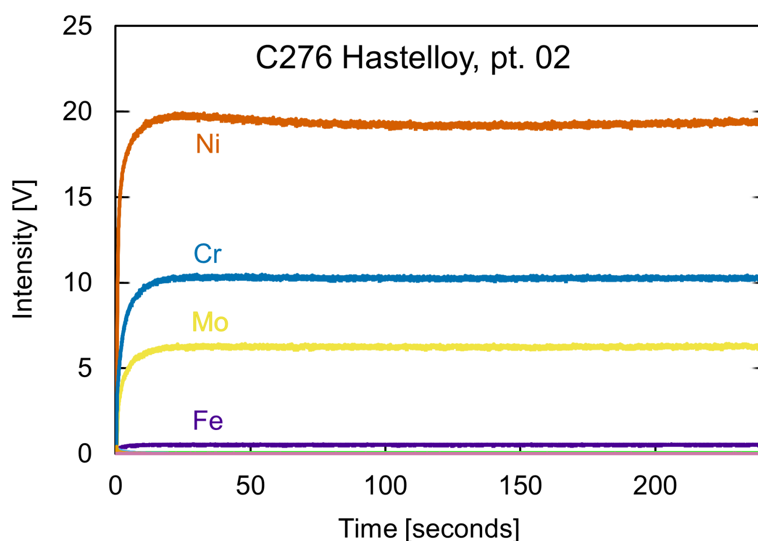

Figure 4.10: GDOES calibration profile of C276. Relevant elemental signals are labeled in the plot. Power: 25 W. Pressure: 700 Pa.

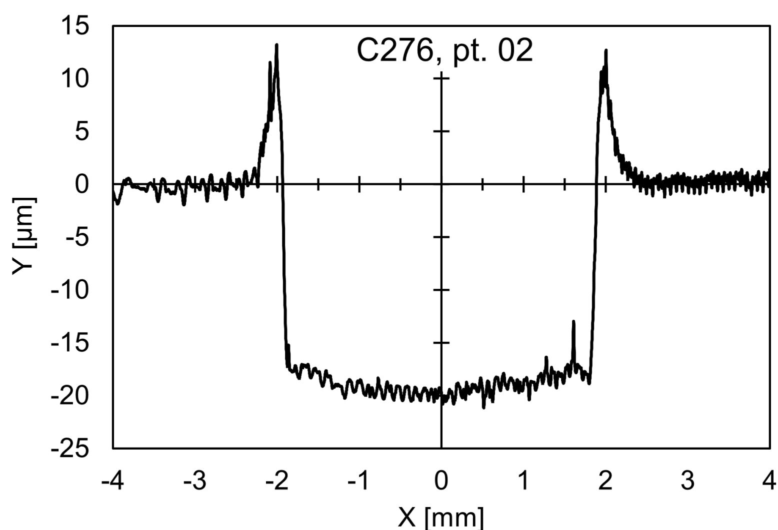

Figure 4.11: Representative stylus profilometer scan of C276 crater. Power: 25 W. Pressure: 700 Pa. Time: 240 s. Average depth: 17.92 µm.

CE650 aluminum-titanium-oxide

The GDOES profile for the CE650 CRM is plotted in Figure 4.12. The elemental profile is stable after 60 seconds, with the expected elements present.

Due to the small size of the sample and the material hardness resisting the efficacy of polishing, measurements on this sample typically overlapped somewhat with previous craters. This made it challenging to obtain clean line scans across the current crater with the stylus profilometer. The 3D optical profiler was more useful for these measurements, as a larger area is mapped and line scans can be taken afterward, avoiding regions influenced by previous craters. A representative optical profiler line scan for a crater on the CE650 calibration sample is plotted in Figure 4.13.

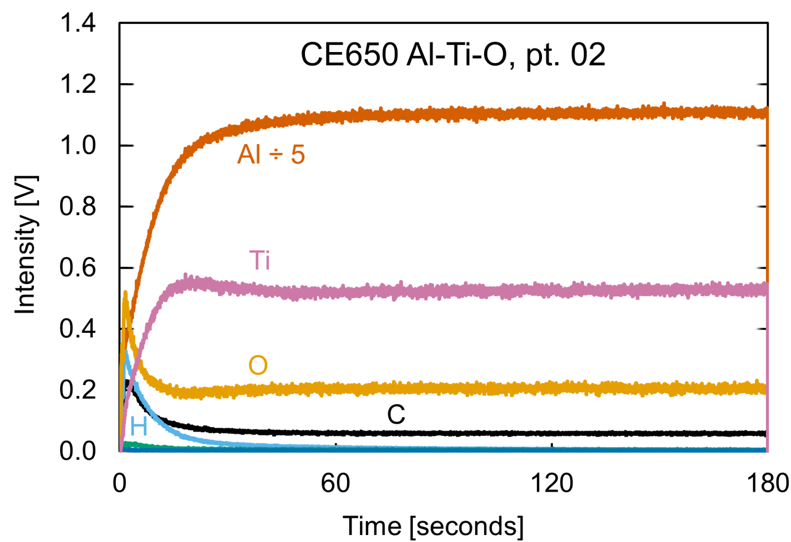

Figure 4.12: GDOES calibration profile of CE650. Relevant elemental signals are labeled in the plot. Power: 25 W. Pressure: 700 Pa.

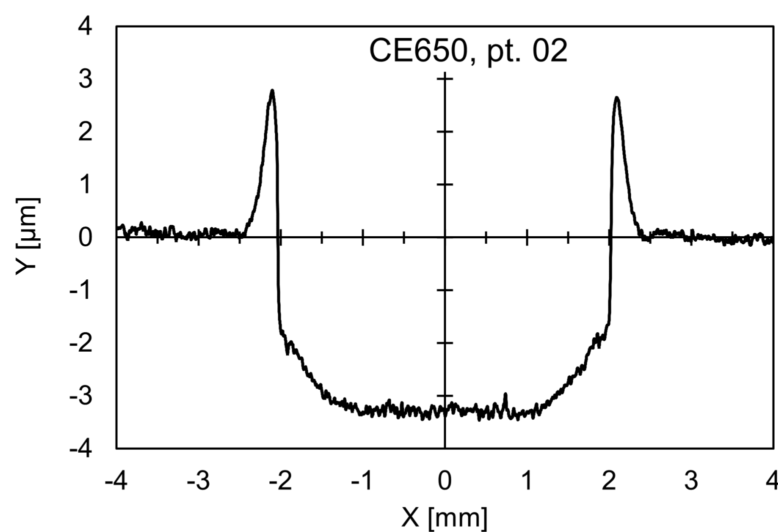

Figure 4.13: Representative 3D optical profiler line scan of CE650 crater. Power: 25 W. Pressure: 700 Pa. Time: 180 s. Average depth: 2.93 µm.

Chromium

The GDOES profile for the chromium calibration sample is plotted in Figure 4.14. It is as expected.

A representative crater profile for the chromium calibration sample is plotted in Figure 4.15. It appears fine, although roughness is evident both inside and outside the crater.

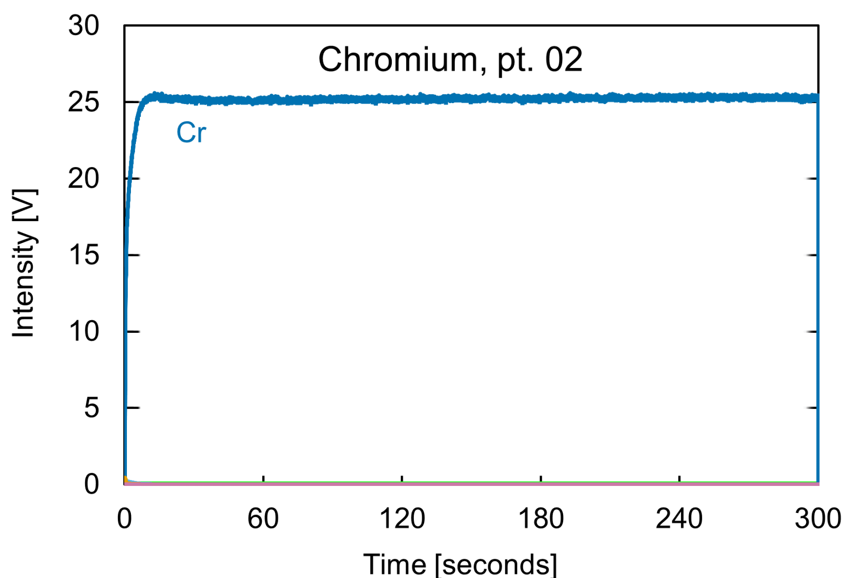

Figure 4.14: GDOES calibration profile of chromium. Relevant elemental signals are labeled in the plot. Power: 25 W. Pressure: 700 Pa.

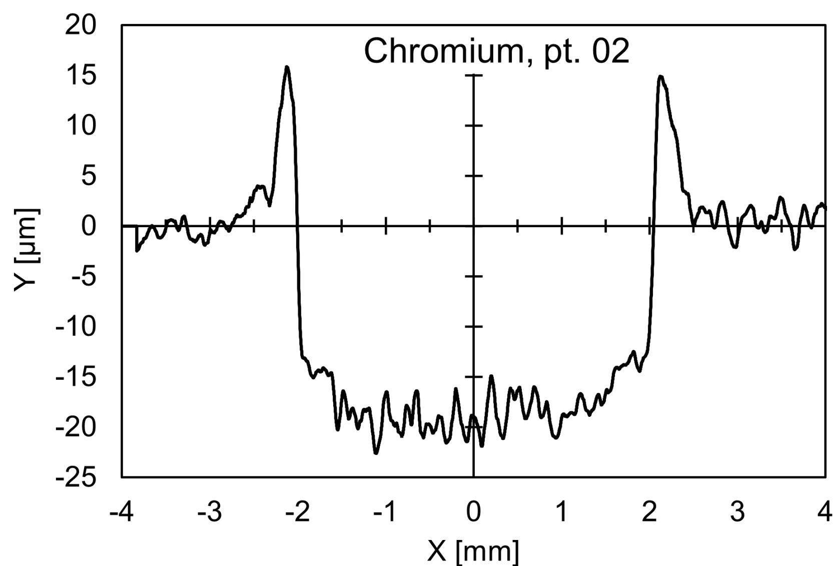

Figure 4.15: Representative stylus profilometer scan of chromium crater. Power: 25 W. Pressure: 700 Pa. Time: 300 s. Average depth: 17.42 µm.

CrN PLD target

The GDOES profile for the CrN PLD target is plotted in Figure 4.16. Previous measurements, however, were prone to issues such as high nitrogen signal or unstable chromium signal. In one previous measurement, the sample actually fractured into pieces, possibly because the PLD target is not solid chromium nitride, but rather a disc of packed powder. The presented measurement at pt. 12 was taken on one of these fragments using a small-sample holder accessory.

A representative crater profile for the CrN PLD target is plotted in Figure 4.17. It is quite convex, and there was a large standard deviation in measured crater depths from different scans. The additional uncertainty regarding the sample density results in a large error range in the relative sputtering rate.

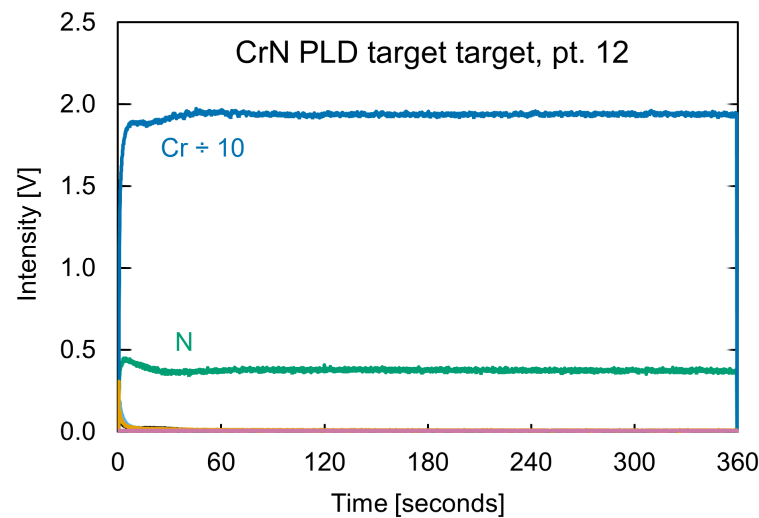

Figure 4.16: GDOES calibration profile of CrN PLD target. Relevant elemental signals are labeled in the plot. Power: 25 W. Pressure: 700 Pa.

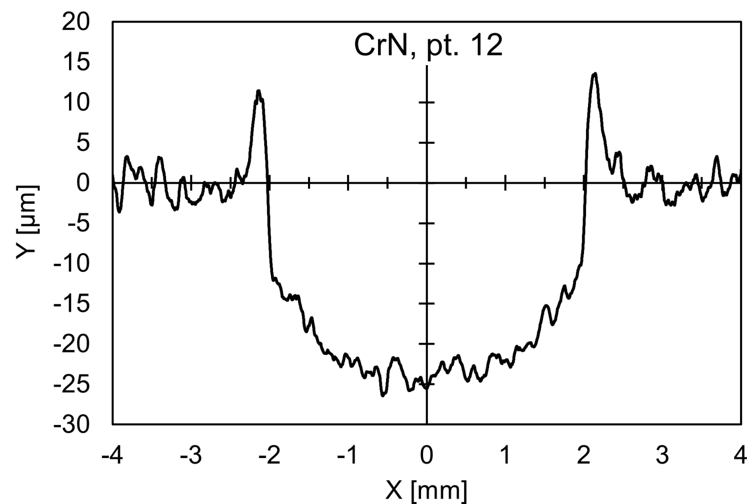

Figure 4.17: Representative stylus profilometer scan of CrN PLD target crater. Power: 25 W. Pressure: 700 Pa. Time: 360 s. Average depth: 18.97 µm.

JK49 high-alloy nitrogen steel

The GDOES profile for the JK49 steel CRM is plotted in Figure 4.18. The various elemental signals have stabilized after about 60 seconds.

A representative optical profile line scan for a crater on the JK49 CRM is plotted in Figure 4.19. The crater profile is nicely shaped, with just slight curvature at the edges.

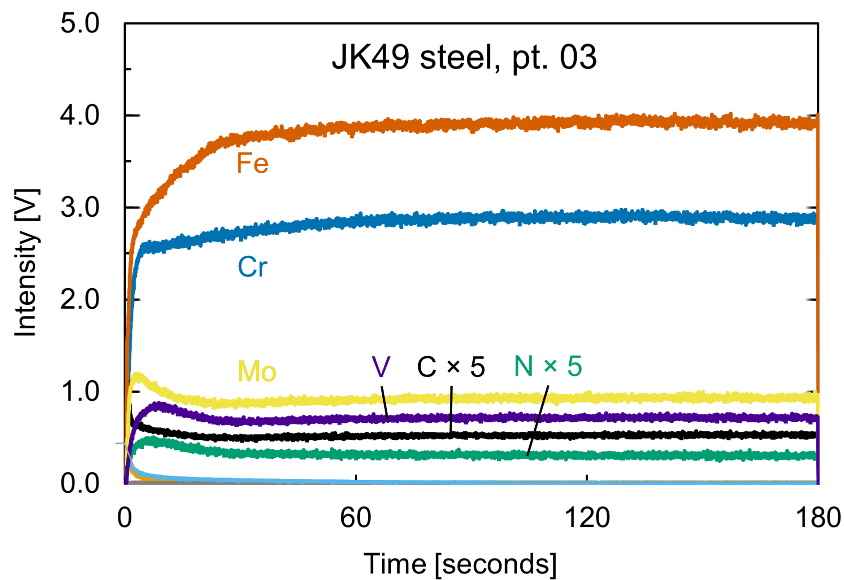

Figure 4.18: GDOES calibration profile of JK49. Relevant elemental signals are labeled in the plot. Power: 25 W. Pressure: 700 Pa.

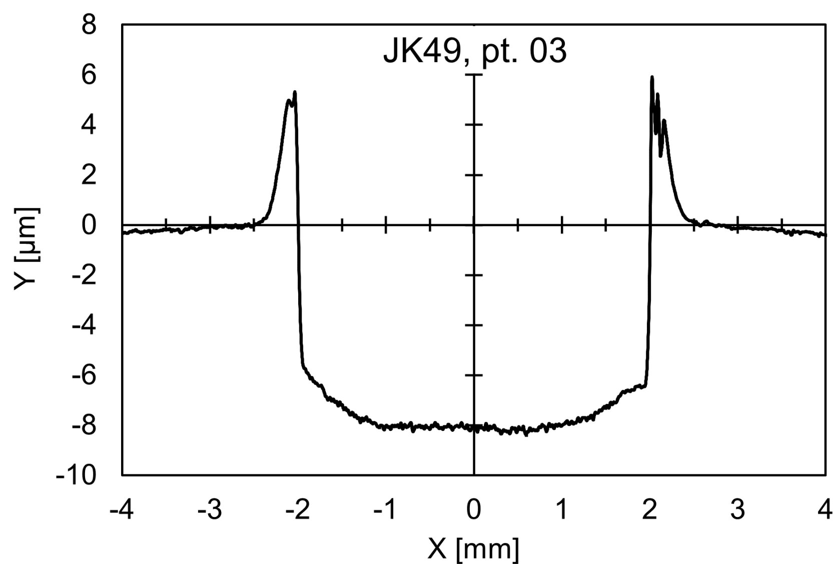

Figure 4.19: Representative 3D optical profiler line scan of JK49 crater. Power: 25 W. Pressure: 700 Pa. Time: 180 s. Average depth: 7.52 µm.

Quartz (SiO_2)

The GDOES profile for the quartz calibration sample is plotted in Figure 4.20. The measured signals on this sample are extremely weak compared with the metal-based samples. This is due to its insulating nature. Due to the unquantified voltage drop across the sample, the realized plasma power may be near the lower limit required to achieve sputtering [62, 55]. A long sputtering time of 10 minutes was necessary in order to erode a deep enough crater to measure.

A representative crater profile for the quartz calibration sample is plotted in Figure 4.21. Similar to the aluminum nitride sample, the quartz crater is quite concave. It is also extremely shallow. The resulting erosion rate, significantly less than all other samples, is in line with the value reported in [68]. Pulsed mode is often recommended for glass samples, as sputtering at normal power levels can cause melting of the surface, which may have occurred here [55, 44].

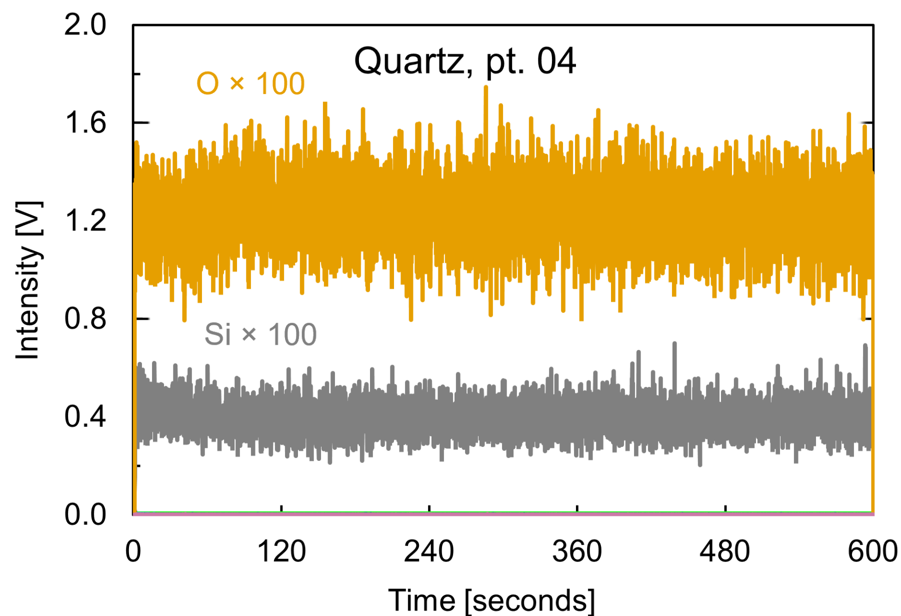

Figure 4.20: GDOES calibration profile of quartz. Relevant elemental signals are labeled in the plot. Power: 25 W. Pressure: 700 Pa.

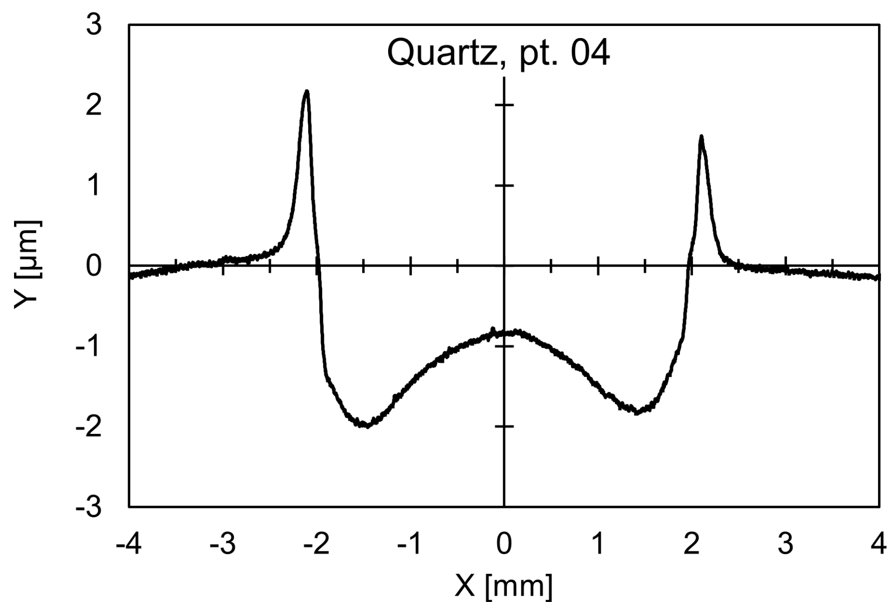

Figure 4.21: Representative stylus profilometer scan of quartz crater. Power: 25 W. Pressure: 700 Pa. Time: 600 s. Average depth: 1.52 µm.

Silicon

The GDOES profile for the silicon calibration sample is plotted in Figure 4.22. It is as expected.

A representative crater profile for the silicon calibration sample is plotted in Figure 4.23. It has rounded edges, and some curvature is evident across the entire wafer surface.

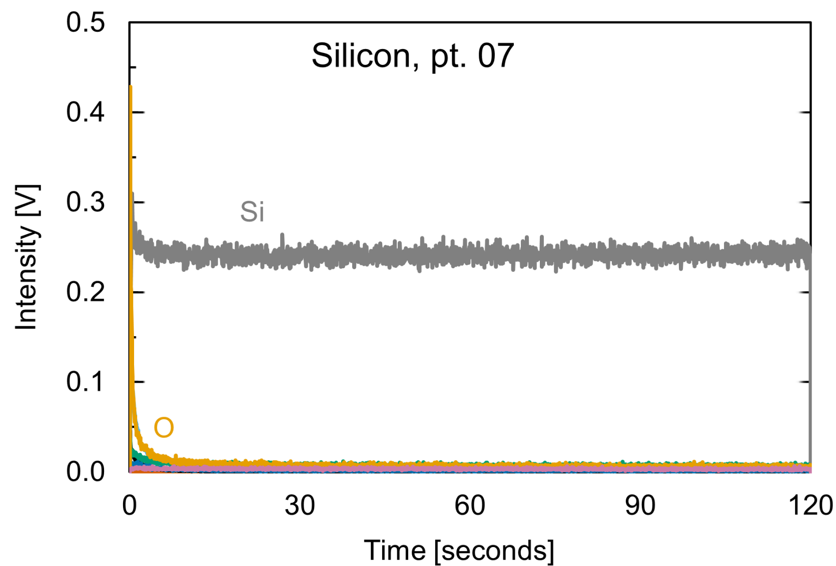

Figure 4.22: GDOES calibration profile of silicon. Relevant elemental signals are labeled in the plot. Power: 25 W. Pressure: 700 Pa.

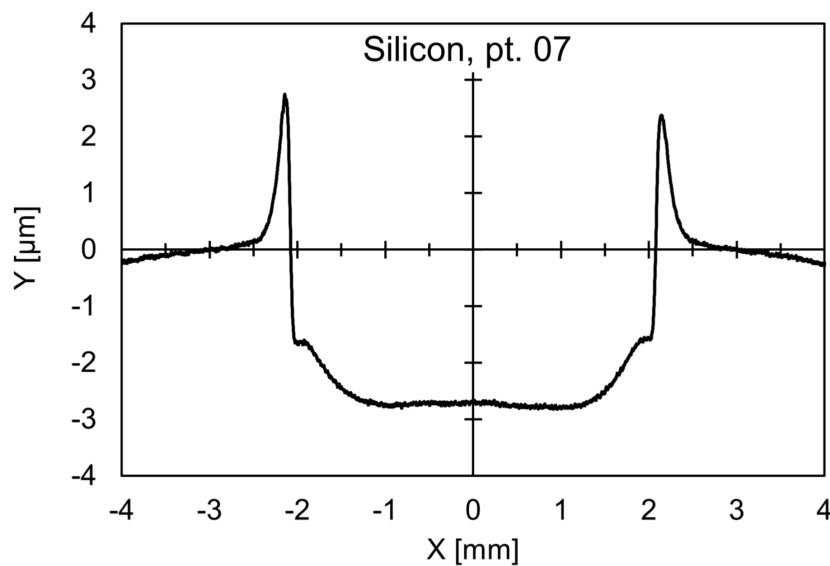

Figure 4.23: Representative stylus profilometer scan of silicon crater. Power: 25 W. Pressure: 700 Pa. Time: 120 s. Average depth: 2.46 µm.

Titanium

The GDOES profile for the titanium calibration sample is plotted in Figure 4.24. The titanium emission intensity is strong and stable, as expected. Not plotted here is a weak, but persistent, tin emission line (Sn 317.510 nm), assumed to be a product of spectral interference from the titanium. This explanation is supported by the appearance of a small tin signal in profiles of the diverse other titanium-based samples.

A representative crater profile for the titanium calibration sample is plotted in Figure 4.25. The sample surface was not polished beforehand, and the existing roughness is evident both inside and outside the crater.

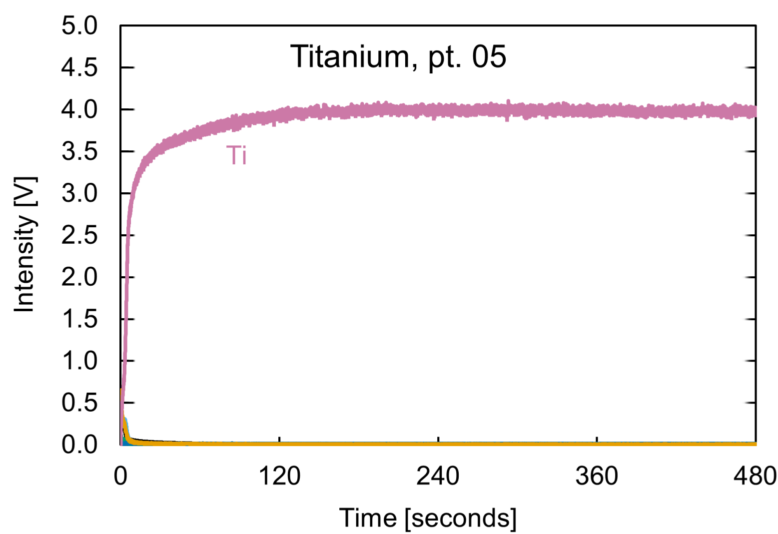

Figure 4.24: GDOES calibration profile of titanium. Relevant elemental signals are labeled in the plot. Power: 25 W. Pressure: 700 Pa.

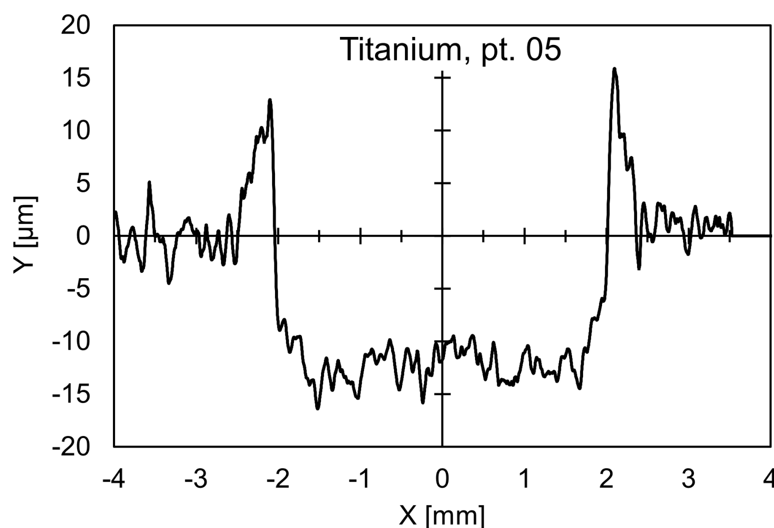

Figure 4.25: Representative stylus profilometer scan of titanium crater. Power: 25 W. Pressure: 700 Pa. Time: 480 s. Average depth: 12.11 µm.

TiN

The GDOES profile for the TiN calibration sample is plotted in Figure 4.26. The tin nitride sample used here is not a bulk material, but a coating on cobalt-chromium. The elemental signals are still slanting slightly even once the bulk substrate is reached (at around 320 seconds, not plotted here). Some chromium diffusion to the surface is noticeable. The Sn 317.510 nm signal appears again in the recorded data, but is omitted from the plot here.

The TiN measurement at pt. 02 is used for calibration, but sputtering proceeded into the substrate in this instance. For the purpose of sputtering rate determination, another measurement was taken (pt. 03) which terminated in the TiN layer. A representative crater profile for the TiN calibration sample at pt. 02 is plotted in Figure 4.27. The sides are rather rounded (convex).

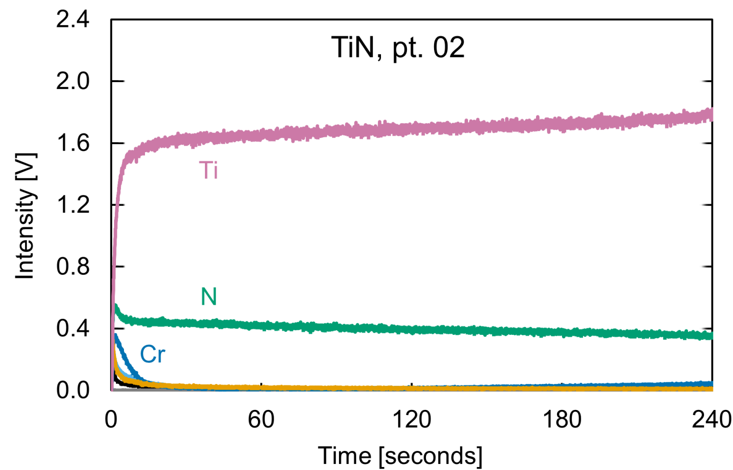

Figure 4.26: GDOES calibration profile of TiN. Relevant elemental signals are labeled in the plot. Power: 25 W. Pressure: 700 Pa.

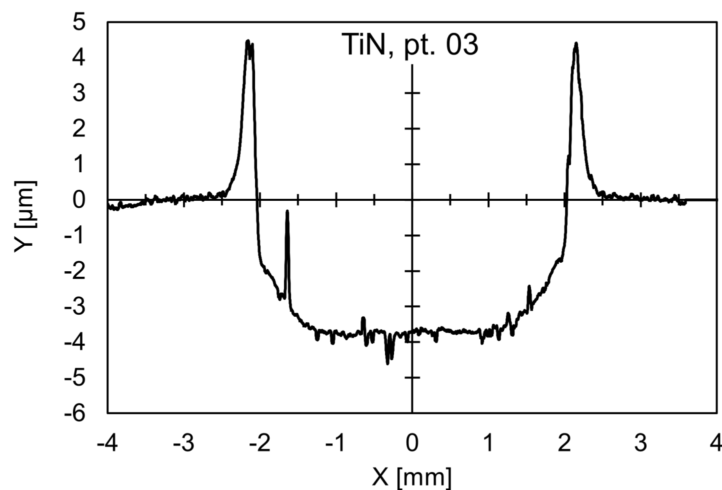

Figure 4.27: Representative stylus profilometer scan of TiN crater. Power: 25 W. Pressure: 700 Pa. Time: 240 s. Average depth: 3.21 µm.

TiO_2 PLD flat film

The GDOES profile for the F-TiO_2-O-700-opt PLD sample is plotted in Figure 4.28 Nominally, this sample is stoichiometric TiO_2 deposited by PLD on a silicon substrate. In reality, some hydrogen and carbon contamination appear in the film. Additionally, the raw data recorded shows oscillations in the titanium signal. This is due to the optical interference effect of a transparent thin film on a reflective substrate, as explained in Section 2.2.4. These oscillations have been smoothed out in the software to better display the actual trend in the elemental signal. The signal from the silicon substrate appears quite sharply at 16 seconds, and the titanium and oxygen lines also drop steeply; this suggests that the plasma parameters are appropriate to form a flat-bottomed crater in this material and resolve a clean interface between the layers. The titanium signal decays for some time into the silicon substrate however, possibly due to diffusion into the heated substrate during deposition. A weak tin emission line was also detected in the TiO_2 layer (but not plotted), caused by spectral interference as in the previous sample.

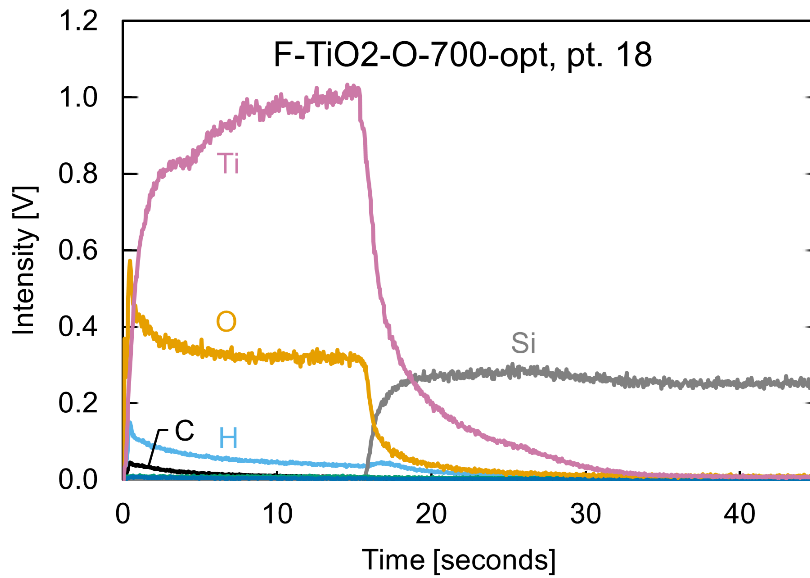

Figure 4.28: GDOES calibration profile of TiO_2 PLD film (F-TiO_2-O-700-opt). Relevant elemental signals are labeled in the plot. Power: 25 W. Pressure: 700 Pa.

The PLD films in the work were all less than 1 µm thick, making it challenging to clearly profile the crater shape using the stylus profilometer. Even using the 3D optical profiler, the substrate typically presented some slight curvature (possibly due to stress of the deposited film) and the films don't have a completely uniform thickness over the 4 mm diameter of measurement, and this tended to obscure the form and depth of the GDOES crater within the layer. So, rather than try to sputter partially into the thin TiO_2 layer and then measure the crater to calculate sputtering rate, an alternative method is to sputter completely into the substrate, note the time required, and rely on a film thickness determination from another source - ellipsometry, in this

case. Prior ellipsometry measurements performed by Brakstad on this sample found a film thickness ranging from 193 nm at the center to 206 nm at the edge. At the particular GDOES spot measured here (marked in Figure 4.29 (a) below), the average thickness is 201 nm.

Since multiple crater depth scans are not available to take a standard deviation, an alternative method is required to estimate sputtering rate uncertainty. One possibility would be to measure at other positions on the wafer and calculate additional sputtering rates according to the times required to sputter through the layer. This option was avoided to save space on the wafer for other tests. According to the ellipsometry thickness map, the minimum and maximum values covered by the crater area are 198.3 and 203.7 nm, a relative error span of 2.7% around the average value. This value is perhaps unrealistically small compared to the relative standard deviations calculated for the other samples, especially given the non-certified nature of the TiO_2 sample. Lacking a more suitable estimate, the software default of 5% will be used [45].

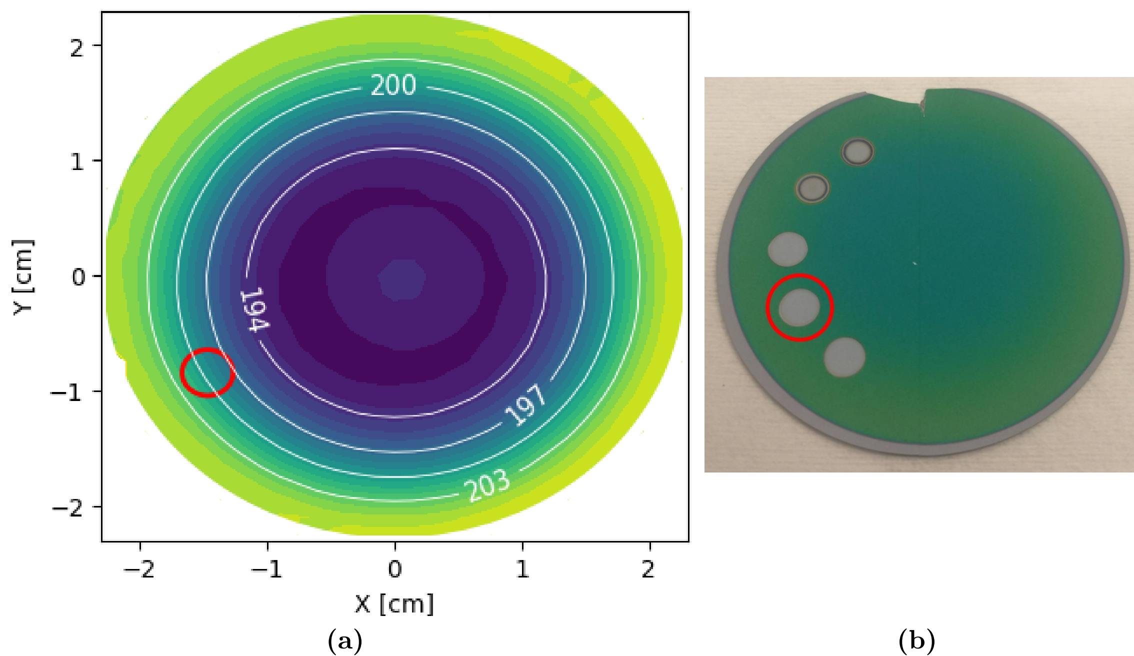

(a) (b)

Figure 4.29: (a) A film thickness color map based on ellipsometry measurements and model for F-TiO_2-O-700-opt. (b) A photograph of the sample with multiple erosion craters from measurements. The red-circled crater is the position used for calibration.

4.2.2 Calibration measurement summary tables

Based on the GDOES measurements presented in the previous section, average signal intensities for titanium, oxygen, chromium, nitrogen, and silicon are calculated for each calibration sample. The results are summarized in Table 4.1 below.

Based on the crater profiles presented in the previous section, average crater depths are calculated for each calibration sample. This is converted to relative sputtering rate. The relative standard deviation of measurements per crater is also calculated. The results are summarized in Table 4.2 below.

Table 4.1: A summary of the relevant measured elemental signal intensities in each of the samples used for calibration. The time range is the period of the measurement used to average signals for the calibration curve. This is typically the final 30-120 seconds of the measurement, once all signals have stabilized. The next columns list the average intensity measured in the selected time range for Ti, O, Cr, N and/or Si, as is relevant for the particular sample.

Sample	**Time range**	**Average intensity [V]**				
	[s]	**Ti**	**O**	**Cr**	**N**	**Si**
1045	150-180	0.022	-	-	-	0.0539
1766	NA	-	-	-	-	-
AlN	360-480	-	-	-	0.2940	-
C276	180-240	-	-	10.28	-	0.0023
CE650	120-180	0.528	0.206	-	0.0052	-
Cr	180-300	-	-	25.31	-	-
CrN	240-360	-	-	19.41	0.3739	-
JK49	120-180	-	-	2.89	0.0611	0.0052
Quartz	300-600	-	0.012	-	-	0.0039
Si	60-120	-	-	-	-	0.2420
Ti	300-480	3.986	-	-	-	-
TiN	210-240	1.764	-	-	0.3611	-
TiO_2	2.8-15.3	0.942	0.327	-	-	-

Table 4.2: A summary of the crater depths, sputtering rates, and uncertainty determined in each of the samples used for calibration. The crater depth is averaged from multiple profilometer scans. Based on the duration of the measurement (sputter time), the erosion rate is calculated. The sputter rate is the product of erosion rate and density. The relative sputtering rate (RSR) is the given sample's SR divided by that of the reference sample, 1766 steel. The relative standard deviation (RSD) is the SD of multiple depth measurements normalized by the average crater depth.

Sample	**Crater depth [µm]**	**Sputter time [second]**	**Erosion rate [nm/s]**	**Density [g/cm³]**	**Sputter rate [g/m²/s]**	**RSR**	**RSD [%]**
1045	6.63	180	36.8	2.685	0.099	0.297	9.1
1766	4.98	120	41.5	7.863	0.326	1.000	5.2
AlN	5.83	480	12.2	3.26	0.040	0.119	13.9
C276	17.92	240	74.7	8.89	0.664	1.994	5.8
CE650	2.93	180	16.3	3.719	0.051	0.152	4.1
Cr	17.42	300	58.1	7.15	0.415	1.247	8.0
CrN	18.97	360	52.7	5.16 $^{\alpha}$	0.272	0.817	7.0$^{\beta}$
JK49	7.52	180	41.8	7.544	0.315	0.946	5.2
Quartz	1.52	600	2.5	2.65	0.007	0.020	6.1
Si	2.46	120	20.5	2.328	0.048	0.143	3.1
Ti	12.11	480	25.2	4.5	0.113	0.341	6.8
TiN	3.21	240	13.4	5.3	0.072	0.217	9.4
TiO_2	0.20$^{\gamma}$	16.3	12.4	3.78	0.047	0.141	5.0

$^{\alpha}$ Assumes a nominal density of 5.9 g/cm^3. Based on the modified density range of 85-90%, the density is set at $5.9 * 87.5\% = 5.16$, with a relative uncertainty of 3%.

$^{\beta}$ The RSD based on multiple scans is 6.4%. The value of 7.0% in the table accounts for an additional 3% density uncertainty, treated as a multiplicative error source.

$^{\gamma}$ As opposed to basing the sputtering rate on crater depth, the entire film depth is used, based on ellipsometry characterization.

4.2.3 Reduced sputtering measurements

Throughout the calibration process, one of the concerns was that the small number of reference samples available for each element might be insufficient to form a reliable calibration curve. Of course, a line can be defined from just two points, and one of those points could be the origin, but it is recommended to use at least six CRMs for a linear curve, and more if the curve appears non-linear [23].

Since additional reference samples were not immediately available, this motivated the question of if each sample could be used to generate multiple data points for a calibration curve. In the typical multi-matrix calibration performed for compositional depth profiling, each different sample measurement will involve a change in all three of I_i, c_i, and q_M. For a single sample, though, a means of adjusting q_M would cause a shift in I_i, despite c_i remaining the same. Several studies have noted a dependence of sputtering rate q_M on sample thickness [55, 69, 30], mostly related to a voltage drop from the sample's rear to the sputtering sample.

As an experimental means of artificially adjusting sample thickness, a silicon wafer was inserted behind the rear of the JK49 steel disk, held in place between the sample and the cathode block. Using the same measurement conditions as before (i.e. Figure 4.18), this new GDOES measurement recorded a reduction in the major signal intensities to approximately 96% of their original values. This experiment was repeated with the silicon wafer buffer replaced by a quartz slide - thicker and more insulating. In this instance, the signal intensities reduced to 84% of original.

As the method to reduce the sputtering rate seemed to work as intended, it was repeated with some of the other available calibration samples. As an example, Figure 4.30 compares the C276 GDOES profile as normal (left) and with the quartz slide inserted (right). The inclusion of the insulating quartz sample causes the signal intensities to reduce to approximately 85%.

A comparison of stylus profilometer crater scans for both C276 pt. 02 and pt. 03 is shown in Figure 4.31. In the course of an identical GDOES measurement duration, pt. 03 (the quartz-buffered measurement) was sputtered to an average depth of 14.39 µm, which is 80% of pt. 02's depth of 17.92 µm. This effective thickening of the sample has the intended effect of decreasing both sputtering rate and intensity (while leaving elemental concentration unchanged, of course).

This method was used for an additional measurement on C276, CE650[1], JK49, silicon, titanium, and the TiO_2 PLD flat film. The results for these measurements appear qualitatively similar to their normal counterparts (the measurements of Section 4.2.1), so rather than plot all GDOES and crater profiles, Table 4.3 merely summarizes the signal intensity and sputtering rate ratios compared to the normal calibration measurement. The measurements are termed "reduced", and an asterisk *

[1] The reduced measurement on CE650 used a silicon wafer as the buffer, as the plasma failed to ignite when using the quartz slide

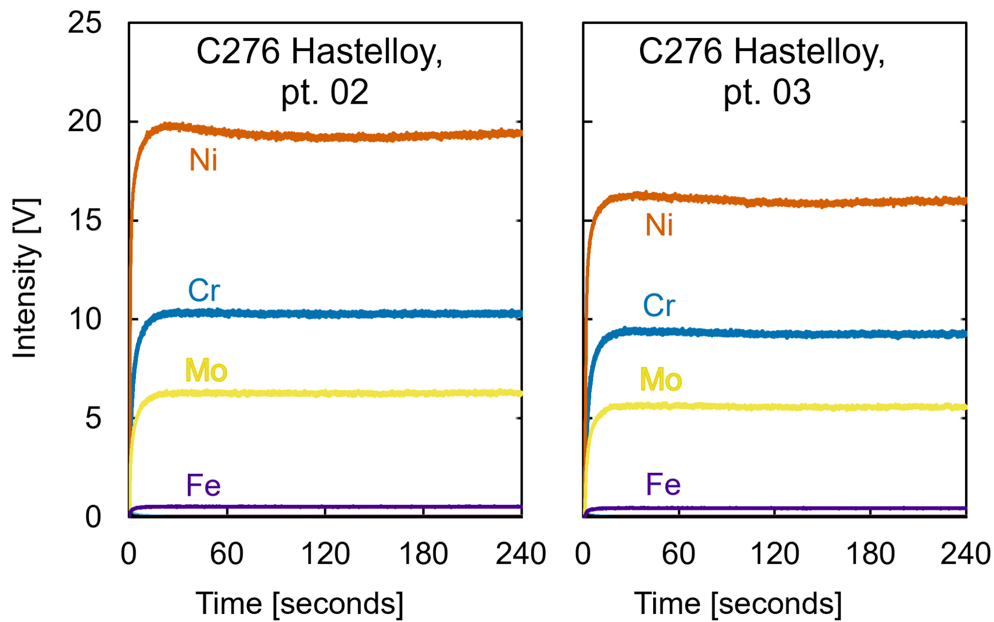

Figure 4.30: A comparison of two GDOES profiles of the same sample C276. Power: 25 W. Pressure: 700 Pa. The measurement at pt. 03 differs from pt. 02 by the inclusion of a quartz slide at the backside of the sample. The signal intensities drop by 15%, due to the reduced effective plasma power.

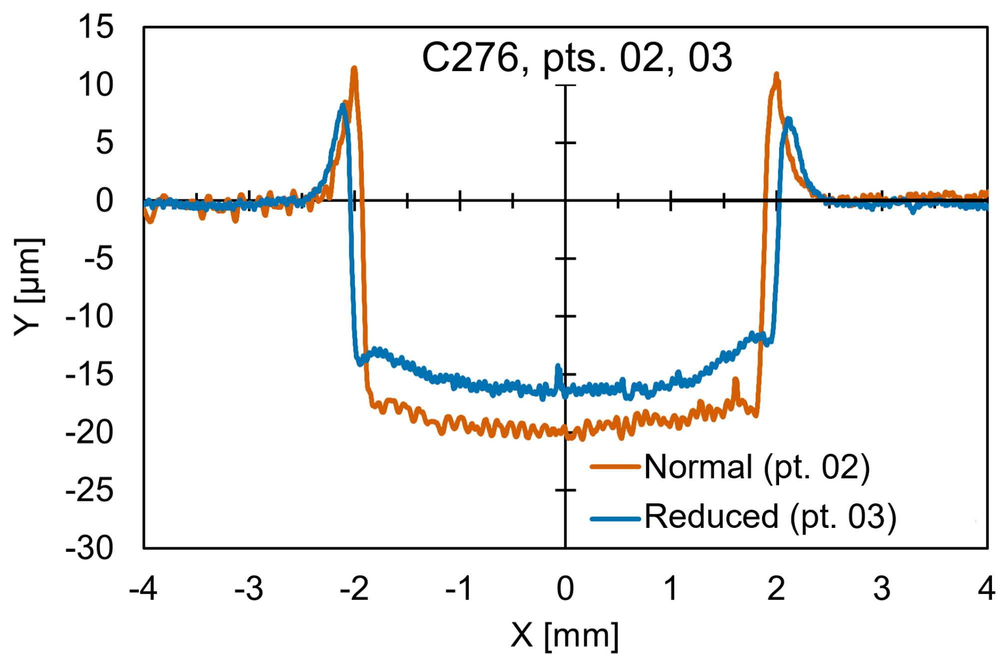

Figure 4.31: Representative stylus profilometer scans of C276 pt. 02 (the same as in Figure 4.11), and pt. 03 where the sputtering rate has been artificially slowed by inserting a quartz slide between the sample backside and the electrode. For both measurements: Power (nominal applied) = 25 W. Pressure = 700 Pa. Time = 240 s. Average depth pt. 02: 17.92 µm. Average depth pt. 03: 14.39 µm.

appears after the sample name to distinguish the measurement from its normal counterpart. These reduced calibration measurements will also appear in the calibration curves in the following section, for a visual comparison. As in the normal calibration measurements, the sputtering rate was determined by averaging the crater depth from multiple stylus profilometer scans. In the case of the TiO_2 PLD sample, it was estimated again according to the film thickness (201 nm, by ellipsometry) and time required to sputter through to the substrate (22.0 s in this case).

Table 4.3: The ratio of selected signal intensities between reduced measurements and normal measurements on the same sample. The reduced versions (identified by an *) involved a quartz slide inserted at the backside of the sample, effectively increasing sample thickness and resistance. SR is sputtering rate.

Sample	Intensity ratio [%]					SR ratio
	Ti	O	Cr	N	Si	[%]
C276*	-	-	90.0	-	-	80.3
CE650*	89.3	83.9		85.8	-	92.7
JK49*	-	-	82.2	84.0	75.8	85.7
Si*	-	-	-	-	70.9	71.0
Ti*	96.9	-	-	-	-	87.5
TiO_2*	79.8	56.6	-	-	-	73.9

The decision to reduce sputtering rate by this artificial sample thickening was based on the supposition that it more closely resembled the differences already inherent in different calibration samples (such as dimension and conductivity). A direct change to the applied power seemed like too blatant of a change to the plasma conditions, invalidating the assumptions that make multi-matrix calibration possible.

Subsequent consideration reveals that this choice may have been misguided. As explained in Section 2.3.2, the emission yield is the key to relating detected intensity to elemental concentration in the plasma, and the emission yield depends on conditions in the plasma. Emission yield increases with excitation current and decreases with excitation voltage [23, 33]. The modeled dependencies in each case are not quite proportional [42], but the inverse relationships with current and voltage can balance each other enough to minimize the change to emission yield when both parameters are scaled together. Indeed, Ref. [42] actually develops a calibration curve from just three samples, using each sample to produce multiple data points by explicitly adjusting the power up and down. Such an approach was not found repeated in any other literature reviewed for this thesis, but a Horiba researcher mentioned in passing that it was a valid possibility [70].

In contrast, the backside insertion of the quartz sample may be influencing emis-

sion yield in an unacceptable manor. Recall that the plasma impedance has an influence on emission yield when the ratio of voltage and current changes.

The mechanism by which the quartz insertion causes a reduction in intensity and sputtering rate is complex. The inclusion of an insulating layer no doubt causes some voltage drop such that bias apparent at the sputtering surface is less than the applied voltage [67, 66], decreasing the effective plasma power. This much is evident from the decreased sputtering rates. At a first approximation, the applied current is unchanged, because the applied voltage is unchanged. Decreasing the effective voltage while maintaining current would decrease the plasma impedance, increasing emission yield. However, the resulting mismatch between source impedance and plasma impedance would increase the reflected power, causing a feedback loop in the matching box to seek equilibrium. The final operating point achieved by these interactions is not so clear. Although the instrument can output a measurement of applied voltage, the reported value is only valid for conductive samples [24], which no longer applies due to the quartz layer. Similarly, it is difficult to determine the current in RF operation mode [66, 42].

Lacking confidence in the validity of this reduced method, these data points will *not* ultimately be used in the calculation of calibration curves (unless otherwise noted). They are, nevertheless, included in the plots in the following section, as they generally lie consistent with the curve and this may prove useful in future work. Considering the difficulty of obtaining appropriate oxygen- and nitrogen-containing CRMs, further study of this topic is recommended to maximize the utility of each calibration sample.

4.3 Calibration curves

Based on the emission line intensities (Table 4.1) and relative sputtering rates (Table 4.2) from all calibration sample measurements, the Quantum software was used to develop calibration curves for titanium, oxygen, chromium, nitrogen, and silicon. These are shown in Figures 4.32-4.38.

Each measurement data point is plotted as intensity (I_i) vs elemental concentration multiplied by relative sputtering rate ($c_i\ q_{RSR}$). The error bars account for uncertainty in sputtering rate, composition, and variation in intensity (transformed onto the horizontal axis), as explained in Section 3.2.4. The primary contribution to these error bars stems from the differences in crater depth from repeated profilometer scans. While the relative error may be similar amongst the various calibration samples, the absolute error will be lower for small concentration or small sputtering rate. For many of these low-concentration points, the error bars are not even visible on the plot. Two calibration curves are calculated for each element: one weighted and one unweighted, favoring lower concentrations and higher concentrations, respectively [23]. As mentioned in the previous section, the data points from measurements with reduced sputtering rates are also plotted (labeled with a *), but were not used for calculation unless otherwise noted.

A zero-concentration data point was included for the calculation of each line. This was provided by the silicon measurement (see Figure 4.22) for the Ti, O, Cr, and N curves. The titanium measurement (see Figure 4.24) was used for the Si curve. This acknowledges that even though there is 0% titanium in the silicon bulk, the titanium emission detector might still record some small non-zero signal due to background or spectral interference. The zero-concentration point additionally encourages the curve to pass through the origin. This data point is not plotted on the figures below.

The calibration curve figures also have a highlighted range of $c_i\ q_{RSR}$ marking the concentration expected (desired) in the (Cr+N) co-doped TiO_2 CCS films (assuming a relative sputtering rate q_{RSR} similar to F-TiO_2-O-700-opt).

The quality of each curve is assessed qualitatively. Metrics such as correlation coefficient R^2 are calculated in the software, but are not so appropriate for the multi-matrix calibration performed for CDP [70].

Titanium

The titanium calibration curve (shown in Figure 4.32) is formed by measurements on pure titanium, titanium nitride, the TiO_2 PLD film, and CE650 (as well as 1045, effectively acting as another zero-concentration point). The unweighted curve fits all data points very well. The slope of the weighted curve is skewed upward by the comparatively small error in the CE650 calibration sample. The expected concentration for the CCS samples is just below that of stoichiometric TiO_2, as some sites will be substituted by the Cr or N dopants.

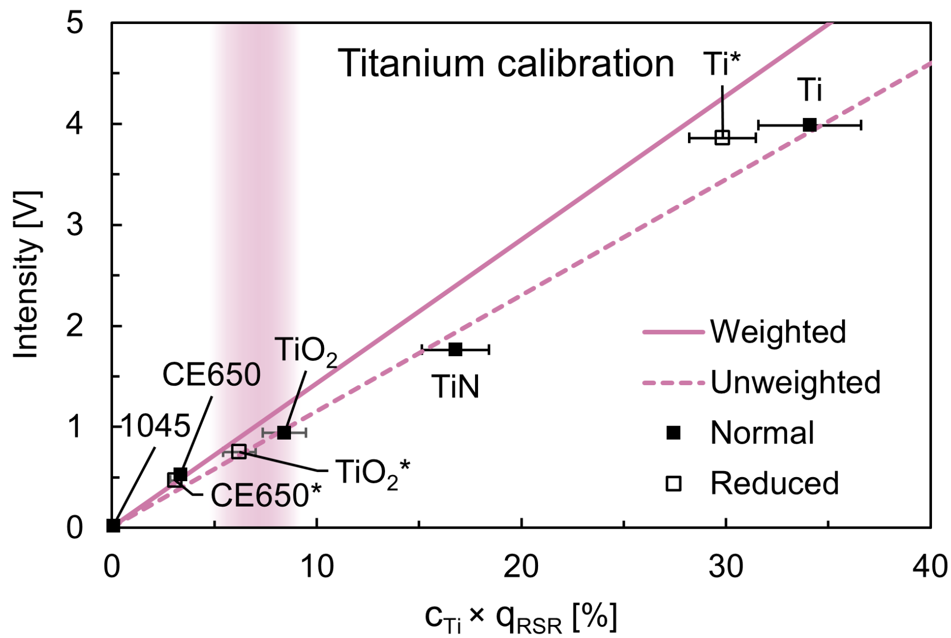

Figure 4.32: Calibration curves formed from the I_i vs $c_i\ q_{RSR}$ data points from titanium-containing reference samples. Both a weighted and unweighted regression line are plotted. Reduced measurements (as explained in Section 4.2.3) are plotted alongside, but were not used in the regression line calculation. A shaded range of $c_i\ q_{RSR}$ marks the desired concentration in the CCS films.

Oxygen

The oxygen calibration curve (shown in Figure 4.33) is formed by measurements on TiO_2, CE650, and quartz. The three samples do not form a clear line. The weighted curve passes through the origin, due to the negligible error of the silicon zero-concentration point. The unweighted curve is pulled by the quartz to cross the x-axis at a positive value. This is problematic, as a detector reading of 0 V intensity will be interpreted as a non-zero concentration of oxygen in the sample. As was noted in the quartz calibration (accompanying Figure 4.20), the signals were extremely weak. The sample might be so insulating that the plasma conditions and emission yield are incomparable to the other samples.

Ignoring the quartz data point is of little help, as the TiO_2 and CE650 points also fail to generate a linear curve to the origin. Either the TiO_2 intensity is too high, or the CE650 intensity is too low, or the TiO_2 sputtering rate is too low, or the CE650 sputtering rate is too high. Both the TiO_2 and CE650 data points fall well on the titanium curve in Figure 4.32, suggesting that the sputtering rates are reasonable.

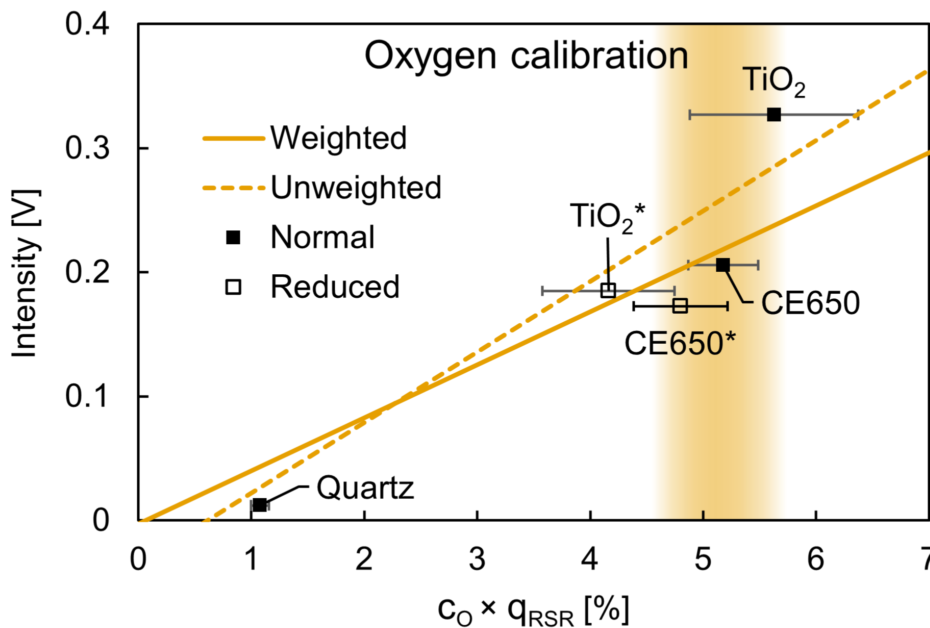

Figure 4.33: Calibration curves formed from the I_i vs c_i q_{RSR} data points from oxygen-containing reference samples. Both a weighted and unweighted regression line are plotted. Reduced measurements (as explained in Section 4.2.3) are plotted alongside, but were not used in the regression line calculation. A shaded range of c_i q_{RSR} marks the desired concentration in the CCS films.

There was a noticeable hydrogen signal throughout the TiO_2 film in Figure 4.28. One of the reported influences of the hydrogen effect is an enhancement of the O 131.223 nm line [23, 43]. Applying a negative correction to the oxygen calibration signals could be used to bring the TiO_2 and CE650 data points in line. This is a manual process, where a correction factor in the software must be adjusted until the

results are satisfactory. The outcome is plotted in Figure 4.34, where the quartz sample has been omitted from the regression calculation. The TiO_2 data point has significantly decreased in intensity, and the curve slope has decreased slightly compared to the weighted curve in Figure 4.33. The curve intersects the positive Y-axis because the silicon zero-concentration point recorded a non-zero oxygen signal.

There is a danger, of course, in this type of correction, especially applied to so few points. Although the hydrogen effect on oxygen signals is a valid physical phenomenon, there is little guidance on what a reasonable correction factor may be. This hydrogen-corrected calibration curve will be used going forward, but this caveat should be kept in mind when interpreting quantified results.

As with titanium, the expected oxygen content in the CCS films is just below that of stoichiometric TiO_2.

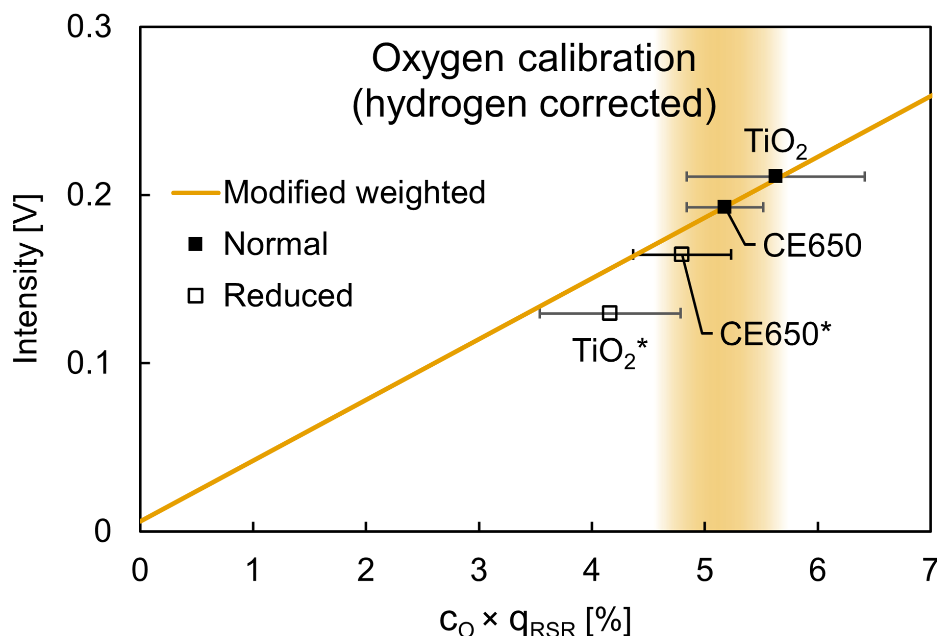

Figure 4.34: A re-plotting of the data points in Figure 4.33 after application of a negative hydrogen correction factor to the O 131.223 nm signal intensities. Only a weighted curve is presented. The reduced measurements are plotted alongside, but were not used in the regression line calculation. The quartz sample was also omitted in this instance.

This raises the question of if the hydrogen effect has also altered the titanium signal in the calibration sample F-TiO_2-O-700-opt. It is reported that hydrogen can decrease the intensity of the Ti 365.355 nm line [43, 38]. The TiO_2 data point in Figure 4.32 already lies precisely on the unweighted curve, though, and application of a positive correction factor merely shifts the point out of line. This is perhaps another reason to be skeptical of the correction applied to the oxygen curve. Further research should consider the relative effects of hydrogen on these titanium and oxygen emission lines.

Chromium

The chromium calibration curve (shown Figure 4.35) is formed by measurements on pure chromium, the CrN PLD target, C276, and JK49. The Cr 425.439 nm emission line is classified as a resonant line and is known to suffer from self-absorption. For this reason, a 2nd-order curve has been applied, with a very good fit to the data [23]. The weighted and unweighted curves differ only slightly. The weighted curve crosses closer to the origin, so this will be preferred. The reduced measurements of JK49* and C276*, although not used for regression calculation, happen to fit quite well on the curve.

As mentioned in Section 3.1.2, some results were additionally calculated as if the CrN PLD target were actually Cr_2N. This would have no impact on the measured intensity, but the increased concentration of chromium shifts the point right on the x-axis. The higher density of Cr_2N compared to CrN also means that the measured crater depth would correspond to a higher sputtering rate.

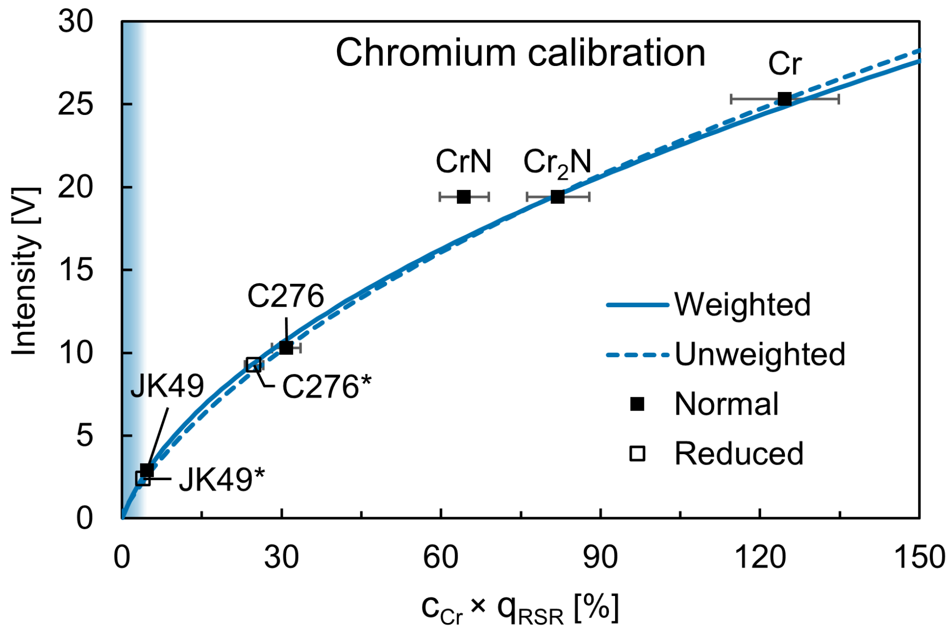

Figure 4.35: Calibration curves formed from the I_i vs c_i q_{RSR} data points from chromium-containing reference samples. Both a weighted and unweighted regression line are plotted. A 2nd-order curve is used to account for self-absorption effects. Reduced measurements (as explained in Section 4.2.3) are plotted alongside, but were not used in the regression line calculation. A shaded range (far left) of c_i q_{RSR} marks the desired concentration in the CCS films.

Both of the regression curves plotted in Figure 4.35 are calculated without either the CrN or Cr_2N data points (that is, only the Cr, C276, JK49, and silicon zero-concentration points were used). The Cr_2N clearly fits better with the regression line. When the curve is calculated with the inclusion of CrN (not shown), it overshoots the C276 and Cr points. When the curve is calculated with the inclusion of Cr_2N

(not shown), it remains nearly indistinguishable from the one in Figure 4.35.

The expected concentration of chromium in the CCS samples is up to 10 at%. After factoring by the relative sputtering rate of TiO_2, this lies at the far left range of the concentrations sampled, below even JK49. Despite the apparently good fit of the overall curve, more reference samples should be included in this very low-concentration range.

Nitrogen

The nitrogen calibration curve (shown Figure 4.36) is formed by measurements on the CrN PLD target, TiN, AlN, JK49 and CE650. Once, again, a Cr_2N version of the PLD target is included. Although Cr_2N has a larger sputtering rate than CrN, the decreased nitrogen content in the former results in a leftward shift on the x-axis.

The data points are disparate. There is no clear best choice for a regression curve. Two separate curves are plotted, based on a different selection of the data points. The first, "Weighted, partial", forms a line from the origin through the AlN and TiN points. The JK49 and reduced JK49* points also form a line to the origin which happens to cross the Cr_2N point as well. The unweighted version of this curve fits slightly better than the weighted, so it is labeled "Unweighted, partial".

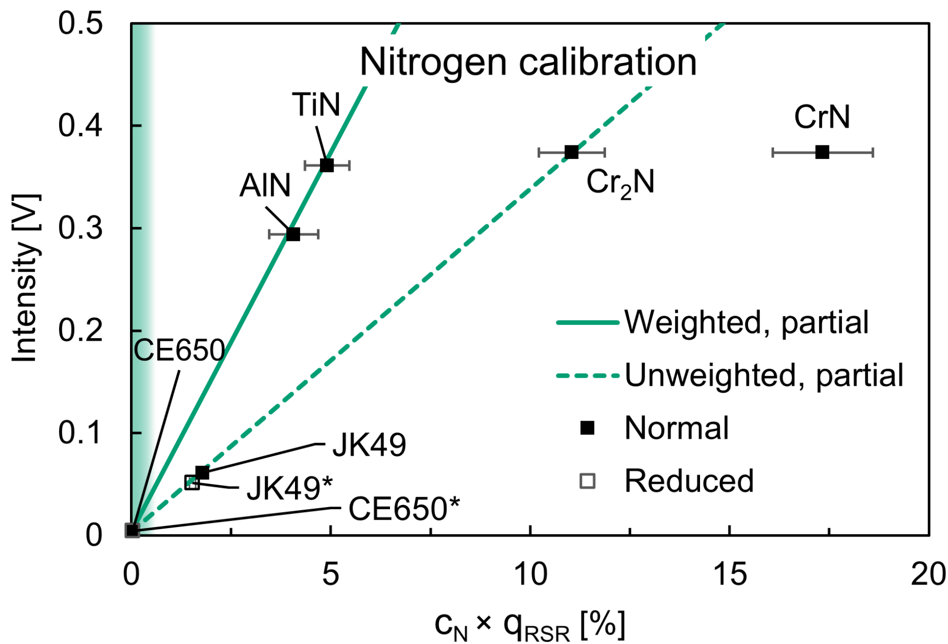

Figure 4.36: Calibration curves formed from the I_i vs c_i q_{RSR} data points from nitrogen-containing reference samples. A weighted regression line is built from TiN, AlN, and CE650. An unweighted regression line is built from JK49, JK49* and CE650. Reduced measurements (as explained in Section 4.2.3) are plotted alongside, but were not used in the regression line calculation. A shaded range (far left) of c_i q_{RSR} marks the desired concentration in the CCS films.

Unlike with the oxygen calibration curve, there are no hydrogen effects present to distort the recorded intensities. Nor is there reason to suspect the N 149.267 nm emission line of self-absorption. One remaining possibility is spectral interference. The appendix in [23] calculates a possible chromium emission interference for the N 149.267 nm line. Chromium is present in both JK49 and Cr_xN, making this a potential culprit. As with the hydrogen effect, the Quantum software enables modification of the regression equation by adding a variable, in this case a dependence

on the measured chromium signal of the same sample.

Re-computing the nitrogen calibration curve with the inclusion of this chromium correction factor yields an impressive improvement in the fit across all samples. The updated curve is plotted in Figure 4.37. TiN, AlN, and CE650 contain no chromium, so their data points are left untouched. The JK49 and Cr_xN points are shifted leftward. The chromium correction factor is negative, meaning that the intensity recorded for these two samples actually results from an effectively smaller nitrogen concentration c_i q_{RSR}. Put another way, the chromium interference serves to reduce the recorded intensity of the N 149.267 nm line. This seems strange, as spectral interference more often results in a stronger intensity at the wavelength of detection, caused by additional emissions from the offending interference element. A weakening of some elemental signals is observed in the case of hydrogen, so there is some precedent for intensity suppression. The mechanism by which this could occur in the N 149.267 nm line due to the presence of chromium is not clear.

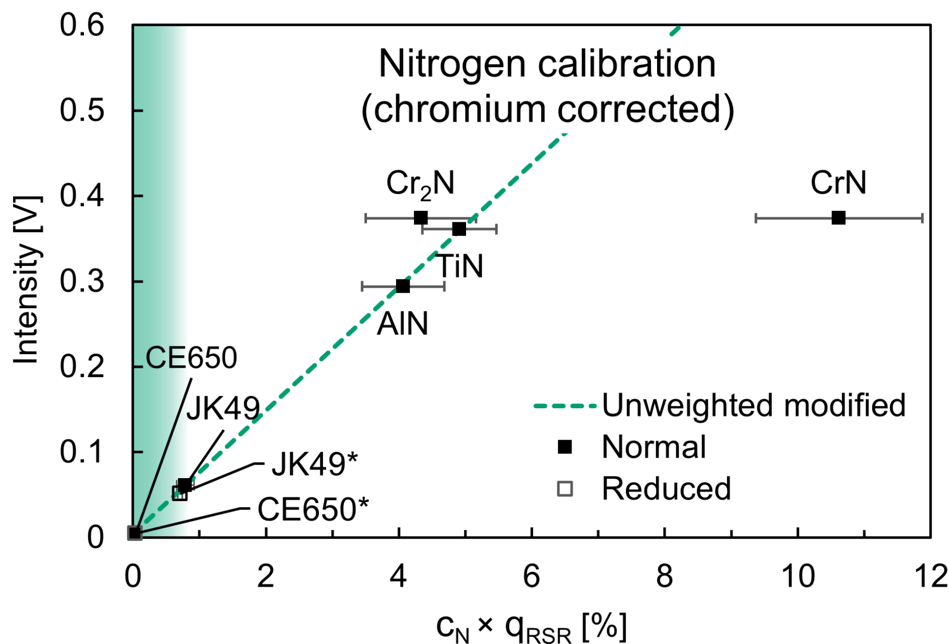

Figure 4.37: A re-plotting of the data points in Figure 4.36 after application of a negative chromium interference correction factor to the N 149.267 nm signal intensities. The JK49, JK49*, Cr_2N and CrN data points have all been shift left compared to Figure 4.36. Only an unweighted curve is presented. The reduced measurements are plotted alongside, but were not used in the regression line calculation.

The (unweighted) regression line in Figure 4.37 is calculated using TiN, AlN, Jk49, and CE650. As in the chromium calibration curve, the Cr_2N point fits the line more closely than the CrN. Indeed, when Cr_2N is included in the fitting process (curve not shown), the chromium calibration factor is able to shift it into line with TiN, AlN, and JK49. The same cannot be said of CrN, which remains displaced to the right of the curve (not shown).

The inclusion of interference corrections in the regression equation must be used cautiously. An improvement may be apparent simply because the additional correction parameter grants an extra degree of freedom [45]. The application in this instance seems justified, however.

An issue arises, though, when considering a sample containing chromium, but without nitrogen. Because the software assumes a suppression of the nitrogen signal in proportion to the chromium signal, it will wrongly attempt to correct a zero-intensity nitrogen signal up to a non-zero value. This is especially relevant in the CCS samples, where nitrogen levels are already low and chromium seemed to be incorporated more readily into the films. In the quantified results section, two versions will be presented: one which applies only the slope and intercept of the nitrogen calibration curve in Figure 4.37 (i.e. the chromium correction is used on the calibration samples, but not for the PLD samples), and another which additionally applies the chromium correction factor to the PLD samples.

The upper range of nitrogen expected in the CCS films is 10 at%, falling leftward of the JK49 data point. Like in the chromium calibration, more low-concentration samples would ideally be included. Future work could employ a different nitrogen emission line free of spectral interference.

Silicon

The silicon calibration curve (shown Figure 4.38) is formed by measurements on pure silicon, 1045, JK49, C276, and quartz. The metallic calibration samples contain only a small amount of silicon and so are clustered near the origin. The quartz sample, as noted before, produced very weak signals. The weighted and unweighted regression lines are quite similar and both pass well through the silicon data point, at the concentration range of interest. The unweighted curve fits slightly better and also passes closer to the origin.

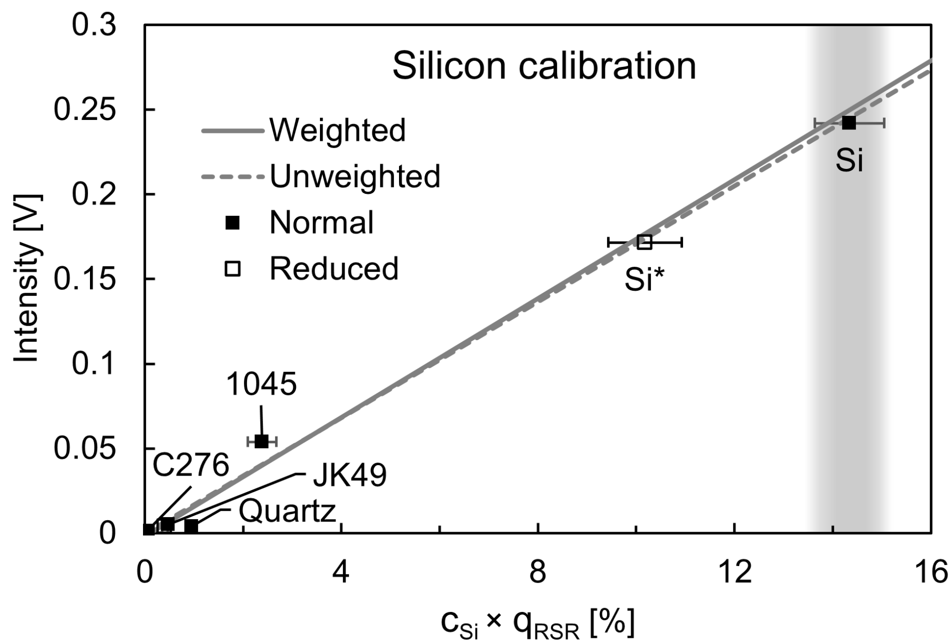

Figure 4.38: Calibration curves formed from the I_i vs c_i q_{RSR} data points from silicon-containing reference samples. Both a weighted and unweighted regression line are plotted. Reduced measurements (as explained in Section 4.2.3) are plotted alongside, but were not used in the regression line calculation. A shaded range of c_i q_{RSR} is the expected concentration in the silicon substrate of the CCS films.

The reduced Si* measurement lies nicely on the curve. The reduced JK49* and C276* points are omitted from the graph as they effectively overlap with the normal JK49 and C276 data points. This silicon calibration curve is of least consequence, and it is included only because the PLD substrate is silicon. It is expected that only concentrations of 0% and 100% will appear in the quantified GDOES results.

Calibration curve summary and validation

As a recap, the calibration curves which will be used for PLD film quantification are: unweighted titanium, weighted hydrogen-corrected oxygen, weighted 2nd-order chromium, unweighted silicon, and two versions of the unweighted chromium-corrected nitrogen curve - one based solely on the curve in Figure 4.37, and one which additionally applies a chromium-correction to the PLD sample nitrogen levels.

Ideally, this set of curves would be validated against additional CRMs to refine the curves and get an estimate of expected accuracy. Any available CRMs were already used for calibration in this work, so the only alternative is to use some of these calibration samples to check curve quality. The options within this set of calibration samples is limited even further, because calibration curves were only calculated for a selection of elements. Besides the five elemental curves shown here, aluminum and iron were the only other elements with sufficient data points to generate a curve.

The CE650 sample is one option whose elemental composition is covered by the available calibration curves (with the exception of 0.4 wt% tungsten). Applying the calibration to the data from Figure 4.12 yields (in wt%): 36.2% Al, 31.2% O, 27.6% Ti, 3.8% C, and 0.1% N. Compared to the specified concentrations in Table 3.3, the largest discrepancy is for titanium, which has a nominal concentration of 22.0%. The calculated density is 3.654 g/cm^3, a 17% increase compared to the input value of 3.113 g/cm^3. The calculated sputtered depth is 2.592 µm, a 12% reduction compared to the profilometer measurement of 2.932 µm.

The density estimation is simply based on a concentration-weighted sum of elemental densities (with a correction for oxides and nitrides). This method lacks the detail to take into account differing densities of different crystalline phases. Additionally, any errors in the calculated elemental concentration will translate into errors in the density. The depth calculated in the quantification process is, in turn, based on the estimated density at each timestep in the profile. The uncertainties in density and sputtering depth are related, then, to any inaccuracy in the quantified elemental concentrations.

The TiO_2 PLD film is also an interesting calibration sample to check. This quantification fares somewhat better; applying the calibration curves to the data in Figure 4.28 yields (in wt%): 57.3% Ti and 40.0% O, with the balance made up of contaminating signals such as C, Si, and N. The calculated density is 4.144 g/cm^3, 9.6% higher than the input value of 3.780 g/cm^3. This density more closely matches that of rutile TiO_2. Again, though, the model is based purely on elemental concentrations and cannot factor crystal phase. The calculated film thickness is approximately 180 nm, a 10% decrease compared to the ellipsometry value of 200 nm.

The estimated error of this calibration is larger than ideal. The quantitative results presented at the end of the chapter should be interpreted with this in mind.

The inclusion of more CRMs, and perhaps a more thorough application of software corrections, could help to improve the performance. The mediocre quality of the calibration curves, however, does not diminish the use of GDOES for qualitative analysis and comparison.

4.4 PLD plume films - qualitative

Before applying any of the calibration curves for quantitative results, the qualitative GDOES measurements will be presented for the fabricated PLD films. In the following results, only Ti, O, Cr, N, Si, H, and C are plotted, using the same colors as in the calibration GDOES profiles. The GDOES profile for each sample contains an inset photograph of the wafer and the marked crater. The measurement position naming (with exception of P-CrN-O-700) is based on the closest point in the wafer alignment template (see Figure 3.10). Typically, measurements were made at pt. 21, the upper left near the wafer flat, in order to leave the plume center intact for other measurements. Some samples, however, received additional measurement at other locations. As a reminder, all the PLD samples are deposited on a 2" (50.8 mm) diameter silicon wafer, and the GDOES crater has a diameter of 4 mm. All measurements extend completely through the deposited layer and into the silicon substrate. All three samples deposited using the CrN target are plotted with the same Y-axis range, for easier signal comparison. Likewise for the four samples deposited using the TiO_2 target.

P-CrN-O-700

The qualitative GDOES profile of P-CrN-O-700 is shown in Figure 4.39, along with a photograph of the wafer and measurement position. The measured position presented for this sample is near the plume center, where the film is thickest. While some nitrogen is present, it is apparent that merely ablating CrN in O_2 results in noticeable oxygen incorporation into the film. This finding aligns with the previous suspicion which prompted the N_2-O_2 gas cycling idea. The chromium signal has an oscillatory appearance, suggesting an optical interference effect as described in Section 2.2.4. The chromium emission line used for detection is 425.439 nm (or 2.91 eV), which should be absorbed by non-transparent CrN to nullify the interference effect. The optical response has clearly been altered by the presence of Cr_2O_3. Some aluminum signal (Al 396.157 nm) was also recorded in the film (not plotted). This could possibly be attributed to spectral interference from chromium (which has a weak line at 396.369 nm) [36], however the aluminum did not appear in the GDOES profiles for any of the following chromium-containing samples.

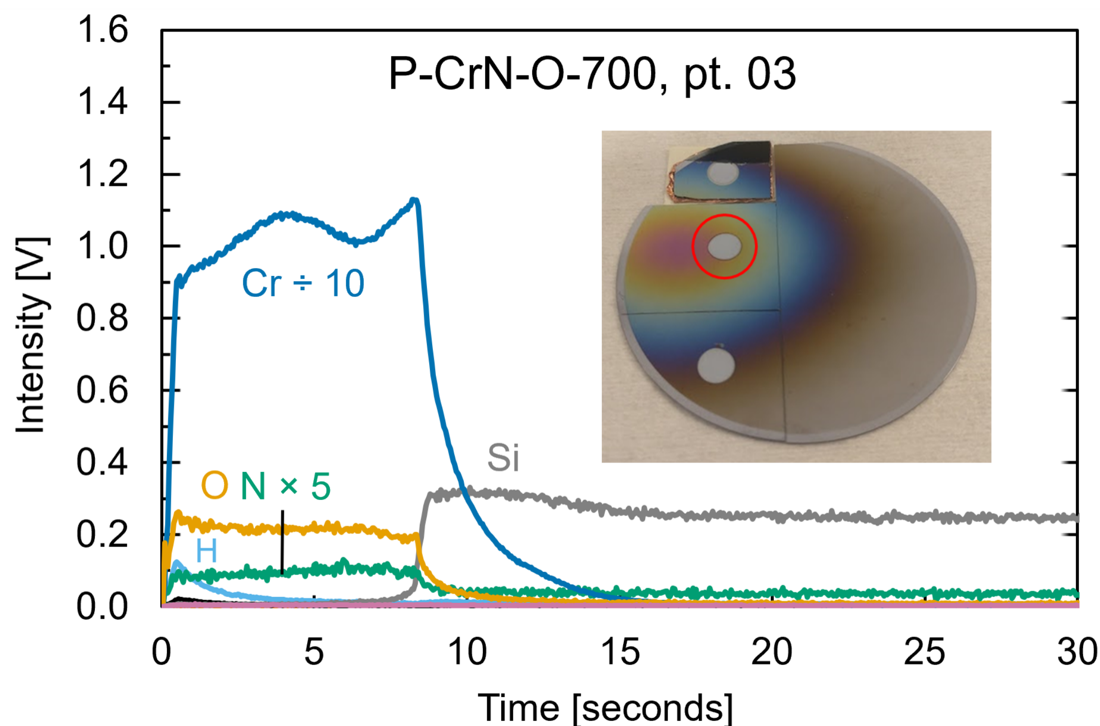

Figure 4.39: GDOES profile of CrN-ablated plume film, deposited in O_2 atmosphere at 700°C.

P-CrN-N-cy-O-700

The qualitative GDOES profile of P-CrN-N-cy-O-700 is shown in Figure 4.40, along with a photograph of the wafer and measurement position. The measured position on this sample is, once again, near the plume center. Although ablation and deposition took place only in N_2, the cycling periods to O_2 have still introduced oxygen into the film. The rising shape of the chromium signal appears similar to the first crest in the previous sample, so the optical interference effect could be involved here as well. Without seeing more oscillations though (due to the thinness of the film), it is difficult to say conclusively.

It is strange that the nitrogen signal would be weaker for this sample compared to the previous one. Possibly, the combination of elevated substrate temperature (700°C) and the addition of waiting periods during the gas cycling provided more opportunity for desorption of deposited nitrogen from the film back into the chamber. In any case, observing the undesired effect of mere O_2 atmosphere exposure prompted the TiO_2-in-N_2 capping idea.

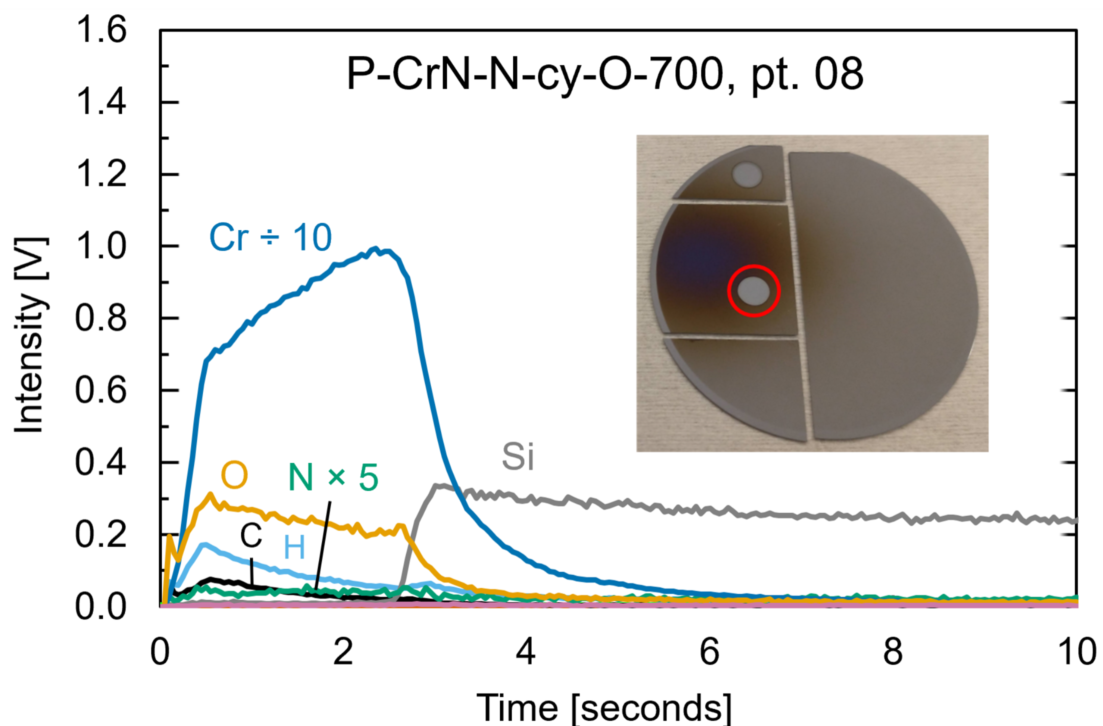

Figure 4.40: GDOES profile of CrN-ablated plume film, deposited in N_2 atmosphere at 700°C, with periodic intervals of cycling to O_2 without deposition.

P-CrN-N-550

To conclude the series of PLD films deposited using the CrN target, this final sample GDOES measurement is plotted in Figure 4.41, along with a photograph of the wafer and measurement position. The GDOES profile displays the desired strong nitrogen signal. Note that, unlike the previous two samples, the nitrogen signal here is not scaled by 5. The nitrogen intensity plateaus around 0.326 V. The chromium signal is also higher than the preceding cases, averaging 14.32 V.

Consider the GDOES profile from the CrN PLD target which was used to deposit this film: the nitrogen signal intensity was 0.374 V and the chromium intensity was 19.41 V (see Figure 4.16 and Table 4.1). Thus, the nitrogen signal in this plume film is 87% of the target, and the chromium signal is 74%. That both signals are lower could stem from differences in the material densities, or from the silicon substrate having a higher resistance (and lower sputtering rate) than the CrN PLD target. The material transfer from the target is apparently not quite stoichiometric though. The relative nitrogen signal may be higher than the relative chromium signal because the deposition took place in a background gas of N_2, which was somewhat incorporated into the film. Additionally, it is also expected that the lower substrate temperature of 550°C is more suited for nitrogen retention in the film [49].

The oxygen signal is not completely absent though. It is possible that the CrN PLD target surface was oxidized to a degree in a previous N_2-cycle-O_2 deposition, and this could explain the transfer source.

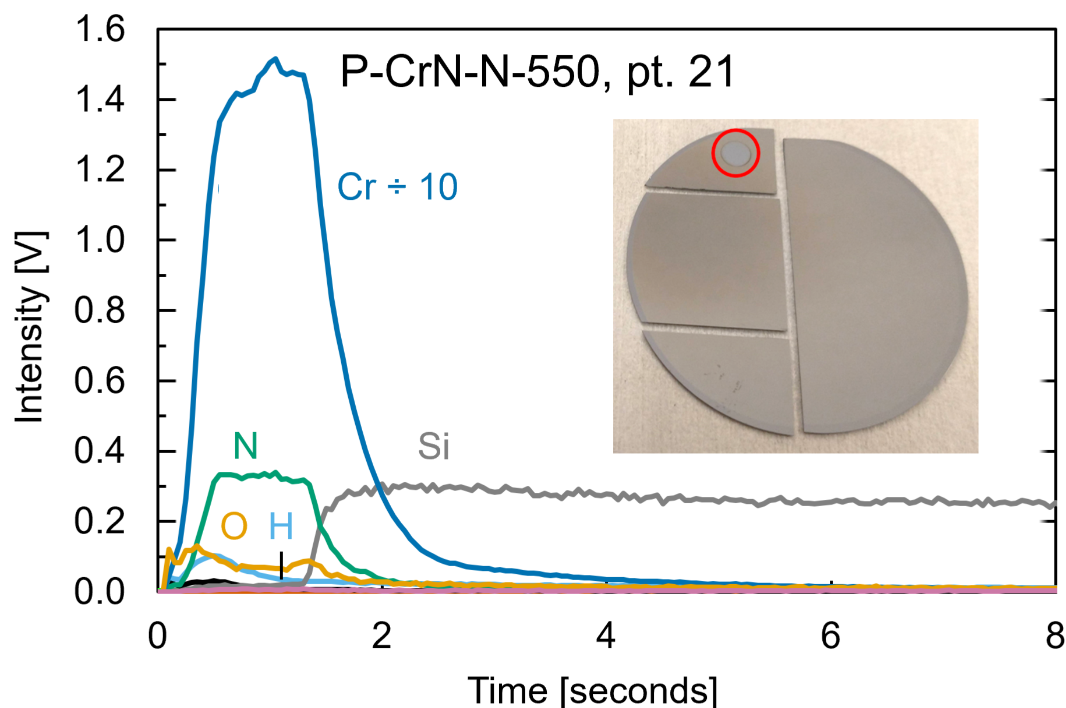

Figure 4.41: GDOES profile of CrN-ablated plume film, deposited in N_2 atmosphere at 550°C.

P-TiO_2-O-700

Shifting now to the TiO_2 PLD plume films, the first is a deposition solely in O_2 background gas, at a high substrate temperature of 700°C. The qualitative GDOES profile of P-TiO_2-O-700 is shown in Figure 4.42, along with a photograph of the wafer and measurement position. The titanium signal oscillations are the result of optical interference. The spectrometer uses the 365.355 nm (3.38 eV) emission line for titanium, which is slightly beyond the absorption edge determined for these samples by ellipsometry. Thus, plasma emissions directed back toward the sample reflect both at the film surface and also transmit through to reflect from the silicon substrate, satisfying the conditions for interference as explained in Section 2.2.4. The O, H, and C lines are at shorter wavelengths, so these are absorbed by the film without generating any oscillations at the detector. This effect can be removed in the software, but it is left unaltered for these qualitative results (in part because the smoothing algorithm fails with some of the thinner films presented later).

The decaying shapes of the hydrogen and carbon signals have the appearance of surface contamination. However, a slight bump is visible in the hydrogen intensity at the silicon interface. This could be contamination on the silicon wafer prior to deposition, or it could result from minor hydrogen incorporation during film deposition, which subsequently concentrated at the interface. In any case, the presence of hydrogen in the plasma can have a variety of complicating effects, as presented in Section 2.2.4.

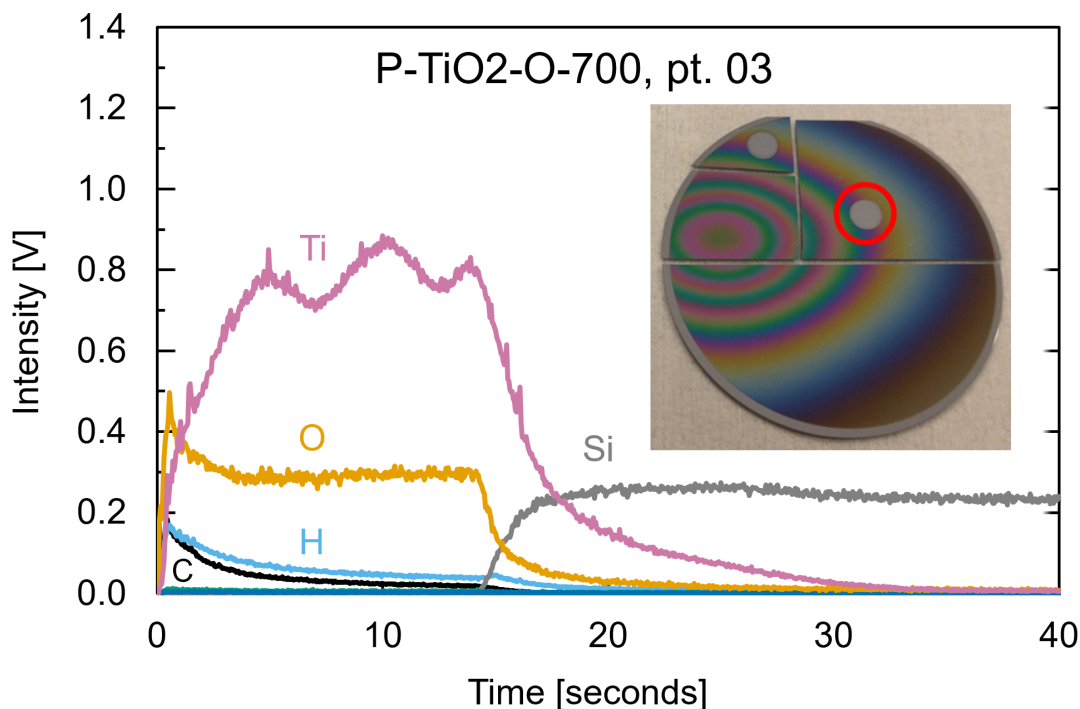

Figure 4.42: GDOES profile of TiO_2-ablated plume film, deposited in O_2 atmosphere at 700°C.

P-TiO_2-O-550

This sample is similar to the previous, with the difference being the substrate heating temperature has been dropped to 550°C, and fewer pulses were used resulting in a thinner film. The qualitative GDOES profile is shown in Figure 4.43, along with a photograph of the wafer and measurement position. The titanium and oxygen intensities are slightly weaker than in the previous sample, and the hydrogen and carbon signals are more apparent.

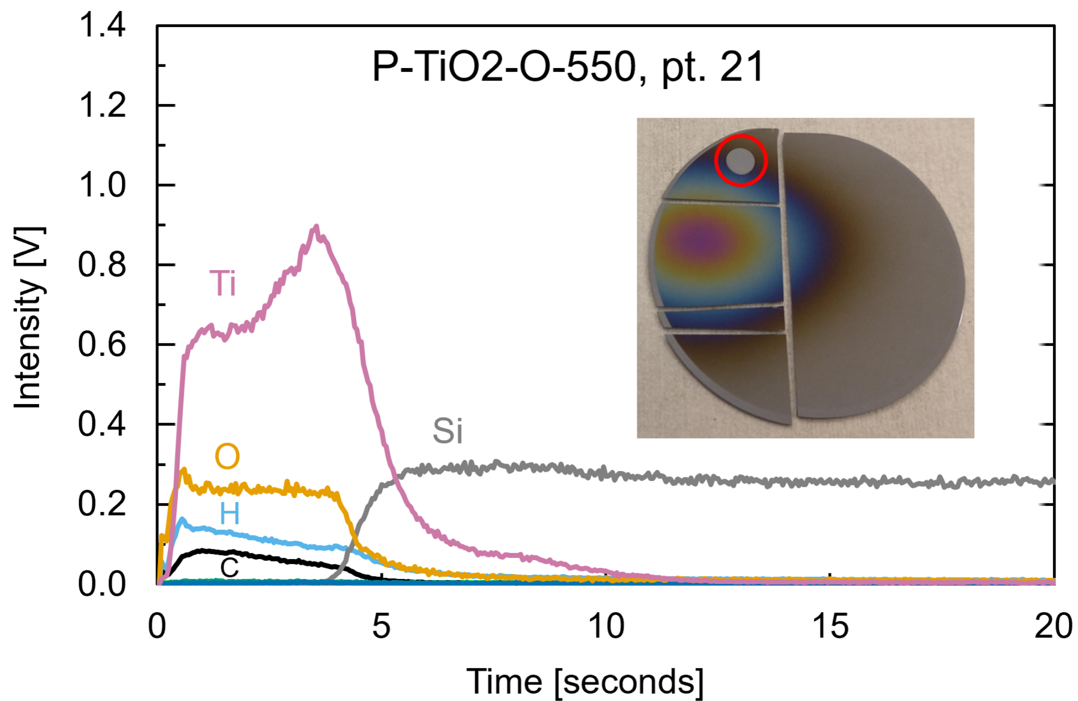

Figure 4.43: GDOES profile of TiO_2-ablated plume film, deposited in O_2 atmosphere at 550°C.

P-TiO_2-N-cy-O-700

This sample tested the effect of TiO_2 ablation in a N_2 environment, with additional cycles to O_2. The qualitative GDOES profile is shown in Figure 4.44, along with a photograph of the wafer and measurement position. Compared to P-TiO_2-O-700, a higher titanium signal intensity is recorded for this film, as well as a smaller oxygen signal, and a non-zero nitrogen signal.

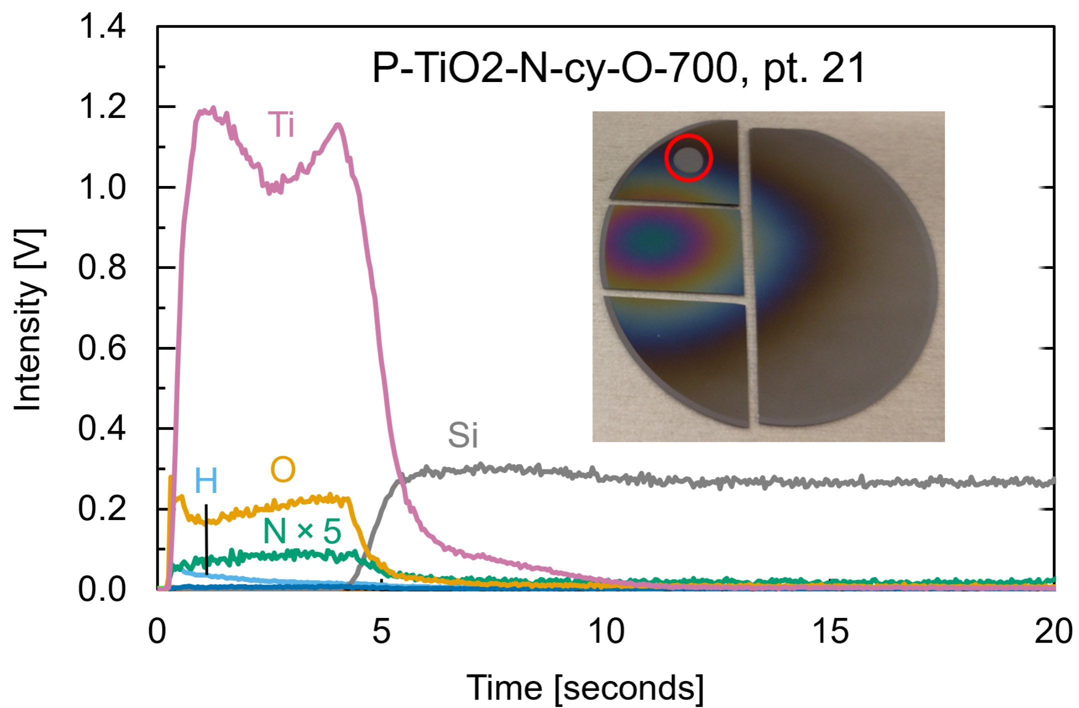

Figure 4.44: GDOES profile of TiO_2-ablated plume film, deposited in N_2 atmosphere at 700°C, with periodic intervals of cycling to O_2 without deposition.

P-TiO_2-N-cy-O-550

This sample is comparable to the previous, but was deposited on a lower-temperature substrate. The qualitative GDOES profile of P-TiO_2-N-cy-O-550 is shown in Figure 4.45, along with a photograph of the wafer and measurement position. The magnitude of the titanium intensity is similar as the previous sample. The oxygen signal is slightly higher, and the nitrogen signal is 3x larger, clearly demonstrating that lower temperatures are more favorable for nitrogen incorporation.

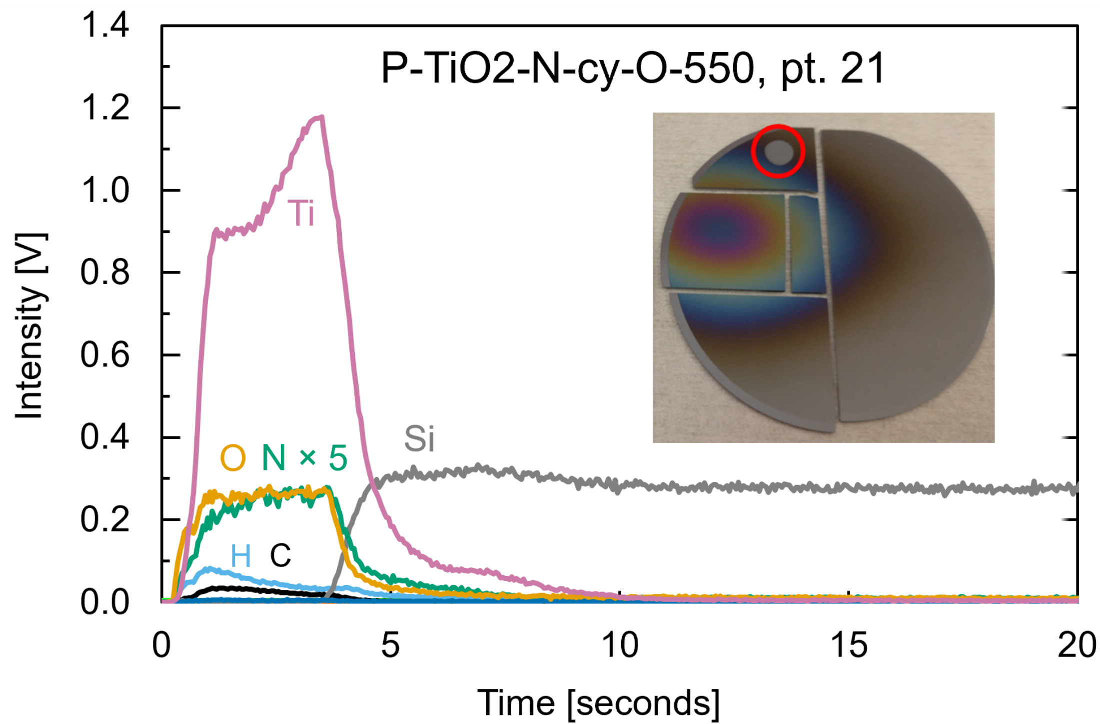

Figure 4.45: GDOES profile of TiO_2-ablated plume film, deposited in N_2 atmosphere at 550°C, with periodic intervals of cycling to O_2 without deposition.

4.5 PLD CCS films - qualitative

In this next section, GDOES profiles of three CCS films, made using combinatorial PLD, are presented. These wafers were already partitioned for other experiments, so the central, flattest section containing the plume centers and wafer center were not available for measurement. In order to get a sense of the elemental gradient, GDOES measurements were taken laterally across the wafer, starting at the left-side (where doping concentrations are lowest) and moving toward the right (where higher doping concentrations are expected). In order to form a sufficient chamber seal with the O-ring, a margin (approximately 6 mm) around each measurement position is required. This prevented measurement closer to the cleaved center line and limited four measurements side-by-side. A photo of each wafer is included with its four measurement positions. The thickness fringes indicate that the film thickness is similar in each measurement.

CCS-O-700

This sample (photographed in Figure 4.46) represents the simplest approach to create a continuous compositional spread using combinatorial PLD. The entire deposition took place in an O_2 background gas, with an elevated substrate temperature. With regard to the plume films, the profiles here are expected to be most similar to P-TiO_2-O-700 at pt. 01, with increasing influences in accordance with P-CrN-O-700 moving toward pt. 04.

The four measurement positions are plotted together in Figure 4.47 using identical axes for time and intensity, and identical scaling factors for chromium and nitrogen. The familiar optical interference oscillations are observable for all the titanium signals, as well as for chromium. Beginning at pt. 01, this position is expected to have the least amount of Cr and N doping. A noticeable chromium signal is already present at this position, as well as a very small nitrogen signal. The oxygen signal takes some seconds to level out, which differs from the flat profile seen at the other positions. In pt. 02, the chromium signal has increased, the titanium signal has reduced slightly, and the other signals are largely the same. For pts. 03 and 04, the chromium intensity continues to increase, as does the nitrogen, although it is difficult to see. The remaining signals are mostly unchanged. A decaying hydrogen signal is also present at the surface in each position. The diminutive nitrogen signals are as expected, considering the results from P-CrN-O-700. An O_2 background and 700°C substrate temperature are not conducive to nitrogen deposition. SIMS measurement of this sample found noticeable concentration gradients in chromium and nitrogen at the surface compared to the bottom of the film [49]. This is not apparent in the GDOES depth profile, although the oscillations slightly obscure any possible trend.

Figure 4.48 is a more concise comparison of the Ti, O, Cr, and N signals at each

position, averaged between time 2-16 s, where the GDOES profiles are stable in the film. The trends are as noted above: slightly stronger titanium and weaker oxygen at pt. 01, and steadily increasing chromium and nitrogen signals. The rising nitrogen intensity is more apparent here, when plotted on it's own axis.

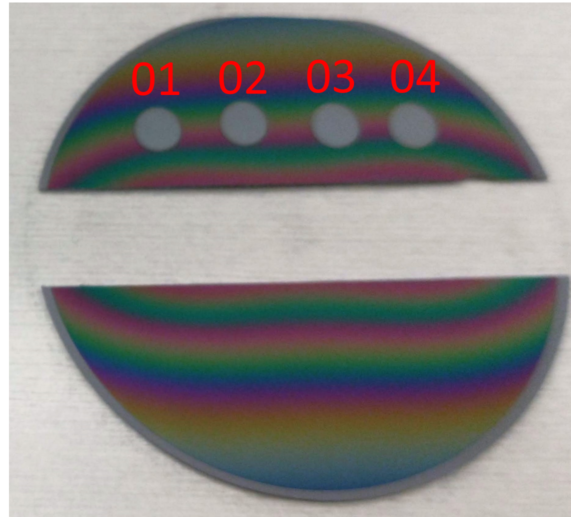

Figure 4.46: A photograph of the combinatorial PLD sample CCS-O-700. The center segment was taken for other experiments. Four (labeled) measurement positions are visible, spanning from left (where minimal Cr and N doping is expected) to right (where maximum Cr and N doping is expected). The film is deposited on a 2" diameter silicon wafer substrate. The GDOES crater spots are 4 mm in diameter.

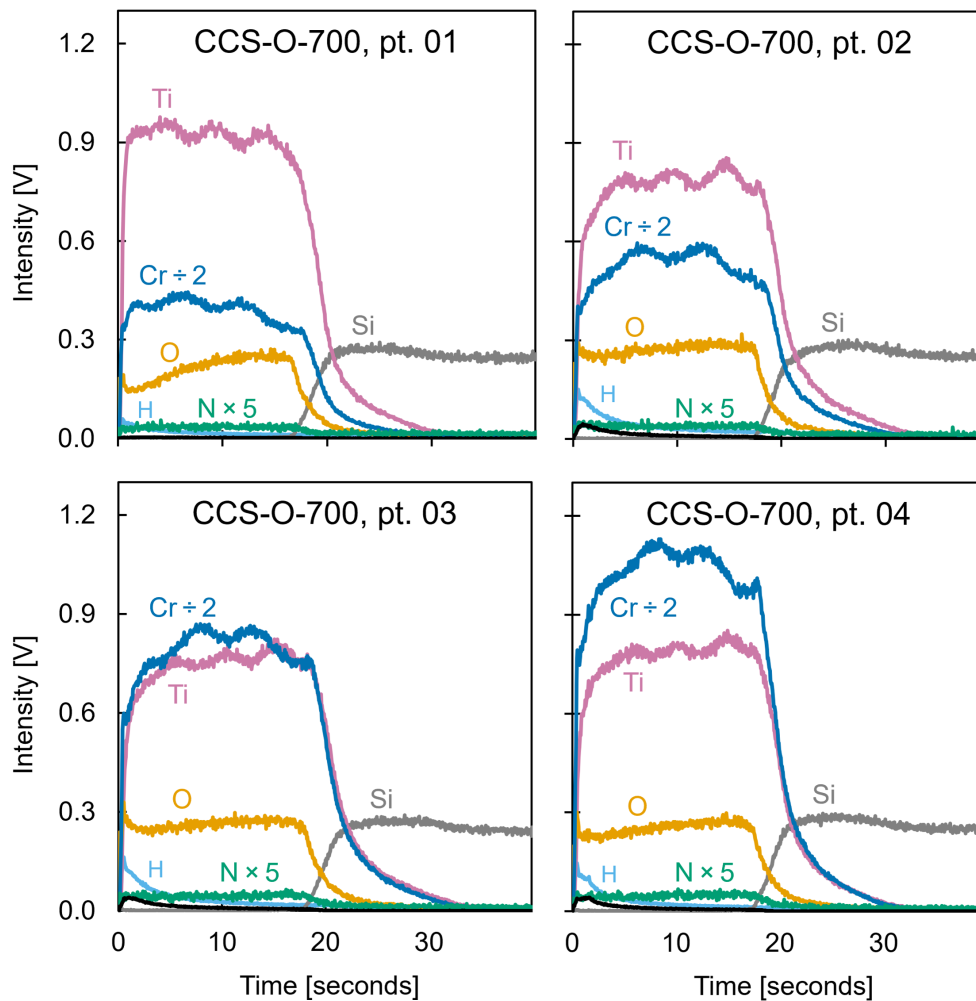

Figure 4.47: Qualitative GDOES profiles of the four positions measured on CCS-O-700. The chromium and nitrogen signals have been scaled by $\frac{1}{2}$ and 5, respectively.

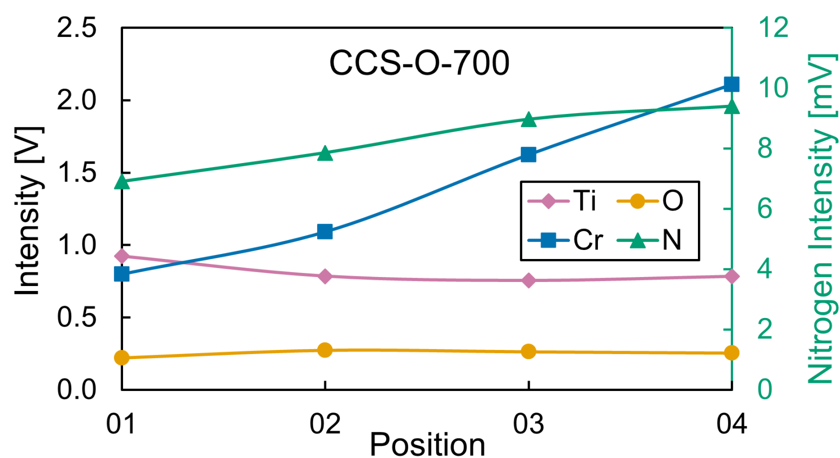

Figure 4.48: A comparison of average signal intensities at each position between 2-16 seconds. The intensity values are un-scaled, but nitrogen is plotted on the secondary Y-axis in mV.

CCS-Cap-NoCr

As a reminder, this sample was fabricated as a test of the capping idea, where some rounds of TiO_2 ablation would take in a N_2 environment (at deposition position 2). In order to isolate the effects of this capping, no CrN ablation took place. Therefore, this sample is akin to P-TiO_2-O-550 on the left, and P-TiO_2-N-cy-O-550 on the right. Figure 4.49 provides a photograph of the sample and the four GDOES measurement positions. The vertical cleavage of this sample forced the GDOES measurements slightly closer together on each side.

The results from the four measurement positions are plotted together in Figure 4.50 using identical axes for time and intensity, and an identical scaling factor for nitrogen. The titanium and oxygen signals are largely unchanged at each point, except for a slightly lower oxygen intensity at pt. 01. The nitrogen profiles at pts. 01 and 02 are nearly the same, but the signal intensity rises at pts. 03 and 04, the side where the capping depositions took place. Obviously there is no chromium to analyze.

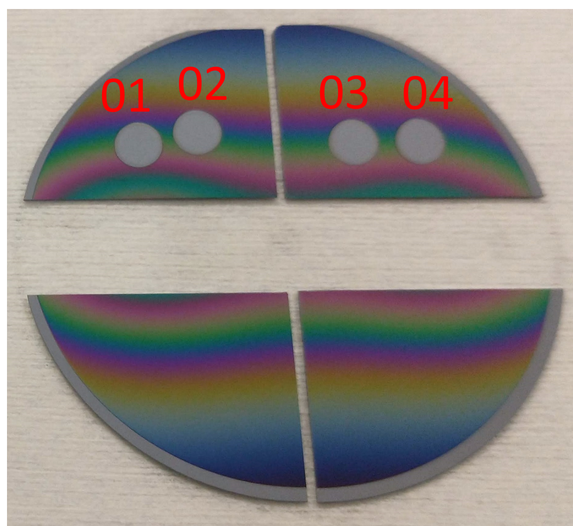

Figure 4.49: A photograph of the PLD sample CCS-Cap-NoCr. The center segment was taken for other experiments, and the wafer was further cleaved vertically. Four (labeled) measurement positions are visible, spanning from left (the side of the TiO_2 ablation purely in O_2) to right (where the TiO_xN_y capping is thickest). The film is deposited on a 2" diameter silicon wafer substrate. The GDOES crater spots are 4 mm in diameter.

There is no need for a comparative plot since the nitrogen signal is the only varying quantity of interest. It roughly doubles in intensity at pt. 04 compared to pt. 01, going from 10.7 to 23.2 mV. Interestingly, the magnitude of the nitrogen signal achieved here by capping (23.2 mV) surpassed the magnitude displayed in the previous sample (9.4 mV) based on deposition from the CrN target. Besides reiterating the benefits of low substrate temperature and N_2 background gas for nitrogen retention in the film, this also highlights the importance of accounting for

this nitrogen contribution when targeting specific doping levels in future capped samples.

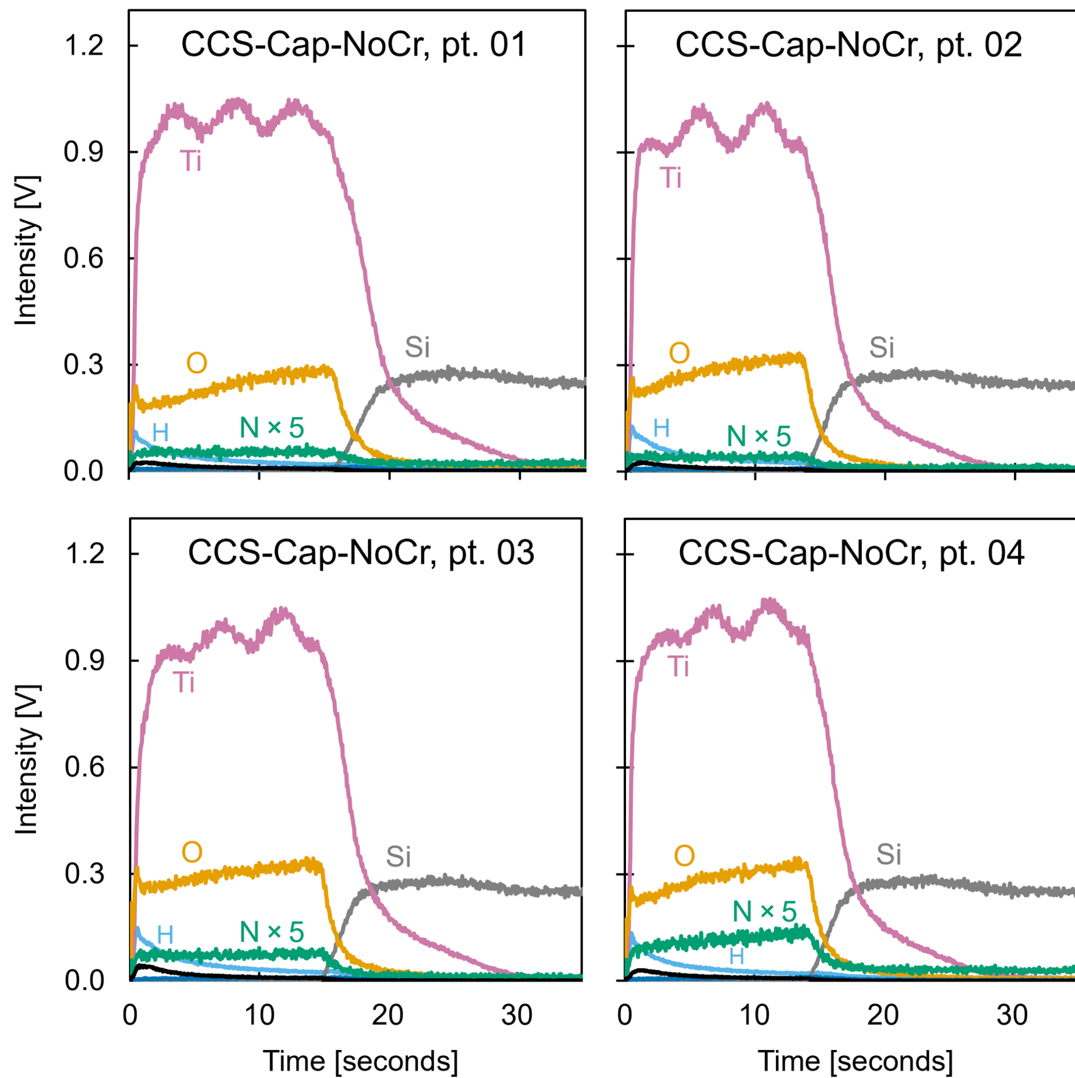

Figure 4.50: Qualitative GDOES profiles of the four positions measured on CCS-Cap-NoCr. The nitrogen signal has been scaled up by a factor of 5 for better visibility.

CCS-Cap1

CCS-Cap1 is the culmination of this batch of PLD samples, designed based on the PLD simulation work, and including both Cr and N doping and TiO_xN_y capping. A photograph is provided in Figure 4.51.

The measurements from the four positions are plotted together in Figure 4.52 using identical axes for time and intensity, and identical scaling factors for chromium and nitrogen. The results match with the findings from the previous samples. While the titanium and oxygen signals don't change much from pt. 01 to pt. 04, the chromium and nitrogen profiles steadily intensify, as expected.

The titanium oscillations, which have appeared in many profiles so far, seem to dampen in magnitude. This is related to the changing optical properties of the film with Cr and N inclusion. As the absorption edge creeps lower in energy due to sub-bandgap energy levels, the film is no longer completely transparent to the Ti 365.355 nm (3.38 eV) emission line, weakening the effect of optical interference. The Cr 425.439 nm (2.91 eV) line remains in the transparent range.

The trend in average signal intensities across the four positions is shown in Figure 4.53. The rise in intensity across the measured positions is linear for both chromium and nitrogen. Comparing pts. 01 and 04, the chromium intensity increases 276%, from 1.24 V to 3.41 V. The nitrogen intensity increases 462%, from 14.5 mV to 66.9 mV.

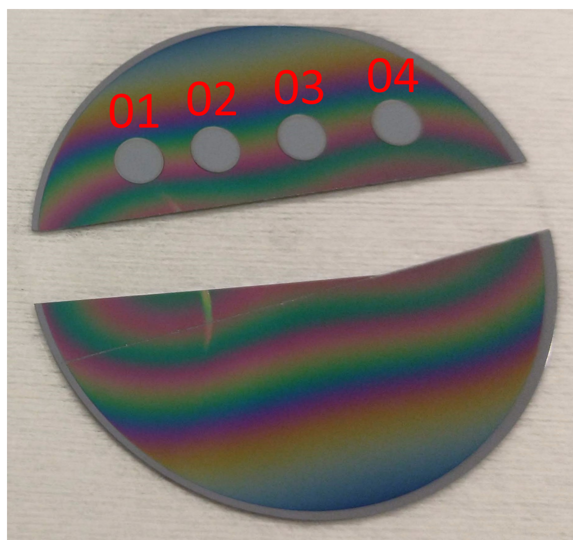

Figure 4.51: A photograph of the combinatorial PLD sample CCS-Cap1. The center segment was taken for other experiments. Four (labeled) measurement positions are visible, spanning from left (where minimal Cr and N doping is expected) to the right (where maximum Cr and N doping is expected). A mysterious "scratch" is visible spanning the gap on the left side, but does not overlap any GDOES measurements. The film is deposited on a 2" diameter silicon wafer substrate. The GDOES crater spots are 4 mm in diameter.

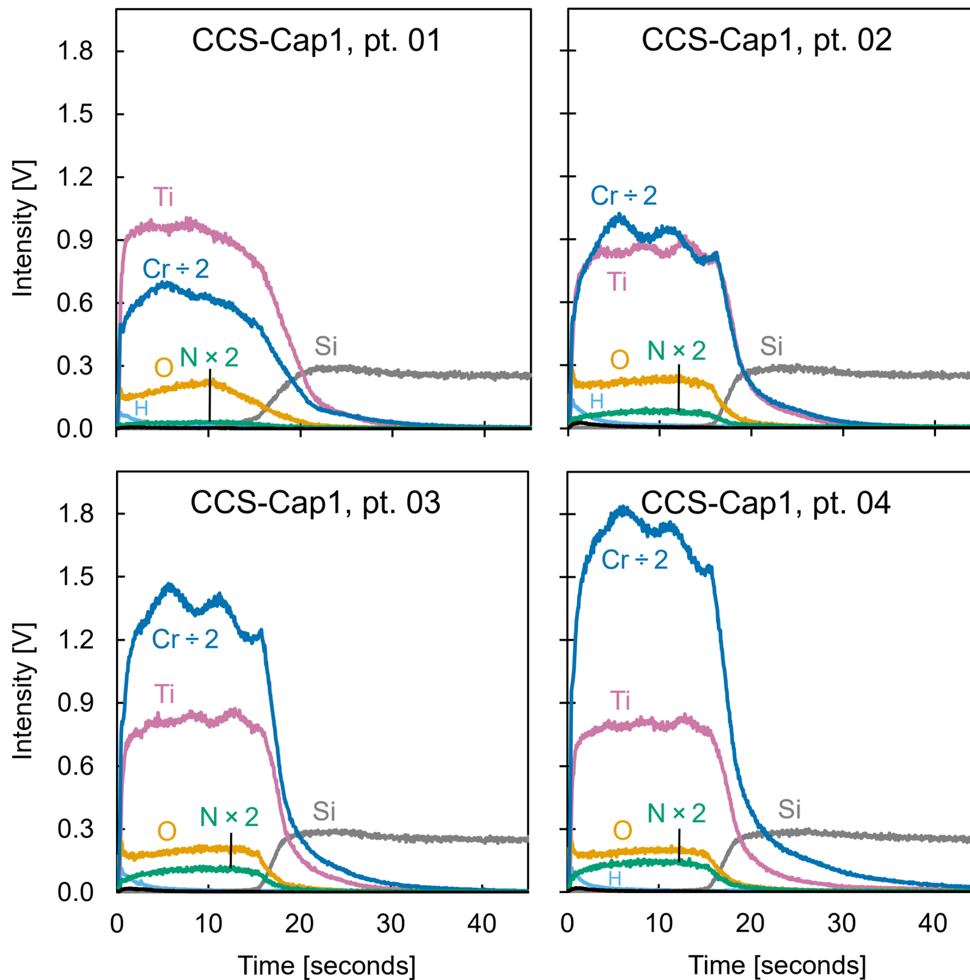

Figure 4.52: Qualitative GDOES profiles of the four positions measured on CCS-Cap1. The chromium and nitrogen signals have been scaled by $\frac{1}{2}$ and 5, respectively.

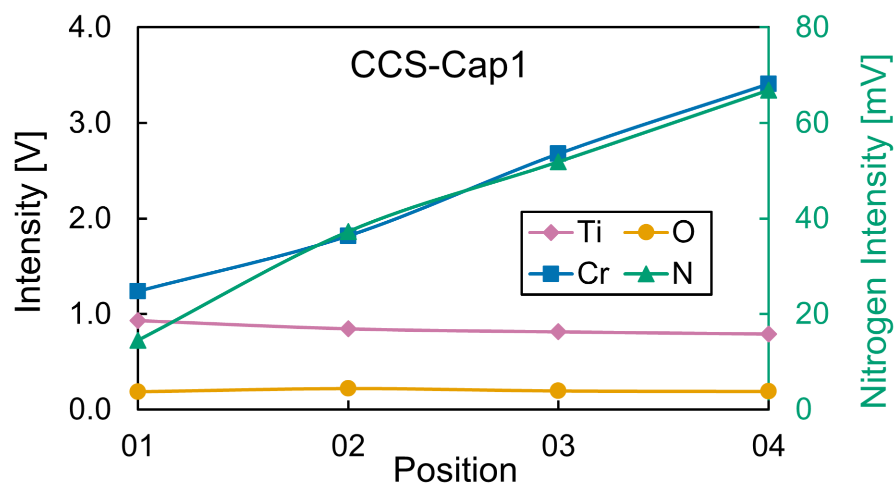

Figure 4.53: A comparison of average signal intensities at each position between 2-15 seconds. The intensity values are un-scaled, but nitrogen is plotted on the secondary Y-axis in mV.

4.6 PLD CCS films - quantitative

Now, the calibration curves developed in Section 4.3 are applied to the PLD CCS film GDOES profiles to give quantified elemental concentrations. As in the previous section, all four measurement locations on each sample will be plotted together for comparison, using at% on the y-axis. Any optical interference oscillations present in the qualitative profiles of the CCS samples were smoothed out in software before quantification. For CCS-O-700 and CCS-Cap1, two versions of the quantified results will be presented. The first uses the nitrogen calibration curve as in Figure 4.37 but does not apply the chromium-interference correction factor to the measured signals. The second uses the nitrogen curve and additionally attempts to correct (increase) the nitrogen intensity in accordance with the chromium intensity.

Average concentration percentages are included with the data labels, based on a selected range between the sample surface and the onset of the silicon signal. These do not always sum precisely to 100% because of non-zero concentration contributions from other unplotted elements.

Prior elemental characterization of these films includes results from SIMS (for Cr and N) and EDX (for Cr). These measurements, however, took place along the center-line of the wafers, which was not available for GDOES measurement [51]. The SIMS and EDX results can be extrapolated to a degree, and this forms a basis for comparison, along with the PLD simulation results for doping concentration across the samples.

Given the uncertainty of the calibration, there is no need to plot quantified profiles for all of the PLD plume films.

CCS-O-700

The first set of quantified results for the four GDOES measurements on CCS-O-700 are plotted together in Figure 4.54 (referring to the positions shown in Figure 4.46). The nitrogen concentrations here are calculated using the measured intensity and the calibration curve in Figure 4.37. As was seen in the qualitative profiles (see Figure 4.47), the nitrogen incorporation into this film was minimal, even at pt. 04 closer to the 2nd plume center. The chromium content is more in agreement with the simulated concentrations. The TiO_2 is closest to stoichiometric at pt. 01. Moving further right on the wafer sees the titanium concentration drop to around 20 at% at pts. 02-04. The oxygen concentration jumps up at pt. 02, then decreases at pt. 03 and 04 as the chromium content increases.

The film thickness at these points is calculated by the calibration to be between 190-230 nm. The titanium and oxygen signals decay into the silicon substrate for another 300 nm. This may be due to diffusion during deposition on the high-temperature substrate, or it could simply be an effect of a non-flat crater shape at the

layer interface. The calculated density for the film at these four positions is 4.0-4.3 g/cm^3. For pure TiO_2, this falls in the range of rutile rather than anatase. Recall though, in the calibration curve validation based on F-TiO_2-O-700-opt (Section 4.3), a density consistent with rutile was also reported, even though the film is anatase according to other methods. The doping of chromium would also have the effect of increasing density.

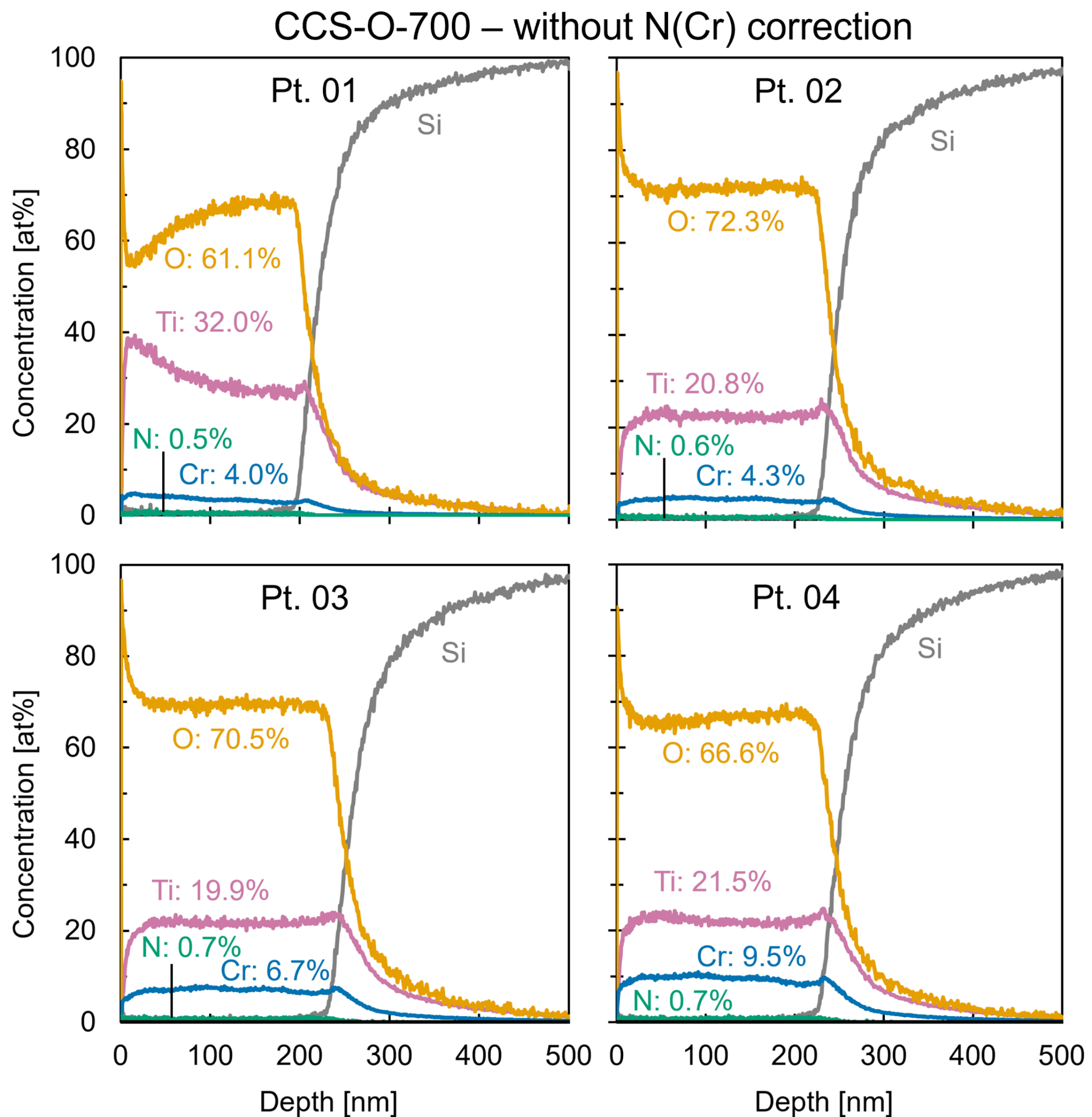

Figure 4.54: Composition depth profiles of four measurement positions on CCS-O-700. The calibration curves used were Ti, O, Cr, N (without any intensity correction), and Si.

The CCS-O-700 profiles in Figure 4.55 relies on the same measurements as in 4.54, but the calibration was applied after the raw nitrogen intensities had been scaled up proportional to the chromium signal. The effect is quite noticeable, as the nitrogen concentrations are much larger than in Figure 4.54 and nearly coincident

with the chromium profiles. Both values roughly double at pt. 04 compared to pt. 01. The trends in titanium and oxygen content are similar to that mentioned above. The addition of nitrogen content here takes place at the expense of oxygen. The calculated densities and layer thicknesses are similar to the previous calibration.

The difference in nitrogen concentration between Figures 4.54 and 4.55 highlights the impact caused by changes in the set of calibration curves. The results in the first plot (without chromium-corrected nitrogen levels) are more in agreement with the SIMS measurements taken on this sample [49]. One of the purposes of exploring GDOES, however, was to consider if it might give more reliable results for nitrogen at higher concentrations.

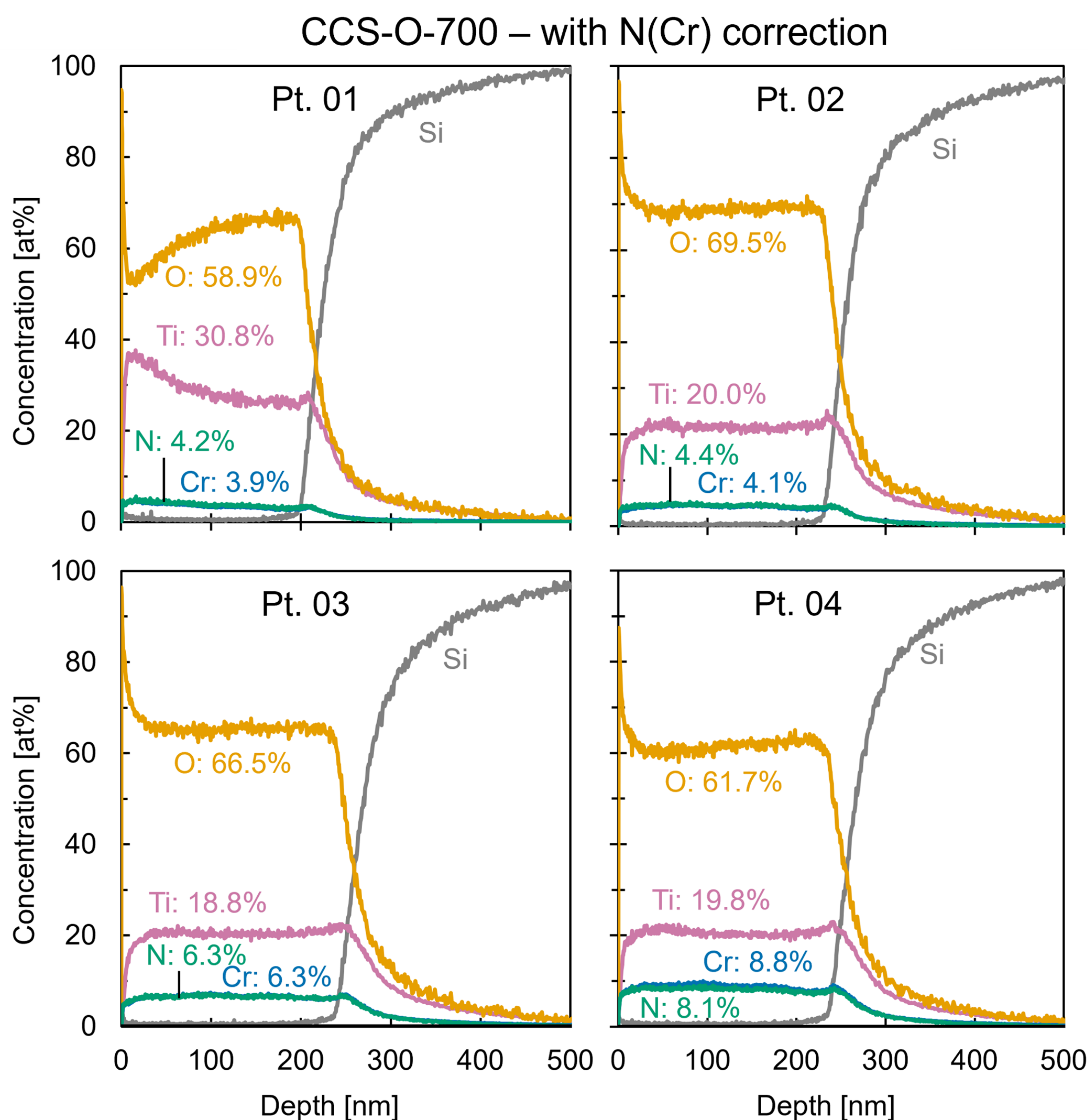

Figure 4.55: A comparable CDP of CCS-O-700 to Figure 4.54, but using a nitrogen calibration that includes a correction to nitrogen concentration according to interference from the chromium signal.

CCS-Cap-NoCr

Figure 4.56 displays the quantified GDOES profiles for four measurements along sample CCS-Cap-NoCr (referring to the positions shown in Figure 4.49). This sample contains no chromium, so there is no difference in results when using the nitrogen calibration curve with/without the chromium correction factor. The quantitative results do not contain so much more information than the qualitative ones in Figure 4.50. The main finding is simply that the capping processes introduces a small concentration of nitrogen into the film, more so on the the plume center $\times_2$ side of the wafer.

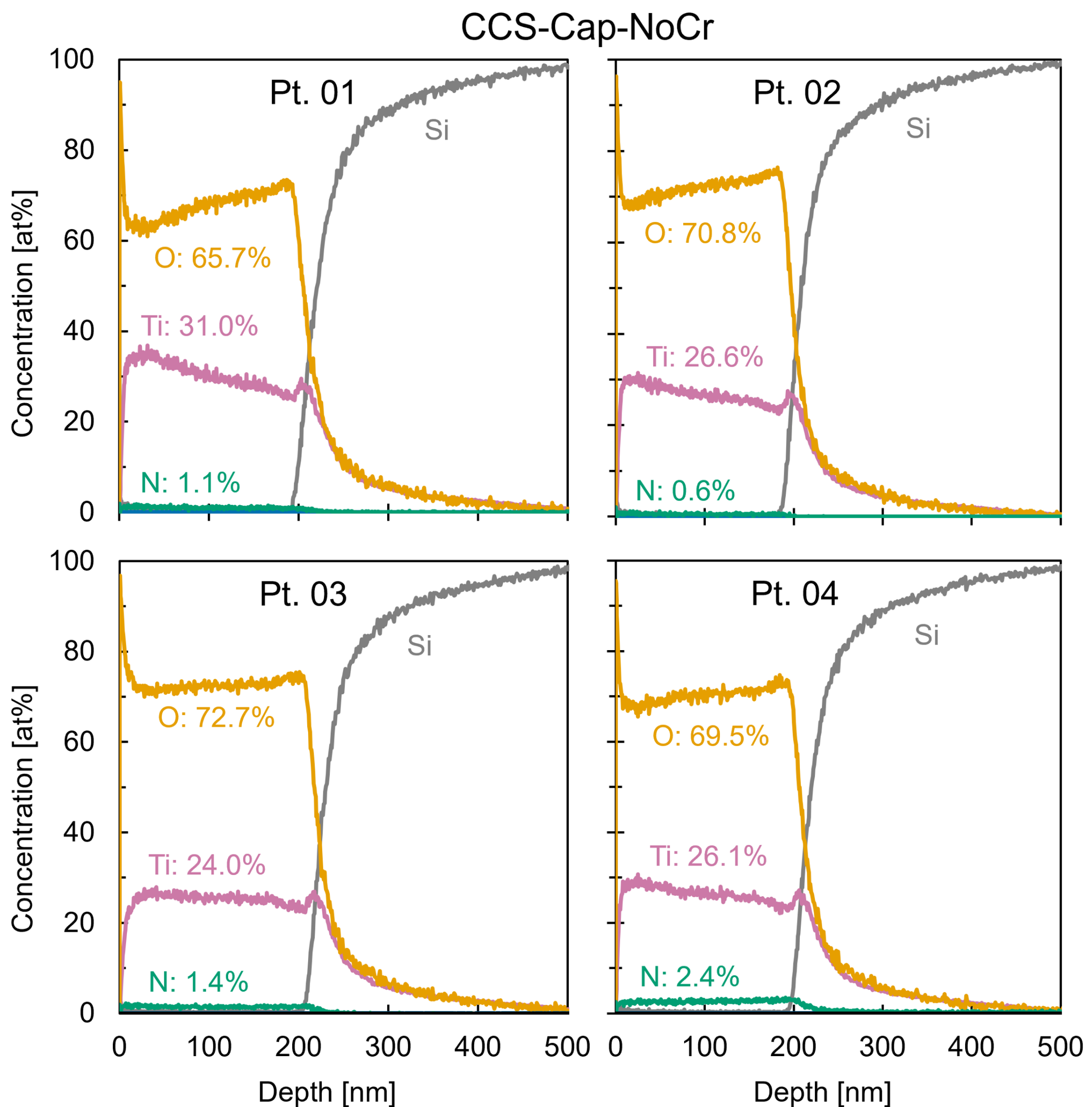

Figure 4.56: Composition depth profiles of four measurement positions on CCS-Cap-NoCr. The calibration curves used were Ti, O, Cr, N (without any intensity correction), and Si.

As in CCS-O-700 above, pt. 01 displays a lower oxygen concentration and higher

titanium concentration compared to pts. 02-04. Indeed, the film at pt. 01 is the closest to stoichiometric TiO_2, with the other pts. displaying an abundance of oxygen. The slight upward slope in the oxygen profiles could be due to a hydrogen effect, where the software is suppressing the oxygen signal intensity near the surface (in accordance with a decaying hydrogen signal, see Figure 4.50). Since the sum of all elemental concentrations must equal 100%, a slope in the oxygen line forces a mirrored slope in the titanium line.

The calculated density is in a slightly decreased range compared with the previous sample: 4.0-4.2 g/cm^3. This makes sense given the absence of chromium. The film depth calculated at these four positions is around 190-200 nm.

CCS-Cap1

First, the CCS-Cap1 profiles are quantified without any chromium-interference corrections to nitrogen. The results at the four measurement positions are presented in Figure 4.57 (referring to the positions shown in Figure 4.51).

Both the chromium and nitrogen concentrations increase moving from pt. 01 across to pt. 04. The relative concentrations are more consistent with deposition from a Cr_2N target. If the capping-based nitrogen levels in Figure 4.57 are similar to Figure 4.56, then the nitrogen contributed from the PLD target is even less. That is not to say a CrN stoichiometry is impossible for the PLD target, as prior results demonstrated that chromium is more readily incorporated into the samples than nitrogen anyway.

According to unpublished supplementary data for [51], the expected chromium and nitrogen concentrations at pt. 01 are in the range 3.5-4.5 at%, pt. 02 is between 5.5-6.5 at%, pt. 03 is 7.8-9.2 at%, and pt. 04 is pt. 04 spans 10.0-11.2 at%. The doping concentrations of chromium in these GDOES measurements are higher than expected from the simulation. The maximum value of 17.3% at pt. 04 is, however, in the range of the chromium concentrations determined by SIMS on this sample [51]. The chromium levels observed here are perhaps more consistent with deposition from a Cr_2N PLD target. The nitrogen concentrations conform more closely to (but fall somewhat below) the simulated values.

Similar to the case for CCS-O-700 above, pt. 01 here displays an initial dip and rise, whereas the signal is stable in pts. 02-4. The onset of the silicon signal in pt. 01 is more gradual than in any of the other CDP plots. This has the appearance of poor lateral resolution due to a non-uniform crater shape, although it's unclear why this point should suffer more than the others. Also in keeping with CCS-O-700, the titanium concentration, after dropping from its pt. 01 level, does not change so much at pts. 02-04. The increasing doping levels has a greater impact on oxygen, correlating with a decrease in concentration. The ratio of titanium to oxygen concentration at pts. 03 and 04 is slightly closer to stoichiometric compared to those pts. in CCS-O-700 or CCS-Cap-NoCr.

The density in the film calculated according to the calibration curves rises from 4.4 g/cm^3 at pt. 01 to 4.7 g/cm^3 at pt. 04, in agreement with increasing chromium content. The film thickness is calculated to be 190-210 nm, which is somewhat thinner than the simulated values at these measurement positions [51].

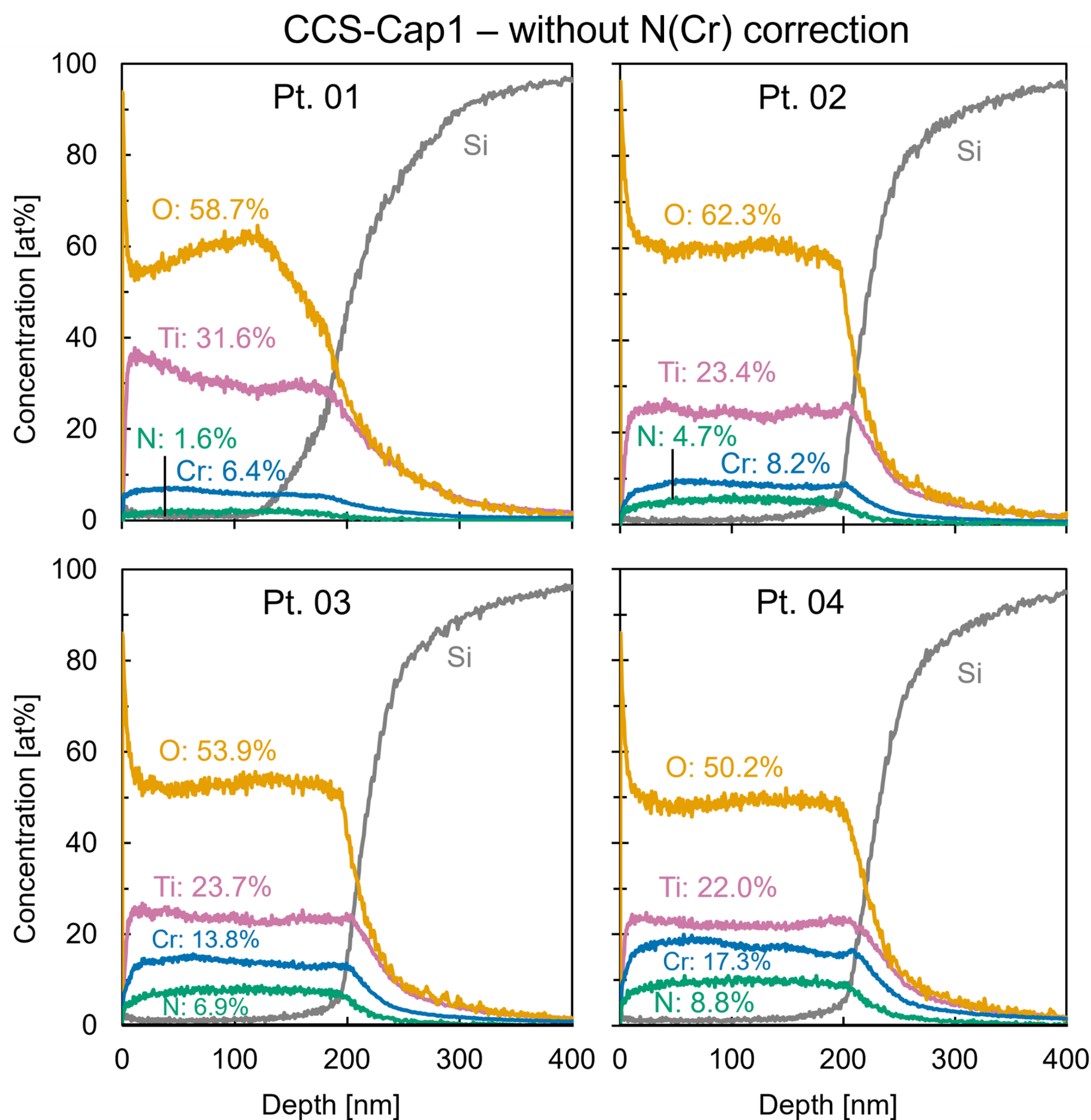

Figure 4.57: Composition depth profiles of four measurement positions on CCS-Cap1. The calibration curves used were Ti, O, Cr, N (without any intensity correction), and Si.

Figure 4.58 presents the compositional depth profiles of CCS-Cap1 pts. 01-04 when the chromium-based nitrogen correction factor is applied in the calibration. As expected, the nitrogen concentration at each point strongly increases, and the other elements decrease somewhat in concentration compared to Figure 4.57. The doping levels in this case are much larger (nearly double) the simulated values. This version of the quantification is consistent with deposition from a stoichiometric CrN PLD target, factoring in a small boost to nitrogen levels due to the capping procedure. The trends in oxygen and nitrogen across the four measurements are otherwise the same as commented above. The density and film thicknesses are also not substantially different.

In all three CCS samples, pt. 01 demonstrates some differences from pts. 02-04.

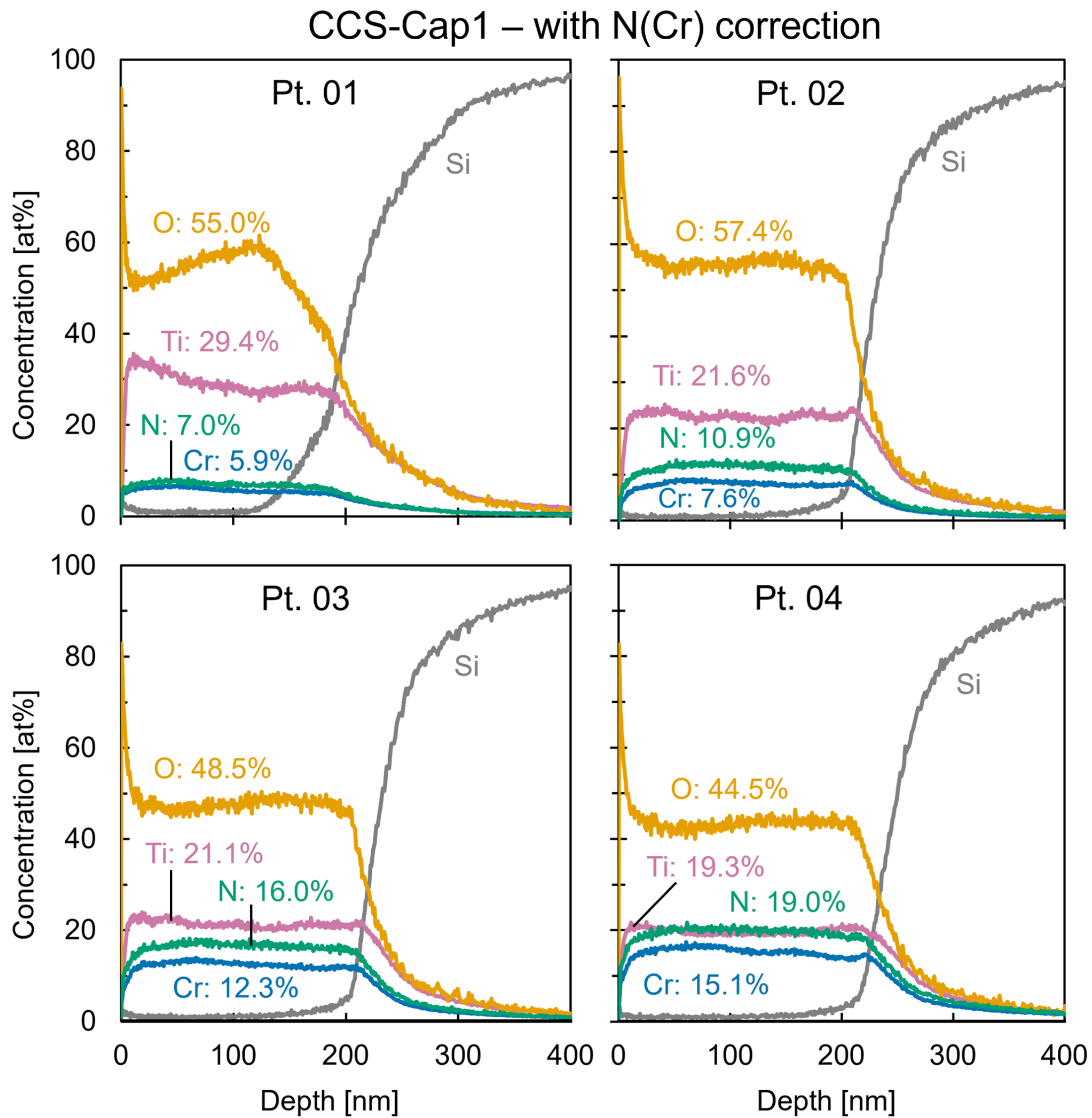

Figure 4.58: A comparable CDP of CCS-Cap1 to Figure 4.57, but using a nitrogen calibration that includes a correction to nitrogen concentration according to interference from the chromium signal.

Whereas the latter points display a relatively steady oxygen concentration in the film, the profile at pt. 01 seems to dip at the surface before rising slightly. According to the trend in pts. 02-4, as chromium and nitrogen doping concentrations increase, oxygen content decreases and titanium remains largely unchanged. Comparing pt. 01 and pt. 02, however, the oxygen concentration actually increases, and the titanium concentration noticeably falls. Despite less chromium at pt. 01, the density calculated for this region of the film is consistently higher than at pt. 02.

These differences may be related to the crystallinity of the film. In Ref. [51], TEM bright-field and selected-area electron diffraction measurements were taken along the center line of the wafer and found significantly higher crystalline quality near plume

center $\times_1$. This may be related to the higher kinetic energy of ablated atoms depositing at this position. Although pt. 01 here is vertically displaced from $\times_1$, it may still benefit to a degree from the proximity. Without having TEM measurements at the particular GDOES points presented here, it is difficult to do more than speculate.

A final note simply reiterates the major difference in results based on the application/omission of correcting nitrogen intensity based on a possible chromium interference. The quantified nitrogen concentrations change by more than a factor of 2. Given the relatively large errors found when validating the calibration curves, it may be more appropriate to treat these CDP results as another form of qualitative results, offering useful comparative information, but lacking the rigor to confidently state elemental concentrations.

4.7 Future work

This project has made some progress in attempting to use GDOES for quantitative elemental analysis of CCS PLD films. Of course, for every answer found, two more questions seem to arise.

Some avenues for future investigation include adjustments to the instrumental setup and measurement method. Diagnostic checks on a reference sample have revealed a steady decrease in detected optical intensity of the years. Cleaning the spectrometer window may be an overdue task. The issues with atmospheric leakage (and resulting uncertainty in the true nitrogen signal) is suspected to be related to sample sealing. It is possible that the O-ring may be somewhat dried out or worn. Replacing this component could improve the vacuum integrity.

A smaller measurement area would be preferable for these samples, both to minimize the destructive consequences and to obtain results over a tighter range of concentration gradient. Smaller anodes (2 mm diameter, for example) are available, but sharing a lab with other users makes it inconvenient to repeatedly switch from the common 4 mm anode. It is conceivable that some sort of removable mask might be developed to employ the 4 mm anode but restrict the sputtering area to a smaller spot on the sample.

Another experimental modification project would be the creation of an apparatus designed to seal the entire sample in a redundant vacuum or argon environment during measurement, eliminating contributions from atmospheric gases. Such a device is already manufactured by Horiba, but is too small for the 2” wafers.

The monochromator could be used to record different emission lines for oxygen or nitrogen, lines which are not subject to interferences from hydrogen or chromium. More sophisticated curve-fitting can also be included, provided the modifications have a theoretical grounding. Any changes to the instrument or measurement method will

require a re-calibration to be performed [45].

Perhaps the most effective way to improve the quality of the calibration curves is simply the inclusion of more CRMs. The nitrogen and chromium curves, in particular, are primarily built from samples with a $c_i\ q_M$ quite far from the range of interest. This may or may not be a reasonable investment, depending on how seriously the group intends to continue pursuing GDOES quantification of such PLD films.

Before resorting to the acquisition of additional CRMs, the validity of the variable power calibration method performed in Ref. [42] could be investigated, as it would potentially allow a three-fold (or greater) increase in the number of calibration data points, while using the same reference samples currently available.

Similarly, some of the non-CRM calibration samples used in this work had rather large uncertainties associated with them. Pairing with other elemental characterization techniques such as EDX could aid to decrease the elemental uncertainty from reference samples such as F-TiO_2-O-700-opt, which was not a CRM but included anyways in the calibration because of its extremely relevant nominal composition. Of course, this complicates the process by introducing potential shortcomings of EDX and somewhat negates the desired convenience of using GDOES in the first place.

The GDOES results cast suspicion on the stated composition of the CrN PLD target. Checking the target density could provide additional information. This could be done, for example, by weighing the target on a sensitive balance, and then determining the sample volume by the Archimedes principle (immersion in water). The sub-nominal density range provided with the PLD target somewhat complicates the interpretation, but Cr_2N is expected to have a larger density than that of CrN. Raman spectroscopy or X-ray diffraction would also be useful tools to determine the chemical phases present in the target.

Chapter 5

Conclusions

This Master thesis project has explored the use of glow discharge optical emission spectroscopy for qualitative and quantitative elemental analysis of PLD-fabricated thin films composed of TiO_2 doped with Cr and N, as well as additional related samples. The continuous compositional spread (Cr+N) co-doped TiO_2 samples were the result of previous work by the Reenaas research group, developed as a stepping stone in pursuit of an intermediate band material. Such a material is the key component in creating an intermediate band solar cell, a 3rd-generation photovoltaic technology with a large potential efficiency.

GDOES was selected as a tool to characterize the elemental composition of these samples, in particular the Cr and N doping levels. The technique employs a plasma to sputter the sample surface and simultaneously excite sputtered atoms, resulting in characteristic optical emissions that can be linked to the presence of particular elements in the sample. Quantitative analysis is possible, but requires a calibration procedure and comparison to measurements on samples of a known composition.

A variety of these calibration samples were obtained and used to generate calibration curves for the elements: Ti, O, Cr, N, and Si. The calibration process involved taking a GDOES measurement on the sample to record signal intensities and determining the sample sputtering rate by measuring the resultant crater depth by profilometry. Some experiments were performed aiming to use a single sample for multiple data points, but the method needs further study. After all this data was collected, a regression line was calculated for each of the elements of interest. Correction factors and higher-order terms were used to improve the fit of some curves.

In response to fluctuating nitrogen signals, a non-destructive method was developed to indicate a sufficient sample seal to minimize contamination from atmospheric gas. Before analyzing the combinatorial PLD samples, qualitative GDOES measurements were made on a variety of PLD plume films - experimental depositions using only TiO_2 or CrN. The findings are in agreement with prior characterization work. TiO_2 deposition in a N_2 background gas can result in nitrogen incorporation into the

film, cycling between N_2 and O_2 during deposition of CrN results in undesired oxide phases, and a lower substrate temperature (550°C) is more conducive to nitrogen incorporation.

Four positions were measured on each CCS film to compare the elemental signals along the concentration gradient. The qualitative results confirm the expected trends: increasing chromium and nitrogen content moving from the left side of the sample to the right, and a similar dependence on deposition parameters as was seen for the plume films.

Two slightly different versions of the calibration curves were applied for compositional depth profiling of the CCS films. The outcome largely follows from the qualitative results. The inclusion or omission of a chromium-interference correction factor to the nitrogen signal, however, has a significant impact. In the sample CCS-Cap1, the average chromium and nitrogen concentrations at the rightmost measurement position are 15.1 and 19.0%, respectively, when applying the correction. Without the correction, the values are 17.3 and 8.8%. Neither set of values quite matches the results from a PLD simulation.

The qualitative results are useful as a confirmation and complement to other characterization performed on these samples. The quantitative results have a large potential error and improvements to the calibration curve are needed. A variety of directions for future work can be pursued; some tasks relate to modifying the experimental method for better, more consistent measurements, and other efforts could improve the calibration curves by including more data points (from additional CRMs or more measurements of existing references) and by tightening the uncertainties in the calibration standards used.

References

[1] Jacob Ng. "GDOES for Qualitative Analysis of PLD Thin Films". NTNU specialization project - unpublished. Dec. 2022.

[2] Jeff Tollefson. *The hard truths of climate change — by the numbers*. Sept. 2019. URL: https://www.nature.com/immersive/d41586-019-02711-4/index.html.

[3] Tim Montague. *A trillion $$ wealth creation opportunity: Jigar Shah interview roundup part I of II*. Jan. 2021. URL: https://cesnrg.com/blog/jigarshah_wealth_creation_p1/.

[4] *COP21: Climate change in figures*. URL: https://www.oecd.org/environment/cop21-climate-change-in-figures.htm.

[5] Godfrey Boyle. *Renewable energy: power for a sustainable future*. Oxford University Press in association with the Open University, 2012.

[6] Varun Sivaram. *Taming the Sun*. MIT Press, 2019.

[7] *The Solar Spark - The Science - Renewable Energy*. URL: http://www.solarspark.chem.ed.ac.uk/science/renewable-energy.

[8] Saul Griffith. *Electrify: An optimists playbook for our clean energy future*. MIT PRESS, 2022.

[9] Nancy M Haegel et al. "Terawatt-scale photovoltaics: Trajectories and challenges". In: *Science* 356.6334 (2017), pp. 141–143.

[10] Madhumitha Jaganmohan. *Global cumulative installed solar PV capacity 2021*. Nov. 2022. URL: https://www.statista.com/statistics/280220/global-cumulative-installed-solar-pv-capacity/.

[11] Brittany L Smith et al. *Photovoltaic (PV) Module Technologies: 2020 Benchmark Costs and Technology Evolution Framework Results*. Tech. rep. National Renewable Energy Lab (NREL), Golden, CO (United States), 2021.

[12] Kunta Yoshikawa et al. "Silicon heterojunction solar cell with interdigitated back contacts for a photoconversion efficiency over 26%". In: *Nature Energy* 2.5 (2017), p. 17032. ISSN: 2058-7546. DOI: 10.1038/nenergy.2017.32. URL: https://doi.org/10.1038/nenergy.2017.32.

[13] Martin A. Green. *Third generation photovoltaics : advanced solar energy conversion*. Springer, 2006, p. 160. ISBN: 9783540265627.

[14] Stuart Bowden and Christiana Honsberg. *Refining silicon.* URL: https://www.pveducation.org/pvcdrom/manufacturing-si-cells/refining-silicon.

[15] William Shockley and Hans J Queisser. "Detailed balance limit of efficiency of p-n junction solar cells". In: *Journal of applied physics* 32.3 (1961), pp. 510–519.

[16] Marcus Wilke et al. "Glow discharge optical emission spectroscopy for accurate and well resolved analysis of coatings and thin films". In: *Thin Solid Films*. Vol. 520. 5. Dec. 2011, pp. 1660–1667. DOI: 10.1016/j.tsf.2011.07.058.

[17] Sven Rühle. "Tabulated values of the Shockley–Queisser limit for single junction solar cells". In: *Solar Energy* 130 (2016), pp. 139–147. ISSN: 0038-092X. DOI: https://doi.org/10.1016/j.solener.2016.02.015. URL: https://www.sciencedirect.com/science/article/pii/S0038092X16001110.

[18] Y. Okada et al. "Intermediate band solar cells: Recent progress and future directions". In: *Applied Physics Reviews* 2.2 (June 2015). ISSN: 19319401. DOI: 10.1063/1.4916561.

[19] Stephen P. Bremner, Michael Y. Levy, and Christiana B. Honsberg. "Limiting efficiency of an intermediate band solar cell under a terrestrial spectrum". In: *Applied Physics Letters* 92.17 (2008). ISSN: 00036951. DOI: 10.1063/1.2907493.

[20] Tianhao Wu et al. "The Main Progress of Perovskite Solar Cells in 2020–2021". In: *Nano-Micro Letters* 13.1 (Dec. 2021). ISSN: 21505551. DOI: 10.1007/s40820-021-00672-w.

[21] Akira Fujishima, Xintong Zhang, and Donald A Tryk. "TiO2 photocatalysis and related surface phenomena". In: *Surface Science Reports* 63.12 (2008), pp. 515–582. ISSN: 0167-5729. DOI: https://doi.org/10.1016/j.surfrep.2008.10.001. URL: https://www.sciencedirect.com/science/article/pii/S0167572908000757.

[22] Wenguang Zhu et al. "Band gap narrowing of titanium oxide semiconductors by noncompensated anion-cation codoping for enhanced visible-light photoactivity". In: *Physical Review Letters* 103.22 (Nov. 2009). ISSN: 00319007. DOI: 10.1103/PhysRevLett.103.226401.

[23] Thomas Nelis and Richard Payling. *Glow discharge optical emission spectroscopy: A practical guide*. eng. RSC analytical spectroscopy monographs. Cambridge, U.K.: Royal Society of Chemistry, 2003. ISBN: 1-84755-098-3.

[24] HORIBA Jobin Yvon. *GD-PROFILER 2 User Manual*. Tech. rep. Oct. 2016. DOI: Reference:1131088561. URL: http://www.horiba.com/scientific.

[25] Volker Hoffmann et al. "Present possibilities of thin-layer analysis by GDOES". In: *Surface and Interface Analysis* 35.7 (July 2003), pp. 575–582. ISSN: 01422421. DOI: 10.1002/sia.1575.

[26] Ramón Escobar Galindo et al. "Towards nanometric resolution in multilayer depth profiling: A comparative study of RBS, SIMS, XPS and GDOES". In: *Analytical and Bioanalytical Chemistry* 396.8 (2010), pp. 2725–2740. ISSN: 16182650. DOI: 10.1007/s00216-009-3339-y.

[27] K. Shimizu et al. "Radiofrequency GDOES: A powerful technique for depth profiling analysis of thin films". In: *Surface and Interface Analysis* 35.7 (July 2003), pp. 564–574. ISSN: 01422421. DOI: 10.1002/sia.1572.

[28] Yedidyah Langsam. *Brooklyn College - C.I.S. 1110 - Assignment #3*. 2009. URL: http://eilat.sci.brooklyn.cuny.edu/cis1_5/old%20hws/hw2d_c.htm.

[29] S. J. Lötter, W. Purcell, and J. T. Nel. "Glow discharge optical emission spectroscopy: A general overview with regard to nuclear materials". In: *Journal of the Southern African Institute of Mining and Metallurgy* 115.10 (Oct. 2015), pp. 967–972. ISSN: 22256253. DOI: 10.17159/2411-9717/2015/v115n10a11.

[30] Vasile-Dan Hodoroaba et al. "Depth profiling of electrically non-conductive layered samples by RF-GDOES and HFM plasma SNMS". In: *Applied surface science* 179.1-4 (2001), pp. 30–37.

[31] Thomas Nelis and Jozsef Pallosi. "Glow discharge as a tool for surface and interface analysis". In: *Applied Spectroscopy Reviews* 41.3 (2006), pp. 227–258. ISSN: 05704928. DOI: 10.1080/05704920600620345.

[32] K. Shimizu et al. "Influence of interracial depth on depth resolution during GDOES depth profiling analysis of thin alumina films". In: *Surface and Interface Analysis* 31.9 (Sept. 2001), pp. 869–873. ISSN: 01422421. DOI: 10.1002/sia.1120.

[33] Arne Bengtson and Thomas Nelis. "The concept of constant emission yield in GDOES". In: *Analytical and Bioanalytical Chemistry* 385.3 (June 2006), pp. 568–585. ISSN: 16182642. DOI: 10.1007/s00216-006-0412-7.

[34] Michael R. Winchester and Richard Payling. "Radio-frequency glow discharge spectrometry: A critical review". In: *Spectrochimica Acta - Part B Atomic Spectroscopy* 59.5 (May 2004), pp. 607–666. ISSN: 05848547. DOI: 10.1016/j.sab.2004.02.013.

[35] D. Ifezue. "Optical interference during rf-gdoes depth profiling of anodized aluminum-tantalum alloy films". In: *Journal of Materials Engineering and Performance* 22.8 (Aug. 2013), pp. 2366–2376. ISSN: 10599495. DOI: 10.1007/s11665-013-0516-0.

[36] Alexander Kramida. *Atomic Spectra Database Lines form*. Nov. 2019. URL: https://physics.nist.gov/PhysRefData/ASD/lines_form.html.

[37] E Marin et al. "Chemical and electrochemical characterization of TiO2/Al2O3 atomic layer depositions on AZ-31 magnesium alloy". In: *Journal of Coatings Technology and Research* 9.3 (2012), pp. 347–355.

[38] Zdenek Weiss and Petr Vlcak. "Analysis of shallow depth profiles of titanium nitride and N-implanted titanium by GD-OES: the 'hydrogen effect'after the discharge startup and a correction thereof". In: *Journal of Analytical Atomic Spectrometry* 32.12 (2017), pp. 2476–2484.

[39] Beatriz Fernández et al. "Investigations of the effect of hydrogen, nitrogen or oxygen on the in-depth profile analysis by radiofrequency argon glow discharge-optical emission spectrometry". In: *Journal of Analytical Atomic Spectrometry* 18.2 (2003), pp. 151–156.

[40] Petr Smid et al. “The effect of hydrogen and nitrogen on emission spectra of iron and titanium atomic lines in analytical glow discharges”. In: *Journal of Analytical Atomic Spectrometry* 23.9 (2008), pp. 1223–1233.

[41] Vasile Dan Hodoroaba et al. “Investigations of the effect of hydrogen in an argon glow discharge”. In: *Journal of analytical atomic spectrometry* 15.9 (Sept. 2000), pp. 1075–1080. ISSN: 02679477. DOI: 10.1039/b002367l.

[42] Richard Payling et al. “New aspects of quantification in rf GDOES”. In: *Surface and Interface Analysis: An International Journal devoted to the development and application of techniques for the analysis of surfaces, interfaces and thin films* 35.7 (2003), pp. 583–589.

[43] Richard Payling, Johann Michler, and Max Aeberhard. “Quantitative analysis of conductive coatings by radiofrequency-powered glow discharge optical emission spectrometry: hydrogen, dc bias voltage and density corrections”. In: *Surface and Interface Analysis: An International Journal devoted to the development and application of techniques for the analysis of surfaces, interfaces and thin films* 33.6 (2002), pp. 472–477.

[44] Richard Payling et al. “Theory of relative sputtering rates in GDOES”. In: *Surface and Interface Analysis* 35.4 (Apr. 2003), pp. 334–339. ISSN: 01422421. DOI: 10.1002/sia.1536.

[45] HORIBA Jobin Yvon. *Quantum V2.08 User Guide*. Tech. rep. Sept. 2010. DOI: Reference:31088534. URL: http://www.horiba.com/scientific.

[46] David P. Norton. “Pulsed Laser Deposition of Complex Materials: Progress Toward Applications”. In: *Pulsed laser deposition of thin films: applications-led growth of functional materials*. Ed. by Robert Eason. John Wiley & Sons, 2007. Chap. 1, pp. 1–30. DOI: doi.org/10.1002/9780470052129.ch1.

[47] Marcus Grand Michaelsen. “Pulsed laser deposited TiO2: X-ray diffraction and Raman spectroscopy studies”. MA thesis. Norwegian University of Science and Technology, July 2022.

[48] Hogne Lysne et al. “Improved methods for design of PLD and combinatorial PLD films”. In: *Journal of Applied Physics* 132.12 (Sept. 2022). ISSN: 10897550. DOI: 10.1063/5.0105298.

[49] T. Brakstad et al. “nc-PLD of (Cr+N) co-doped TiO2 for intermediate band solar cells. PART 1: Challenges in N incorporation”. Draft of forthcoming publication. 2023.

[50] Herman Solstrand. “Characterization of TiO2 based thin films using Raman spectroscopy”. MA thesis. Norwegian University of Science and Technology, Dec. 2021.

[51] T. Brakstad et al. “nc-PLD of (Cr+N) co-doped TiO2 for intermediate band solar cells. PART 2: Optical properties and microstructre”. Draft of forthcoming publication. 2023.

[52] *Silicon Wafers & other semiconductor substrates in stock*. Oct. 2018. URL: https://order.universitywafer.com/default.aspx?cat=Silicon&diam=50.8mm.

[53] R Escobar Galindo et al. "Calibration of nitrogen content for GDOES depth profiling of complex nitride coatings". In: *Journal of Analytical Atomic Spectrometry* 22.12 (2007), pp. 1512–1516.

[54] *Chromium products.* CrN PLD target no longer listed online. 2023. URL: https://www.samaterials.com/165-chromium.html.

[55] Deborah Alberts et al. "Analytical performance of pulsed radiofrequency glow discharge optical emission spectrometry for bulk and in-depth profile analysis of conductors and insulators". In: *Journal of Analytical Atomic Spectrometry* 26.4 (2011), pp. 776–783.

[56] *Certified Reference Materials - 4xxx AlSi - 1045.* 2020. URL: https://reference-materials.ch/en/A~1045.

[57] *Low-Alloy Steel 1766.* 2021. URL: https://shop.nist.gov/ccrz__ProductDetails?sku=1766&cclcl=en_US.

[58] *HASTELLOY C-276 TECHNICAL DATA.* The supplier for the particular C276 sample used is not known. 2015. URL: https://www.hightempmetals.com/techdata/hitempHastC276data.php.

[59] *Jernkontoret - Certified Reference Materials 2018-2019.* The CE650 sample listed in the most recent catalogue differs slightly from the one found in the NTNU GDOES lab. 2018. URL: https://www.swerim.se/file/thecrmcatalogue2018pdf-0.

[60] *Instrument introduction.* URL: https://www.horiba.com/sgp/scientific/technologies/glow-discharge-optical-emission-spectroscopy/instrument-introduction/.

[61] Shiva Mohajernia et al. "Depth elemental characterization of 1D self-aligned TiO 2 nanotubes using calibrated radio frequency glow discharge optical emission spectroscopy (GDOES)". In: *Applied Surface Science* 442 (June 2018), pp. 412–416. ISSN: 01694332. DOI: 10.1016/j.apsusc.2018.02.185.

[62] I. S. Molchan et al. "The concept of plasma cleaning in glow discharge spectrometry". In: *Journal of Analytical Atomic Spectrometry* 24.6 (2009), pp. 734–741. ISSN: 13645544. DOI: 10.1039/b818343k.

[63] Mahr GmbH. *MarSurf M 400.* Nov. 2015. URL: https://metrology.mahr.com/fileadmin/assets/files/MarSurf--M%5C%20400--3760426--FL--EN--2015-11-19.pdf.

[64] Peter de Groot. "Principles of interference microscopy for the measurement of surface topography". In: *Advances in Optics and Photonics* 7.1 (Mar. 2015), p. 1. ISSN: 19438206. DOI: 10.1364/aop.7.000001.

[65] Petr Klapetek, David Necas, and Christopher Anderson. *Gwyddion user guide.* URL: http://gwyddion.net/documentation/user-guide-en/.

[66] L Therese et al. "Improved voltage transfer coefficients for nonconductive materials in radiofrequency glow discharge optical emission spectrometry". In: *Analytical and bioanalytical chemistry* 386 (2006), pp. 163–168.

[67] L Wilken, V Hoffmann, and K Wetzig. "Radio frequency glow discharge source with integrated voltage and current probes used for sputtering rate and emission yield measurements at insulating samples". In: *Analytical and bioanalytical chemistry* 383 (2005), pp. 424–433.

[68] Philippe Le Coustumer et al. "Surface characterization and depth profile analysis of glasses by rf GDOES". In: *Surface and Interface Analysis: An International Journal devoted to the development and application of techniques for the analysis of surfaces, interfaces and thin films* 35.7 (2003), pp. 623–629.

[69] Beatriz Fernández et al. "In-depth profile analysis of thin films deposited on non-conducting glasses by radiofrequency glow-discharge–optical emission spectrometry". In: *Analytical and bioanalytical chemistry* 384 (2006), pp. 876–886.

[70] Patrick Chapon. *Horiba GDOES advice for NTNU project.* Dec. 2022.

Appendix A - Spectrometer detection wavelengths

Table A.1: The wavelengths chosen for analysis of elements in the polychromator. 'I' after the element name indicates the spectral line comes from the ground state (not ionized) atom, whereas 'II' denotes an emission line from a singly-ionized atom.

Element	Wavelength [nm]	Element	Wavelength [nm]
Ag I	328.073	Li I	670.800
Al I	396.157	Mg I	285.217
Au I	242.799	Mn I	403.455
Ba II	455.410	Mo I	386.416
Bi I	306.776	N I	149.267
C I	156.149	Na I	589.600
Ca II	393.372	Ni I	341.481
Cd I	228.806	O I	130.223
Cl I	134.730	P I	178.291
Co I	345.356	Pb I	405.788
Cr I	425.439	Pt I	265.949
Cu I	324.759	S I	180.738
F I	685.611	Si I	288.162
Fe I	371.999	Sn I	317.510
Ga I	417.211	Sr I	421.558
Ge I	275.949	Ti I	365.355
H I	121.574	V I	411.185
Hf I	286.641	Zn I	481.060
In I	451.138	Zr II	339.203
K I	766.500		

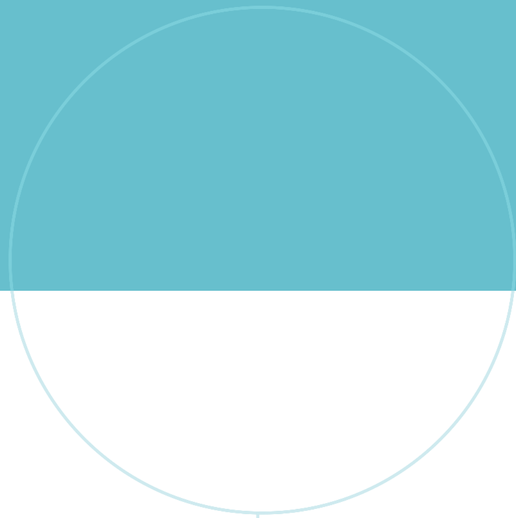

NTNU
Norwegian University of
Science and Technology

DTU
Technical University
of Denmark